2017

Mesoscopic Interactions in Complex Photonic Media

Roxana Rezvani Naraghi
University of Central Florida

MESOSCOPIC INTERACTIONS IN COMPLEX PHOTONIC MEDIA

by

ROXANA REZVANI NARAGHI
B.S. University of Tehran, 2009
M.S. University of Tehran, 2012
M.S. University of Central Florida, 2015

A dissertation submitted in partial fulfillment of the requirements
for the degree of Doctor of Philosophy
in the Department of Physics
in the College of Sciences
at the University of Central Florida
Orlando, Florida

Spring Term
2017

Major Professor: Aristide Dogariu

ABSTRACT

Mesoscale optics provides a framework for understanding a wide range of phenomena occurring in a variety of fields ranging from biological tissues to composite materials and from colloidal physics to fabricated nanostructures. When light interacts with a complex system, the outcome depends significantly on the length and time scales of interaction. Mesoscale optics offers the apparatus necessary for describing specific manifestations of wave phenomena such as interference and phase memory in complex media. In-depth understanding of mesoscale phenomena provides the required quantitative explanations that neither microscopic nor macroscopic models of light-matter interaction can afford. Modeling mesoscopic systems is challenging because the outcome properties can be efficiently modified by controlling the extent and the duration of interactions.

In this dissertation, we will first present a brief survey of fundamental concepts, approaches, and techniques specific to fundamental light-matter interaction at mesoscopic scales. Then, we will discuss different regimes of light propagation through randomly inhomogenous media. In particular, a novel description will be introduced to analyze specific aspects of light propagation in dense composites. Moreover, we will present evidence that the wave nature of light can be critical for understanding its propagation in unbounded highly scattering materials. We will show that the perceived diffusion of light is subjected to competing mechanisms of interaction that lead to qualitatively different phases for the light evolution through complex media. In particular, we will discuss implications on the ever elusive localization of light in three-dimensional random media.

In addition to fundamental aspects of light-matter interaction at mesoscopic scales, this dissertation will also address the process of designing material structures that provide unique scattering properties. We will demonstrate that multi-material dielectric particles with controlled radial and azimuthal structure can be engineered to modify the extinction cross-section, to control the scattering directivity, and to provide polarization-dependent scattering. We will show that dielectric core-shell structures with similar macroscopic sizes can have both high scattering cross-sections and radically different scattering phase functions. In addition, specific structural design, which breaks the azimuthal symmetry of the spherical particle, can be implemented to control the polarization properties of scattered radiation. Moreover, we will also demonstrate that the power flow around mesoscopic scattering particles can be controlled by modifying their internal heterogeneous structures.

Lastly, we will show how the statistical properties of the radiation emerging from mesoscopic systems can be utilized for surface and subsurface diagnostics. In this dissertation, we will demonstrate that the intensity distributions measured in the near-field of composite materials are direct signatures of the scale-dependent morphology, which is determined by variations of the local dielectric function. We will also prove that measuring the extent of spatial coherence in the proximity of two-dimensional interfaces constitutes a rather general method for characterizing the defect density in crystalline materials. Finally, we will show that adjusting the spatial coherence properties of radiation can provide a simple solution for a significant deficiency of near-field microscopy. We will demonstrate experimentally that spurious interference effects can be efficiently eliminated in passive near-field imaging by implementing a random illumination.

To my mother Hamideh Tabatabaie

ACKNOWLEDGMENT

The completion of this work is the result of scientific collaborations, fruitful discussions, research partnerships and friendships of many different people. I would like to briefly acknowledge all of them. First and foremost, I would like to thank Dr. Aristide Dogariu, my PhD advisor. I cannot even put into words the appreciation and gratitude I have for all that Dr. Dogariu has taught me ever since I have known him. He is a patient teacher, brilliant scientist, compassionate leader, and supportive friend. He appreciates the value of educating young scientists and has worked tirelessly over his entire academic career to ensure that his students graduate with the best scientific comprehension that one can achieve. His timely trust in me helped me to develop self-confidence. Every day I learned something new, not only in terms of research but also in different aspects of life. He has taught me the value of scientific reasoning, critical thinking, and striving for perfection in everything I do. In general, he made me a better person. He even spent his valuable time to teach me rock climbing. Whatever challenge I encountered, whether in research or life, he has always been available to discuss it. I honestly cannot imagine a better mentor; it really has been a privilege working with him.

I would like to thank Dr. Ayman F. Abouraddy not only for being a member of my committee, but also for all our collaborations throughout my studies at CREOL with Multi-material Optical Fiber Devices Group. Special thanks to Felix, Guang-Ming, Soroush and Joshua.

I also want to acknowledge my committee members, Dr. Talat S. Rahman and Dr. Laurene Tetard for their enlightening discussions and guidance. I would like to thank the CREOL and Physics faculty and administrative staff.

I would like to thank our collaborators, Dr. J. J Saenz, Dr. L. G. Cançado, Dr. F. Salazar-Bloise for thoughtful discussions. I would like to especially thank Gustavo for sharing his expertise in Graphene and near-field microscopy with me. I also would like to thank Dr. Paul Wiegand for assistance with the Stokes operation.

I would like to express all my gratitude and appreciation to Dr. Madi Dogariu, for being very supportive. She is one of the kindest, most compassionate, understanding and coolest person I ever meet.

I gratefully thank all the former and current members of the Photonic Diagnostics of Random Media group. I am specifically grateful to Dr. Dana C. Kohlgraf-Owens for putting in her time to train me how to work with Near-field Scanning Optical Microscope. I would also like to especially acknowledge Dr. Sergey Sukhov, for teaching me so many things in optics and mathematical modeling, showing patience with me, and being a great friend and officemate.

On a more personal note, I would like to thank my friends. I have so many friends to thank that I cannot possibly mention all of them here. I would like to thank all my friends at University of Tehran. I wish to thank Azarin my dearest friend and sister, Midya for always taking care of me, Bardia for bringing fun to my PhD life, Fedor for introducing me to the Russian culture and food, Amir, Alireza, Negin, Amin, Fatemeh, Hossein, Marzieh, Masoud, Soroush, Nazanin, Sia, Mehdi, Faraz, Marta, Mahtab, Marjan, Dan,

Tomas, Nima, Minoo, Behnaz, Sepehr, Moji, Mahmood, Mahdi, Parinaz, Zahra, Seyfollah and all the others…

But the main aspect of life during all these years has been my outstanding family. My family has been the most important driving force during my studies, and I am always appreciative to them throughout my entire life. My deepest appreciation goes to my mom, my best friend Hamideh, for always supporting me, being so understanding, and teaching me the meaning of life. She is my role model for many different reasons. My dad Behrooz, and my brothers Rouzbeh and Ashkan, thank you so much for always being there for me, helping me through all the tough times, following my progress, and instilling confidence in me. I also thank my sisters in law Leila and Setareh and my beautiful niece, Lilia for bringing happiness and joy to my life. I would also like to thank my late grandmother Habibeh, late Uncle Abolghasem, Auntie Zohreh, Shahnaz, Haideh and Uncle Mohammad. I thank my cousins Reyhaneh, Nazli, Ehsan, Shadi, Nima, Neda. Special thanks to Auntie Maryam and my cousin Vafa for all of their support. I love you all so much, and you have no idea how much you mean to me.

TABLE OF CONTENTS

LIST OF FIGURES

CHAPTER 1:
INTRODUCTION TO MESOSCOPIC OPTICS

1.1 Why do we need to study mesoscale optics?

The way in which light and matter influence each other depends not only on the optical properties of incident field (wavelength, wave-front, coherence, strength, etc.) and the material or structural properties of the medium (size, refractive index, composition, periodicity, etc.), but also on the effective scale of light-matter interaction. If the structure is much larger than the wavelength of the incident light, one can use traditional continuum optics. On the other hand, if the structure is much smaller than the wavelength, a simple dipole approximation may suffice for explaining how light is scattered. However, there are also intermediate, mesoscopic scales where significant restructuring of the field occurs over distances in the order of the wavelength. Mesoscopic interaction refers to optical phenomena developed over scales characteristic to wavelength of radiation, in contrast to macroscopic descriptions of much larger scales or microscopic accounts which describe the interaction at scales significantly smaller than the wavelength. For instance, at intermediate scales between atomic and macroscopic, neither the laws of quantum mechanics nor the classical mechanics can capture the unique characteristics of physical phenomena. For electronic systems, understanding the phenomenology and controlling the transport properties at these scales resulted in extraordinary capabilities for miniaturization [1–3].

In optics, the interest in mesoscopic phenomena is stimulated by the advent of new composite photonic materials in support of the ever-increasing need for enhancing the

functionality and the performance of optical devices [4,5]. Engineering new structures with properties beyond those of natural materials can only be accomplished by carefully accounting for electromagnetic interactions that extend over many wavelengths while providing means to efficiently project macroscopic outcomes. On the other hand, limiting the scale of interaction can also lead to novel phenomena in extreme environments where electromagnetic fields couple strongly to matter [1,2]. At photonic mesoscales, fascinating interaction and confinement phenomena occur across different scales in both time and space. At such dimensions, photonic phenomena include scale-specific modifications of the structure in response to light so that a passive linear interpretation of the reciprocal action is inadequate, and nonlinear descriptions including the dynamics of the light-structure interaction are necessary. Remarkably, the effective light-matter interaction can be conveniently tuned to emulate phenomenology impossible to probe at atomic scales [6,7].

In general, mesoscopic phenomena are primarily due to wave's phase coherence and they exhibit specific fluctuations which cannot be predicted neither by averages at macroscale nor by deterministic microscale models. More specifically, there is a characteristic length scale known as phase coherence length, for scales larger than that there is no phase coherence [1,2,8].

When light encounters complex material systems, an informative description requires an entire ensemble of realizations rather than one particular interaction between light and matter. These realizations can be created by changes in either the material system, the properties of the optical incident field, or both. Therefore, the ensemble of samples is

characterized by a set of identical macroscopic parameters such as the size and shape of the system, concentration of the scattering potential, wavelength and angular distribution of incident field, etc. Of course, to evaluate the outcome of the light matter interaction one needs to average over these ensembles [9]. These samples differ from each other due to specific realizations of random scattering potential and, as a result, the outcome of interaction with each sample brings its own specific fluctuation that depends both on the property of the sample and incident light. In this sense, information about all individual members of the ensemble is richer than an average; averaging inherently discards the information specific to a particular realization. In many situations however, one is required to average over many realizations, and the question is: can effects due to the phase coherence survive such averaging? The answer is found to be affirmative, a well-known example being coherent backscattering effect [1,10,11]. where the light backscattered from semi-infinite random media, an inherently averaged property of the light matter interaction, exhibits an angular dependence which cannot be explained by classical transport theory. This effect is commonly regarded as a manifestation of the weak localization of light in disordered media.

So far we discussed that the light matter interaction at mesoscales is highly complex, and each realization carry a fingerprint of the interaction. Although the average over this ensemble might revel certain coherence effects, one would have to go beyond this first moment of the distribution to acquire more information on the way light interacts with medium. Therefore, understanding and characterizing mesoscopic interactions requires approaches specific to statistical optics on which the outcomes depend. In general, the

properties of mesoscopic interactions depend on the duration, scale, and strength of interaction, and, most importantly, can deviate from the universal Gaussian statistics [1,12].

In static disordered media, mesoscopic interactions could be described in accordance with the scale of interaction. In general, there are six different length scales that characterize such a system: (i) the average size of the scatterers a, (ii) the wavelength of the incident light λ, (iii) the scattering mean free path l_s, which is the average distance between two scattering events, (iv) the transport mean free path l^*, which is the length scale over which the directional energy flux is randomized through successive scattering events (v) the phase coherence length l_φ, and (vi) the overall size of the system L. The relation between these length scales determine the different regimes of light-matter interaction. For instance, if $\lambda \gg a$, the scatterers are beyond the resolution of the incident field and, on the scale of one to two scattering mean free path, a disordered system looks like an effectively homogeneous medium. In the opposite case, when $L > l_\varphi$ the phase coherence is lost and the system becomes independent of the specific realization of disorder. In these circumstances, propagation of light is well described by a classical diffusion where the wave properties are inherently disregarded [2,8,10].

The duration of interaction is also an important factor to be considered mainly when the electromagnetic waves encounter dynamic systems such as colloidal suspensions or biological matter. More precisely, in these conditions the statistical properties of scattered light may vary depending on characteristics such as temporal coherence or the time of

measurement in addition to the intrinsic time scales associated with changes in the material system [1,13].

Another intriguing manifestation of extreme photonics at mesoscales is the emergence of active matter, a condition where the distinction between matter and radiation blurs. As opposed to passive matter like common solids or liquids, unique abilities to generate motion and stresses arise from the additional energy imparted to system's constituents: an active medium is out of thermodynamic equilibrium and displays unusual collective behaviors. Elucidating the effects of disorder in the presence of many-body interactions mediated by electromagnetic fields will certainly provide new avenues for creating synthetic materials that, for example, could mimic properties of living matter for an optimum energy management [14,15]. The study of the dynamic system and active matter are themselves vast subjects that we will not be discussed in this dissertation.

1.2 Outline – scope of thesis

Transport of light in complex media is at the core of many natural phenomena and technological applications. Simplistic descriptions however disregard the fact that light is an electromagnetic wave. In Chapter 2 of this dissertation we will demonstrate that the wave nature of light is critical for understanding its propagation in highly scattering materials where optical fields evolve through both homogeneous and evanescent waves. We will provide evidence of new regimes of light transport, which we modeled in terms of the critical near-field coupling between structural elements of complex media, this work has been published in [J3,C1,C3,C7,P2,P5].

In addition to the steady state conditions, we will study, later on in Chapter 2, the evolution of light in complex media. It was a long time belief that, with increasing the scattering strength, the transport of light gradually slows down and could, eventually, come to a hold corresponding to a localized state. We will demonstrate, both experimentally and theoretically, that the perceived diffusion of light is subjected to competing mechanisms of interaction that lead to qualitatively different phases of evolution. These results could impact the ever elusive localization of light in three-dimensional random media and can also provide means to engineer materials where anomalous transport can be controlled at will. This part of the work has been published in [J6,C11,C14,C16,P3].

The Chapter 3 of this dissertation addresses the process of designing material structures at mesoscopic scales that can provide unique outcomes when interacting with light. More specifically, we will show that particles with dimensions on the order of the optical wavelength, but contain high-refractive-index-contrast internal compartments, can be designed to efficiently control various characteristics of an optical field. We will demonstrate how through judicious particle design, one can control the scattering directionality, the state of polarization, the scattering strength, and diffusive scattering. These results have been published in [J1,J4,C5,C6,C8,C9,C12,C15,P1,P4].

Throughout Chapter 4, we will describe how the knowledge of light matter interaction at mesoscopic regime can be exploited to design optical sensing techniques. Understanding and controlling the statistical properties of the radiation is of paramount importance in the design of optical sources, detectors, and sensors. This chapter focuses on (i) quantifying the coherence of radiation emerging from random media and (ii) on using

these measurable coherence properties for surface and subsurface diagnostics. Traditionally, multiple light scattering is considered to wash out all structural information. However, contrary to this conventional wisdom, the field properties in close proximity of inhomogeneous media are influenced by the detailed structural characteristics. We will demonstrate that the near-field statistics render details of both the structural morphology and the distribution of large field enhancements. Creating and controlling extreme photonic states in all-dielectric materials is relevant not only to basic science, but also to efficient engineering of light sources, energy harvesting and sensing, and for enhancing other optical effects, this work has been published in [J5,C10,C12].

Moreover, the near-field coherence properties can also be an extremely effective tool for characterizing interfaces. In Chapter 4 we will demonstrate that the spatial extent of near-field correlations is a direct indicator of defect density in two-dimensional atomic lattices, as we have shown in [J8,C13]. At the end of Chapter 4 we will demonstrate experimentally that the effect of multiple scattering in passive near-field imaging can be effectively eliminated when the sample is illuminated with a dynamic spatially incoherent source, which has been published in [J7,C17].

CHAPTER 2
MESOSCOPIC OPTICS OF COMPLEX MEDIA: FUNDAMENTALS OF LIGHT-MATTER INTERACTIONS

2.1 Introduction

In-depth understanding of mesoscale phenomena provides the necessary quantitative explanations that neither microscopic nor macroscopic models of light-matter interaction can provide. Modeling mesoscopic systems is quite difficult because the properties of the systems can be efficiently manipulated by controlling the extent and the duration of interactions. Mesoscale optics provides a framework for understanding specific manifestations of wave phenomena such as interference and phase memory in complex media. Therefore, mesoscopic interaction models bring in the notion of fluctuations and rely on statistical descriptions, ensembles of realizations, etc.

By complex media we refer to materials whose optical properties vary significantly over the region of interaction with electromagnetic fields. These inhomogeneities can be deterministically structured or they can be randomly distributed. The periodicity of refractive indices can be imposed in one-, two- or three-dimensions and, as a result, the emerging optical properties are rather unique. First, their eigenmodes consist of an infinite number of space-harmonics with phase velocities varying from zero to infinity. Therefore, they support waves with very low phase velocity. Also it allows coupling wave with different wave vectors, because the structure has an inherent wave vector, $\kappa = 2\pi/\Lambda$ where Λ is the period of the structure that conserves the momentum in the coupling of waves. Second, periodic structures only support propagating waves in well-specified propagation

bands, which is called Bragg-reflection, and near the band edges the Bragg scattering gives rise to standing waves, i.e., waves with zero group velocity [16].

The second class of materials, the complex random media can, in most natural situations, be represented as collections of the scattering centers which are randomly varying in space and time. In other words, the medium is composed of a random distribution of many discrete constituents or particles. In this case each particle is excited by both the external electromagnetic field and by the fields scattered by all the other particles. In such a medium, the waves vary randomly in amplitude and phase. Traditionally, there are two main approaches to describe the multiple scattering inside random media. One is the radiative transfer theory which deals with the propagation of the intensity or, in the other words, the distribution of energy inside the medium. The other one, the multiple scattering theory or the analytical theory, deals directly with the wave propagation inside the medium [8,17,18]. Both approaches can be formulated in two steps. First, one calculates the scattering characteristic of a single scatterer such as scattering and absorption cross section and then, in a second step, one tries to account for the interaction effects due to many scatterers that are distributed randomly.

Unfortunately, for most realistic situations, there are no exact solutions for neither of these approaches and various approximations had to be developed. Choosing the appropriate approximation requires a careful examination of the length scales involved. The first parameter which has to be considered is the volume fraction or ratio between the wavelength of radiation, λ, and the average scatterer separation, d. In the tenuous regime, the scatterers can be considered as spatially independent and acting as uncorrelated objects.

In this case the particle density is low enough such that one can assume that the scattered wave is solely due to single scattering from the particles; multiple scattering can be effectively neglected and first order multiple scattering theory (single scattering theory) can be used [8]. However, by increasing the concentration, the scatterers interact with each other through the scattered electromagnetic fields to generate, depending on their specific locations, certain regularities in the overall scattered field [8]. Thus, to accurately describe multiple scattering in these media, we need to know both the properties of individual scatterers and their spatial distribution [8]. For even higher concentrations, even this collective scattering approximation fails. In the case of denser media, the scattering centers are in very close proximity of each other and can also interact through evanescent fields. This is clearly beyond the previous descriptions which considered the scatterers to act independently of their specific environment and were framed in terms of far-field scattering properties such as Mie cross-sections. Here we develop a novel propagation model in terms of measurable far- and near-field scattering property.

The complexity of mesoscale interactions often excludes any realistic theoretical description. Various approximation that can be handled analytically can become inadequate and one is forced appeal to numerical techniques. Various numerical methods such as the discrete dipole approximation (DDA), transition matrix (T-Matrix), the finite-element method (FEM), the finite-difference time-domain method (FDTD), etc. Each technique has its own pros and cons in term of the accuracy, computation time and the range of geometries to which it can be applied. For instance, for geometries which are rotationally or axially symmetric T-Matrix has significant advantage in terms of

computation time as opposed to DDA, FEM and FDTD. DDA, FEM modeling or the FDTD method, the accuracy of the solution depends on resolution-limited parameters such as the inter-dipole spacing or element length, in the T-matrix method as the scattered-field can be represented as a sum of vector spherical harmonics; hence, the accuracy of the solution will therefore depend on the truncation order. Another advantage of the T-Matrix technique is that the T-Matrix is the property of a particle, once it has been determined the scattered fields may be computed for any particle orientation without having to solve the problem from scratch thus it can be used to compute the scattered-field for many particles more rapidly in comparison to the other approaches. In this report we mainly use the T-Matrix method for the numerical calculation.

This method is one of the most accurate and efficient techniques for describing the light scattering by arbitrary particles, both single or cluster, based on directly solving the Maxwell's equations. In the T-matrix scheme, the incident and scattered fields are expanded in vectorial spherical wave function. The relation between the coefficient of the scattered field and the incident field is linear due to the linearity of the Maxwell equation and boundary conditions. The linear transformation which connects these coefficients to each other is known as the transition matrix [19,20].

This chapter will provide a brief survey of fundamental concepts, approaches and techniques specific to fundamental light-matter interaction at mesoscopic scales. The Chapter is organized as follows. First, we will discuss different regimes of light propagation through randomly inhomogenous media containing scattering particles of various concentrations. In particular, a novel description will be introduced to analyze

specific aspects of light propagation in dense composite media. Then, we will present evidence that the wave nature of light can be critical for understanding its propagation in unbounded highly scattering materials [21–24]. We will show that the perceived diffusion of light is subjected to competing mechanisms of interaction that lead to qualitatively different phases for the light evolution through complex media [25–27]. In particular, we will discuss implications on the ever elusive localization of light in three-dimensional random media and may also provide means to engineer materials where anomalous transport can be controlled at will. By their very nature, mesoscopic phenomena are usually non-Gaussian. It follows that they are rich in information but also that they may require specialized approaches. There are many manifestations of this nature, here we clarify the fundamentals of several specific phenomena.

2.2 Near-field Effects in Mesoscopic Light Transport

Due to scattering in complex media, the phase, amplitude, and frequency of waves change randomly in time and space. The magnitude and direction of the power flux density changes continuously. Without accounting explicitly for wave-like manifestations (diffraction or interference), the energy transport is described as the conservation of so-called specific intensity [8]. When the radiation propagates over a distance ds along the direction s, the specific intensity reduces with $dI = -\rho(\sigma_{sca} + \sigma_{abs})Ids$ due to scattering and absorption but, at the same time, it also increases because of scattering with probability $P(s', s)$ from different directions s' into s. There are no practical solutions for this radiative transport depiction in most realistic situations. However, an angular moments

expansion of the specific intensity leads to the ubiquitous description of diffusive transport [8]. This diffusion approximation is valid when the energy dissipation is minimal, the effective scattering is isotropic, and the source-detector separation is large compare to scattering length scales.

2.2.1 Different regimes of the light transport

The diffusive energy transfer is characterized by different scales. Aside from absorption l_{abs}. and scattering l_{sca} lengths, one also defines a transport mean-free path $l^* = l_{sca}/(1-g)$ as the scale over which the isotropic diffusion establishes. The scattering asymmetry parameter g is defined [28] as the average of the cosine of the scattering angle $g \equiv \langle cos\theta \rangle$. At this scale, the directional energy flux is randomized through successive scattering events. It is because of this randomization that details of particular interaction events are averaged out and simple energetic arguments provide an acceptable description of light propagation. A common representation of energy transport depicts the process as a classical random walk of particles of energy, photons [29]. The dynamic properties of this diffusion of photons can be described in terms of the scattering and dwell times involved and the associated velocities for phase, group, and energy transport [30,31].

Structural properties of random media determine different regimes of mesoscopic light transport. When the separation between scattering centers is much larger than the wavelength, the scattering events are considered to be independent. In this independent scattering approximation (ISA) the transport mean-free path $l^*_{ISA} = [n_o \sigma(1-g)]^{-1}$

depends only on the number density n_o of scattering centers, the optical cross section σ of an individual scatterer, and the asymmetry parameter, or mean cosine angle, g of a generic scattering event [28].

As the concentration of scatterers rises, the inter-particle distances decrease and their spatial locations become correlated leading to possible local interferences. The phase correlation between the scattered waves weakens the effective cross-section below that of an individual scattering event. This collective scattering (CS) is quantified by the structure factor $S(q)$ determined by the pair-correlation function characterizing the spatial distribution of the scattering potential. In this case, the scattering phase function is renormalized $\widetilde{P}(q) = P(q)S(q)$, which, in turn, modifies the effective scattering cross-section $\sigma_{CS} = \int P(q)qdq$. The renormalization of the scattering process leads to a coherent correction $l_{CS}^{*} = [n_0\sigma_{CS}(1 - g_{CS})]^{-1}$ for the transport mean free path. The correlated particles can, therefore, be regarded as collections of pseudo-scattering centers that are characterized by a modified scattering form factor [32,33]. In this interpretation, there is no further interaction between these fictitious scatterers. The interference between the scattered waves can increase the forward scattering and weaken the effective cross-section below that of an individual scattering event, $\sigma_{CS} < \sigma$. Positional correlations then lead to significantly large (wavelength dependent) transport mean free paths, which are responsible, for example, for the relatively large conductivity of disordered liquid metals [34,35] or the transparency of the cornea to visible light [36,37]. However, short-range order can also lead to an enhanced effective cross section and negative values of the asymmetry parameter as it has been recently shown in experiments in colloidal liquids [38]

and amorphous photonic materials [39,40]. The wavelength dependence of CS scattering is also the origin of natural structural coloration [41–43].

Multiple scattering effects are not considered within the CS description. As the particle density increases, the actual field incoming towards the scatter includes not only the initial external field but also the fields scattered by the surrounding particles. In analogy with effective medium theories [44,45], different methods were proposed for homogenizing the environment, surrounding the location of a singular scattering event. A common approach is to use a modified form factor $P(q)$ corresponding to an isolated scatterer in a background with an effective refractive index, n_{eff}, and then use this information in conventional transport descriptions [39,42,46]. This refractive index homogenization eliminates the influence of the specific environment but a far-field description of scattering is still necessary.

At even higher densities, even this CS description fails [47,48] because, in close proximity, scattering centers can also interact through evanescent fields. This is clearly beyond the previous descriptions which not only consider the scatterers to act independently of their specific environment but also describe the scattering in terms of far-field properties such as Mie cross-sections. Thus far, a precise, quantitative depiction of scattering for the case when the particles are located in the near-field of each other is still missing even for the canonical example of spherical scatterers.

2.2.2 Numerical calculations of light transport using T-matrix

To set the limits for the conventional description of light transmission and to get quantitative insights into the physical situations typical to dense media, we first conducted systematic numerical calculations. Using a multiple sphere T-matrix (MSTM) FORTAN-90 code version 3.0 [20], we evaluated rigorously the field distribution inside 3D composite media containing various distributions of particles. For our simulations we used $200\ nm$ in diameter TiO2 (refractive index 2.67) particles distributed in air; N spherical TiO2 particles (total number 3000 to 12000) were randomly placed inside a cylindrical slab with circular cross section of radius R (ranging from $3.5\ \mu m$ to $7\ \mu m$) and thickness L ($1.35\ \mu m$ to $3.5\ \mu m$) while keeping the ratio of the number of the particle to the area of the slab fixed. In each of the cases under study the radius R was at least twice larger than the thickness of the slab ($R \geq 2L$) to make sure that the boundary of the slab does not affect the results. The slab was illuminated with a beam with Gaussian amplitude profile propagating along the axis of the cylinder with a beam width of $\omega_0 = 1.5\ \mu m$ ($\omega_0 < R/2$) and the wavelength $\lambda = 532\ nm$. The focal point of the beam was located on the axis of the cylinder 50 nm above its lower face (see Figure 1).

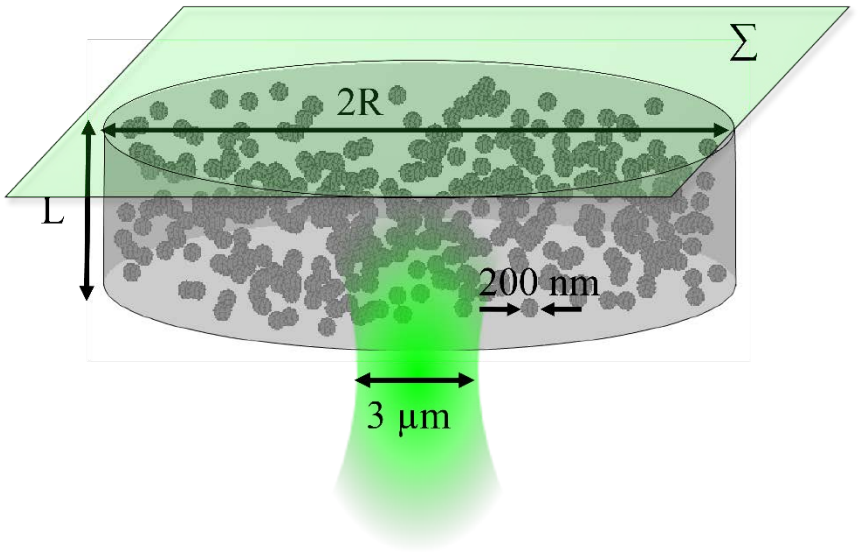

Figure 1: Schematic illustration of a model used for numerical calculation; N spherical 200 nm in diameter TiO_2 particles were randomly placed inside a cylindrical slab with circular cross section of radius R and thickness L. The slab is illuminated with a beam with Gaussian amplitude profile propagating along the axis of the cylinder with a beam width of $\omega_0 < R/2$ and the wavelength $\lambda = 532\ nm$. The focal point of the beam was located on the axis of the cylinder 50 nm above its lower face. The transmitted energy was calculated through the plane Σ

The calculations were performed on a UCF's Stokes parallel computer cluster using 260 to 340 processors. The time of calculations heavily depends on a number of particles and their concentration and typically took 5 to 30 hours. As a result of MSTM calculations, all six electric and magnetic complex field components were found in a plane Σ, 50 nm behind the cylindrical slab and in the radial cross section of the cylindrical slab. The transmitted energy was calculated on the base of known electric and magnetic fields as an overall flux (normal component of Poynting vector) through the plane Σ. Typical results are shown in Figure 2(a-c) for the situation where particles in different concentrations are distributed throughout a cylindrical slab with different thicknesses L. It is readily observed in the figure that, as the concentration of particles increases, the mean inter-particle

distance decreases and more and more localized coupling occurs between neighboring particles.

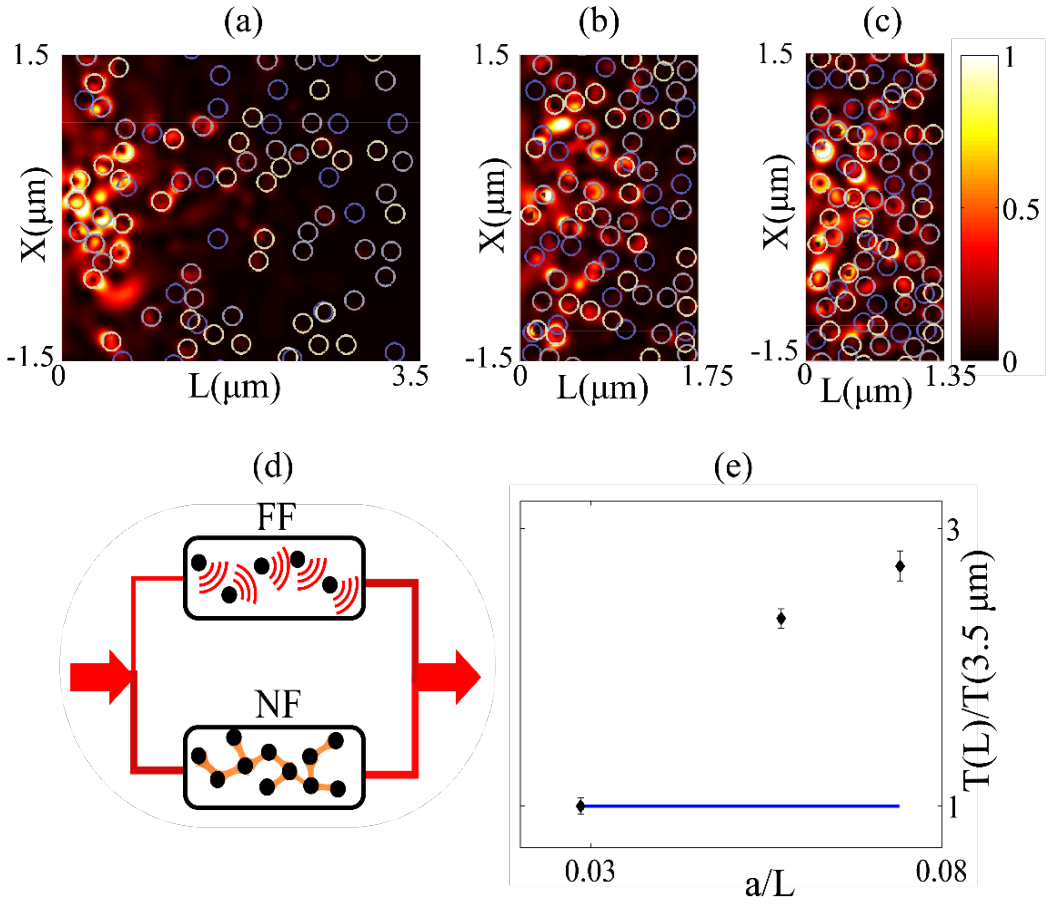

Figure 2: (a-c) Intensity distributions in the cross-sectional areas of 3D slabs with reducing lengths as indicated. The media contain $a = 100$ nm radius TiO_2 particles randomly dispersed throughout the volume. Rings colored in gray denote particles located in the considered cross-section while the white and blue ones indicate particles situated at 100 nm above and, respectively, below that plane. (d) Illustration of the appearance of additional transmission channels due to near-field coupling (see text). (e) Total transmission as a function of inverse thickness. The blue and black symbols designate the ISA and the results of T-matrix calculations, respectively

In the classical description of diffusive transport through a slab of volume V and area A, the transmission scales according to Ohm's law: $T \propto l^*/L = V/[N\sigma(1-g)L] =$

$A/[N\sigma(1-g)]$ [1]. This means that for a fixed ratio of area of the slab to number of particles A/N, the transmission is independent of the length of the medium. However, as apparent from the results of our simulations summarized in Figure 2(e), the transmittance actually increases. This process could be interpreted as a rise in the effective value of l^* or, alternatively, it can be described as the emergence of a different regime of mesoscopic transport.

When propagating in highly scattering media, optical waves comprise both homogeneous and inhomogeneous components. Thus, the energy is not only carried by propagating waves but it also evolves through evanescent coupling between individual scatterers. For linear random media, as scatterers become optically connected [47], near the onset of percolation, the near-field coupling between particles can be seen as an opening of new transmission, optically connected, channels as suggested in the Figure 2(d). High transmission through three-dimensional lattices of close packed spheres has been qualitatively explained as a percolation of light through overlapping whispering gallery modes [49]. In contrast with electronic systems, the appearance of optically connected channels is not expected to lead to percolation threshold phenomena [50]. Since power flow through both connected and scattering channels, the behavior of the transmittance should resemble that of thermal conductance of composites near percolation [51]: these new optically connected channels can be seen as adding parallel resistors to the (far-field) scattering channels (see Figure 2(d)). As a result, the opening of these additional channels increases the overall transmission:

$$T = T_{CS} + T_{NF} = (l_{CS}^* + l_{NF}^*)L^{-1}. \quad (1)$$

In terms of discrete scattering processes, one can consider two types of events: (i) conventional Mie-like scattering where the illumination is provided by a plane wave and (ii) scattering events excited by evanescent waves. Of course, correcting the total transmission in this manner is practically relevant only if it can be described in terms of physically meaningful and measurable quantities such as a near-field scattering cross-section $\bar{\sigma}_{NF}$.

There were several notable attempts to calculate analytically or evaluate numerically the scattering of evanescent wave by spherical objects [52,53]. It has been shown that the conventional Mie theory can be directly applied to scattering of evanescent waves through a complex angle rotation of the standard Mie solution [16,54]. In this approach, by rotating both the direction and the distribution of the incident electric $\vec{E}(\vec{r}) = \hat{R}_y(-\gamma)\vec{E}\left[\hat{R}_y(\gamma)\vec{r}\right]$ and magnetic $\vec{H}(\vec{r}) = \hat{R}_y(-\gamma)\vec{H}\left[\hat{R}_y(\gamma)\vec{r}\right]$ fields by the complex angle, γ a z propagating monochromatic plane wave can be transformed into an evanescent wave. Thus, including this transformation in the conventional Mie calculation, one can readily find the results of the scattering of evanescent electromagnetic waves from spherical particle. We note that, due to the exponential decay of the evanescent wave, the scattering has some atypical features. In standard Mie scattering, because of the spherical symmetry, there are no cross-polarization terms in the scattering matrix. In the evanescent scattering however the exponentially decreasing amplitude introduces an asymmetry, which leads to such polarization mixing. Moreover, as opposed to standard theory, the Mie coefficients do not necessarily decrease with their order and the magnetic terms could actually be enhanced [32].

This demonstrates that σ_{NF} can be not only measured experimentally but it can also be easily evaluated numerically in the case of a spherical scatterer. To calculate evanescent waves scattering, a Mie scattering code was implemented in MATLAB that accommodates complex angle rotations. An example of the scattered electromagnetic field is illustrated in Figure 3 for the case of a spherical particle with refractive index $n = 2.51 + i0.28$ *and radius*$r = 500\ nm$ placed on top of glass prism (refractive index $n = 1.5$). The angle of incidence onto glass-air interface of the prism was $60°$ that ensured the condition of total internal reflection. In Figure 3(a) and (b) we present the intensity distributions of the scattered field at $2\ \mu m$ above the structure for the p-polarized and s-polarized incident field, respectively. The polarization dependent behavior specific to evanescent illumination is evident.

The predictions of this modified Mie scattering approach were also verified experimentally. We conducted measurements on a spherical particle in the conditions similar to those in calculations. In the experiment, the intensity distributions were measured across a $5\times5\ \mu m$ plane situated at $2\ \mu m$ above the particles. For this purpose we used a Nanonics MultiView 4000 near field scanning optical microscope (NSOM) working in standard collection mode using a Cr-Au coated tapered silica fiber probe with $50\ nm$ aperture diameter. The test particles were placed on the surface of a prism ($n = 1.5$) and illuminated in total internal reflection by a slightly focused $532\ nm$ laser beam. Typical experimental results are summarized in Figure 3(c) and (d) and show a good agreement with the numerical calculations. In particular, the dependence of scattered field on polarization of incident wave is quite noticeable.

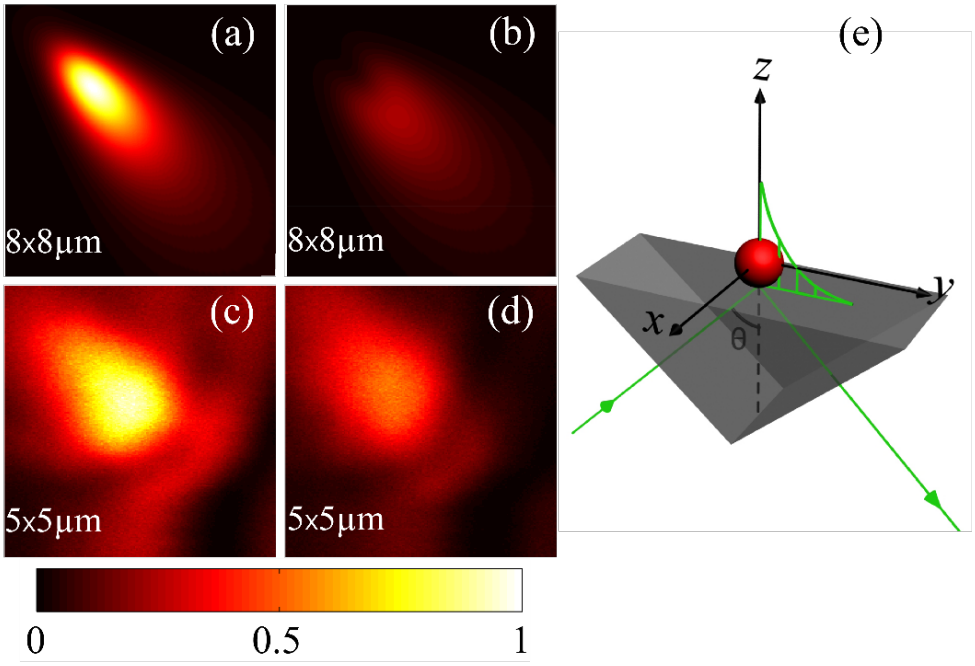

Figure 3: Far field intensity distribution of a 500 nm radius particle exited with evanescent waves. (a-b) Simulation results for the p-polarized and s-polarized incident field, respectively. (c-d) Experimental results for the p-polarized and s-polarized incident field, respectively (e) schematic of experimental setup. All calculations and measurement are for $\lambda = 532\ nm$ and refractive index of $n = 2.51 + i0.28$ and $n = 1.5$ for particle and prism respectively. The angle of incident on glass-air interface was $\theta = 60°$

Grounded on the complete description of the scattering process including both homogeneous and inhomogeneous excitation, one can re-interpret the transport phenomena. Of course, particles can interact through evanescent waves only if they are in close proximity of each other. The process should therefore depend on both the number of scatterers per cubic wavelength $n_0\lambda^3/n$ and the strength of evanescent coupling determined by the average inter-particle distance d [55], which, in turn, is set by the number density n_0. The probability for evanescent transfer can then be written as $p_{NF} =$

$n_0(\lambda^3/n)e^{-\kappa d}$ where κ is the characteristic attenuation length for the evanescent waves. Thus, in the model where the light is transmitted through propagating and evanescent channels one can re-define the transport mean free path as

$$l^*_{CS+NF} = \frac{1}{n_0\sigma^*(1-g^*)} + \left[\frac{p_{NF}}{n_0\sigma_{NF}(1-g_{NF})}\right]. \quad (2)$$

Because the decay rate of the evanescent waves depends on the incident angle, an average $[\overline{\ldots}]$ is taken over the angular domain defined by the refractive indices of the particle and its surrounding medium. Moreover, as we mentioned before, the near field cross-section and the asymmetry parameter are both polarization dependent and, therefore, the values in Eq. (2) are also averaged over the two polarization states.

In practice, the complex angle rotation described before can be used to evaluate scattering properties such as scattering cross-sections and asymmetry parameters. These values can then be used in Eq. (2) to evaluate the transport mean free path for media with different particle concentrations. It is worth mentioning here that l^* is the only directly measurable quantity in a multiple-scattering experiment such as, for instance, enhanced back scattering (EBS).

2.2.3 Enhanced back scattering measurement

To verify the accuracy of our model, we conducted an EBS experiment on colloidal media with increasing concentrations. We used aqueous suspensions silica particles with average diameter of $1\ \mu m$. The schematic representation of the experimental setup is shown

in Fig. 2(a). A collimated laser beam with $\lambda = 476nm$ passes through a beam splitter and through a filter consisting of a linear polarizer followed by a quarter wave plate. The circular-polarization filter insures that no single-scattering contributions are collected. The circularly polarized beam further impinges on a glass cuvette containing colloidal suspension. The back-scattered light is deflected by the beam splitter and then is focused by a lens with $250\ mm$ focal length on the plane of a CCD array (520 × 480 pixels array). During the measurements, an ensemble average is performed by recording typically 100 different data frames.

We chose to use EBS measurements because this technique uses a backscattering mode, which requires only a 'one-side-open' geometry in contrast to classical transmission, which involves samples with different thicknesses and also requires maintaining identical structural characteristics for colloids of high concentration. Also, EBS is a so-called monostatic-scattering technique, which allows the light source and detection system to share the same optical axis and, therefore, offer a high degree of compactness suitable to measurements on both liquid-like and solid-like media.

The colloidal systems consist of relatively monodisperse silica (SiO_2) powders. The average diameter of the particles was $0.84 \pm 0.1\ \mu m$ and the density, obtained by nitrogen pycnometry, was 2.1 g/cm^3 (Geltec Company). The silica slurries were prepared in an aqueous solution of 0.03 M $NaNO_3$, and the pH was adjusted to the desired value using Fisher brand NaOH and HNO_3. The pH adjustments were performed in one direction only. The volume fraction of the solids was determined from the weight fraction and the density of the particles. The powders were added to the suspending fluid slowly while mixing the

sample by shaking and vibration. After the addition of all the powder, the pH was adjusted to the nominal value, and the samples were sonicated for about four minutes with an ultrasonic sonicator and was agitated for 16 hours in a rotational mixer. During the mixing period, the samples were sonicated for about four hours periodically in a bath sonicator. There was no indication of any presence of air bubbles inside the samples after preparations. In all experiments the pH was determined before the measurements, and no significant changes in the pH were detected. The amorphous samples showing no sign of crystallization were placed in standard spectroscopic cuvettes right before the optical measurement.

The schematic of the experimental setup is shown in Figure 4(a). A collimated laser beam with $\lambda = 476nm$ passes through a beam splitter and through a filter consisting of a linear polarizer followed by a quarter-wave plate. The circular-polarization filter insures that no single scattering contributions are collected. The circularly polarized beam further impinges on a 1cm path glass cuvette containing the suspension under study. The light scattered from the cuvette is reflected by the beam splitter and then focused by a lens with 250mm focal length on the plane of a CCD array with 520x480 pixels. During the measurement, an ensemble average was performed by recording 100 different data frames.

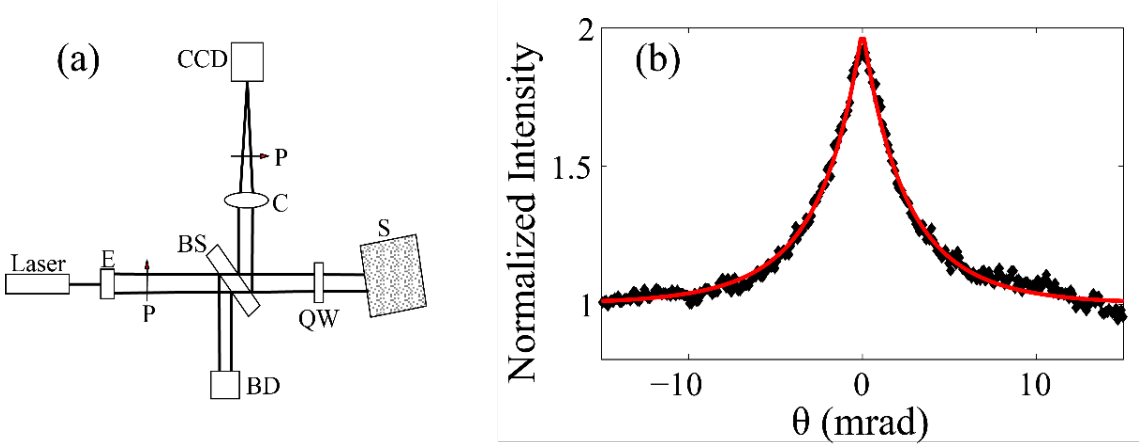

Figure 4(a) Enhanced backscattering (EBS) setup; (b) Enhanced backscattering cone, black diamond are experimental data and the red curve is best fitted of equation 3 to the experimental data.

In Figure 4(b), we present a typical cone of enhanced-backscattered intensity corresponding to volume fractions of 35% of spherical silica particles. The functional forms of the cones were well fitted with a theoretical dependence derived in the frame of a diffusion theory and having the transport mean free path l^* as a fitting parameter [10]

$$\alpha_c(\theta) = \frac{5}{4\pi}\frac{1}{1-\beta}\frac{1}{\frac{2}{3}l^*\kappa_\perp+1}\left(\frac{1}{1+l\kappa_\perp}-\beta\right), \quad (3)$$

where $\beta = 1 - l/l^*$ and $\kappa_\perp \cong \frac{2\pi}{\lambda}\theta$. The values obtained for the transport mean free paths corresponding to different particle volume fractions are summarized in Figure 5(b) in the main text.

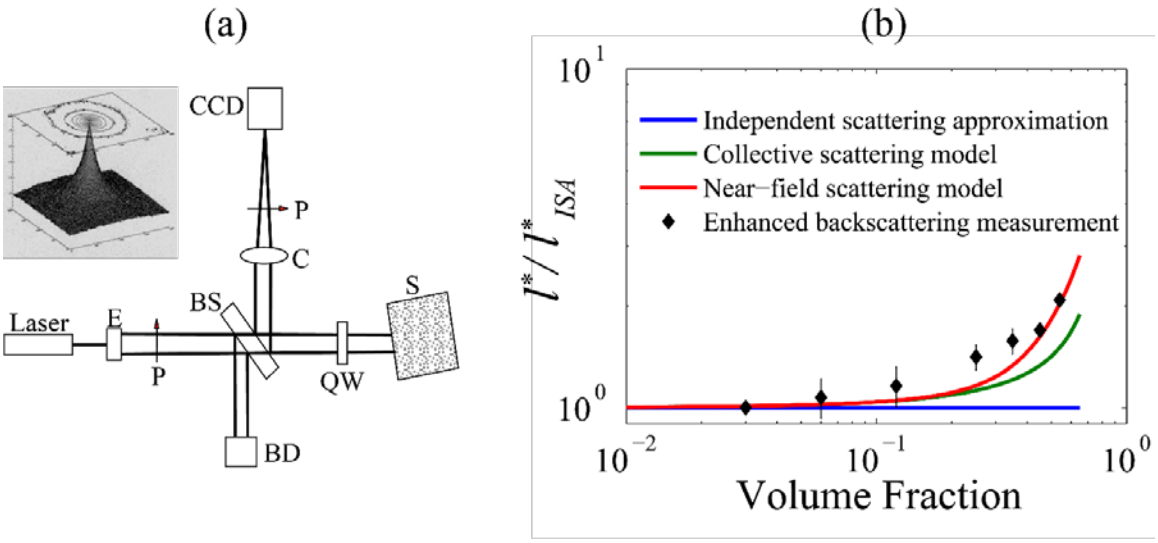

Figure 5: (a) Enhanced backscattering setup. Abbreviations are as follows: E, beam expander; P, polarizers; BS, beam splitter; BD, beam dumper; QW, quarter-wave plate; C, Fourier lens; S, sample. (b) Measured transport mean free path compared with predictions of different transport models.

It is known that the shape of the EBS cone and, hence, the recovered mean free path depends on the average interface reflectivity [10]. However, in the specific case of the interface between a colloidal suspension and the glass cuvette, we estimate the range of reflectivity to be between R=0.009 for glass-water and R=0.0031 for glass-silica. Thus, the corrections for internal reflections are minimal. Moreover, in colloids, the effective reflectivity also depends on the scattering anisotropy of individual particles. In our case, the anisotropy factor is g=0.95, which reduces even more the effect of index mismatch [56].

The results corresponding to different colloidal concentrations are summarized in Figure 5(b) where the experimental l^* values are normalized to the corresponding ones evaluated in the ISA framework. As can be seen, when increasing the concentration of the particles, the measured transport mean free path starts to deviate from both the ISA predictions and the estimations based on the CS correction model. On the other hand, our

near-field transmission model shows a remarkably good agreement with the experimental data. The remaining minor differences may attribute to experimental conditions such as internal reflection [56,57] and potential sample non-uniformities [58,59]. We note that this experimental demonstration augments the significance of our previous numerical calculations: the increase of l^* values due to additional near-field coupling is apparent in both transmission and reflection. At high volume fractions, both experimental and numerical data clearly illustrate the failure of the conventional description of scattering solely in terms of propagating waves.

2.3.4 Conclusions

In conclusion, we have quantitatively described the characteristics of multiple light scattering in dense composite media where particles are located in close proximity and interact through evanescent near fields. We have shown that a new regime of transmission emerges, which can be described in terms of physically meaningful and measurable quantities such a near-field scattering cross-section σ_{NF}. In this regime, additional transmission channels open because of the near-field interactions between scatterers placed in close proximity [22].

A full-scale calculation of the electromagnetic field distribution in 3D random media indicates the emergence of additional channels for energy transfer. The model is also supported by the results of a comprehensive EBS experiment. We found that the transport mean free path corresponding to different concentration of scatterers is in very good agreement with our model for near-field corrected transport. The use of such detailed

descriptors for individual scattering events not only improves the macroscopic description of light propagation in random media but it also enhances the predictive capabilities of light transport models.

2.3 Phase Transitions in Diffusion of Light

The way the electromagnetic (EM) waves propagate through disordered media is a topic that has been thoroughly examined. Different regimes were identified ranging from quasi-ballistics to diffusive to different kinds of anomalous diffusion including the progression towards a complete arrest of propagation [8,60–62].

Can anything new be said about this problem? It turns out that describing the complicated multiple scattering processes required significant simplifications. A more careful examination of aspects specific to EM fields has recently led to discovering new phenomena [22,63,64].

When EM waves encounter complex media, the properties of emerging radiation depend not only on the *structural characteristics* of the material system but also on the *scales of interaction* (temporal and spatial). Evidence for different regimes of propagation is routinely presented by modifying the material systems and examining the corresponding forms of interaction [65,66]. The effect of the interaction scales is analyzed by imposing macroscopic constraints on the size of the system, which usually leads to a number of additional problems unrelated to the intrinsic nature of interaction, e.g. boundary effects [57,67,68].

But, in fact, the properties of EM fields evolve as the radiation penetrates deeper into a medium, even if the randomness is statistically stationary. The simplest example is the gradual change from ballistic to diffusive regimes of propagation [69–71]. One can expect that a careful inspection of how light propagates may indicate transitions even between different regimes of diffusive propagation. Here we demonstrate the existence of different phases of evolution in the way light diffuses through effectively semi-infinite media. We will show that these "phase transitions" are direct consequences of competing mechanisms of interaction between light and complex media.

2.3.1 Normal diffusion of light

When disregarding the wave properties of light, the diffusive transport can be modeled as a random walk of photons with an associated diffusion coefficient D describing the root mean square spread of the photon density [8,72]. The path-length distributions of backscattered photons at the surface of a semi-infinite disordered medium, estimated at the same location of an impulsive source, is $p(s) = (4\pi Dc)^{-\frac{3}{2}} z_e s^{-\frac{5}{2}} \exp(-\mu_a s) \exp(-\frac{r^2+z_e^2}{4Ds})$, where μ_a and z_e account for possible losses and for boundary-specific effects, respectively [73]. For asymptotically large s, this means that $\log\big(p(s)\big) = A - \frac{5}{2}\log(s)$. The power law decay with a -5/2 exponent is the hallmark of "normal" photon diffusion. Examples of this behavior a plentiful ranging from random lasing [74], to image reconstruction [75–77] and biology and medicine [78,79] .

2.3.2 First transition: from normal to anomalous

In strongly multiply scattering materials, wave properties cannot be neglected anymore. Constituent scatterers do not modify the field properties individually. Rather, they start acting collectively modifying the nature of local interferences. Moreover, waves can propagate along reciprocal multiple scattering paths generating additional interferences seen as closed loops in their trajectories [80–82]. This increased probability of returning to the starting point has the net effect of slowing down the "normal" diffusion.

Note that, aside from the deterministic account of a diffusive process, light propagation can be described stochastically as a random walk of photons. In this interpretation, the departure from "normal" diffusion can be portrayed as an anomalous distribution of scattering steps leading to super-diffusion [83]) or as an abnormal distribution of waiting times before random jumps occur. The later can be due to either long dwell times (e.g. scattering resonances) or looping (recurrent scattering), rendering the propagation sub-diffusive [31,84].

The slowing down of "normal" diffusion is the situation encountered in strongly scattering media and can be modeled using a scale-dependent diffusion coefficient. Based on the scaling theory of localization, the optical diffusion coefficient varies with the size L of the system as $D = D_0 l \left(\frac{1}{\xi} + \frac{1}{L} + \frac{1}{L_a}\right)$, where l is the transport mean free path, ξ is the coherence length and L_a is the absorption length [85–87]. In reflection, the effective size L of the explored medium is determined by the root mean square (RMS) distribution of the energy spread $R = \sqrt{6Dt}$; thus for systems with negligible losses and before reaching localization, $L \ll \xi$, one could show that the path-dependent diffusion coefficient becomes

$D(s) = (\frac{D_0^2 l^2}{6c})^{\frac{1}{3}} s^{-\frac{1}{3}}$, which for, large s, leads to $\log(p(s)) = B - 2\log(s)$. Therefore, the transport of light deviates from normal diffusion and approaches a regime where the energy diffuses slower than normal and the path-length distribution decays as s^{-2}. As depicted in Figure 1, this change in the $p(s)$ behavior indicates the first phase transition in the diffusion of light: from normal to anomalous.

2.3.3 Second transition: from anomalous back to normal

In many situations, composite media are so densely packed that individual scatterers are in close proximity and become optically connected through strong near-field (NF) interactions. This situation leads to a new regime of transport where the energy diffuses also through additional evanescent channels [22]. Moreover, reports also suggest that the vector character of light has a critical role in establishing this interaction regime [63,64]. All these very recent developments may help clarify the elusive strong localization of light in three-dimensional photonic structures [88].

As discussed before, at high concentrations of scattering centers, there is a finite probability for light to pass more than once through the same particle. Such recurrent scatterings sequences can be imagined as loops of energy flows inside the medium, which determine the overall sub-diffusive nature of energy transport. On the other hand, the NF coupling between scattering centers has the tendency to destroy these loops by leaking energy into new transmission channels [22]. Of course, the longer the path inside the medium, the more loops can be created but also more NF coupling events can occur. As a result, the loops of energy flows along longer paths are destroyed more and more and light

propagation gradually returns to a regime of normal diffusion. This constitutes a second phase transition in the diffusion of light: from anomalous to normal.

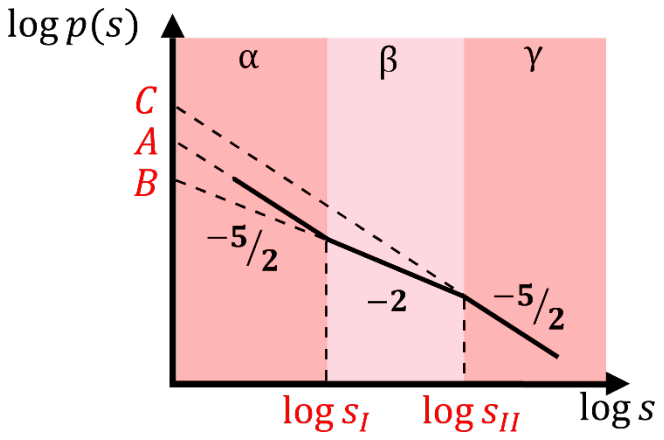

Figure 6: Distinct regimes of light propagation through complex media are characterized by path-length distributions having specific power-law dependences. Phase transitions may occur between normal (α,γ) and anomalous (β) diffusions.

The evolution of path-lengths distribution through these phase transitions is generically depicted in Figure 1. Let us comment on the meaning of the extrapolation constants A and C that depend on the values of the two "normal diffusion coefficients before and after the phase transitions. From the general solution for $p(s)$ one finds that $\mathrm{A,(C)} = \log\left(\left(4\pi D_{A,(C)}\right)^{-\frac{3}{2}} z_e\right)$, where D_A and D_C are the diffusion coefficients before the 1st and after the 2nd transition, respectively. It is evident that $D_C < D_A$. This means that, even though the normal diffusion is eventually recovered, because of the anomalous slowing down at intermediate ranges, light practically expands over larger areas at lower pace than if the diffusion would have been normal all along. This could open up new possibilities to control the large-scale propagation.

We note that for any diffusion, including the "passive" diffusion of photons, one can associate an effective temperature at which the process evolves [89]. Then, the return to normality in region (γ) corresponds to reaching the thermodynamic equilibrium at large scales. Moreover, one can say that the diffusing photons reach the thermodynamic equilibrium at lower effective temperatures because of the "cooling down" during the evolution at intermediate scales (β).

The other extrapolation value indicated in Figure 1 is $B = \log\left(\left(4\pi(\frac{D_A^2 l^2}{6})^{\frac{1}{3}}\right)^{-\frac{3}{2}} z_e\right)$ and, from $\mathrm{A} - \mathrm{B} \propto \log(s_I)$, it follows that $\log s_I \propto \frac{l^2}{D_A}$. It is interesting to comment on the meaning of $\mathrm{C} - \mathrm{B} \propto \log s_{II}$. This quantity, measures in fact the "duration" or spatial extent of the anomalous diffusion $s_{II} = s_I \left(\frac{D_A}{D_C}\right)^3$ and, most interestingly, it can be accessible experimentally as we will show in the following.

2.3.4 Experimental demonstration

The sub-diffusive behavior of light has been demonstrated in a number of photonic structures [87]. Here we establish experimentally the presence of the 2nd phase transition. Usually, light transport in disordered scattering media is examined by techniques providing macroscopically averaged properties such as transmission. Thus, one cannot say much about the way the diffusion evolves in steady-state. Clarifying this evolution requires access to detailed information about the distribution of paths the optical waves take throughout the medium. Direct measurements of the probability density function of radiation path-lengths can be performed interferometrically [90].

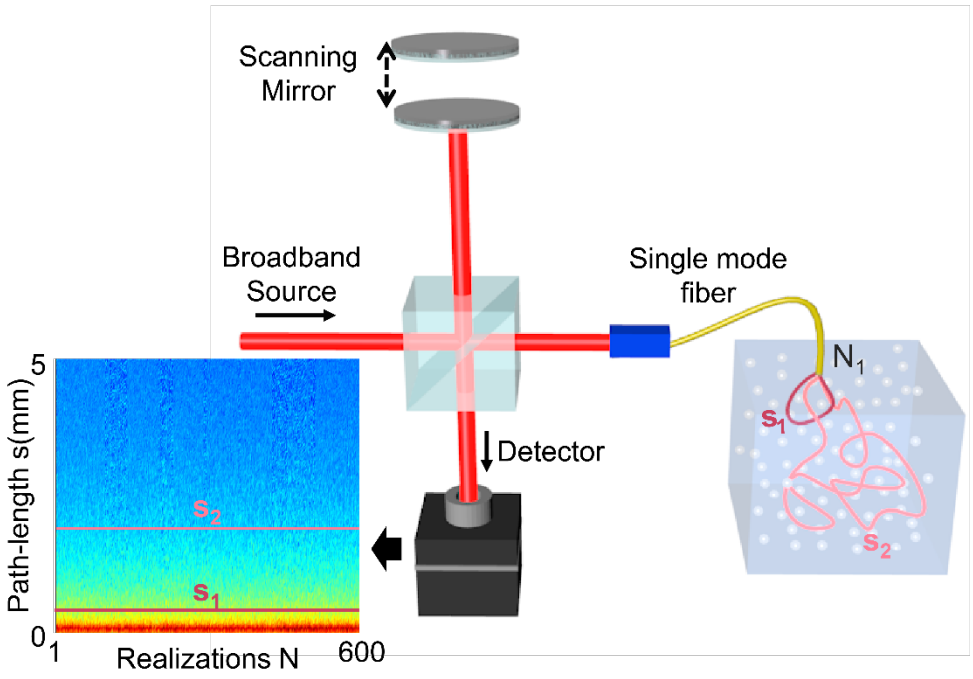

Figure 7: A single-mode fiber-based low-coherence interferometer allows direct measurement of path-length distributions in reflection from a semi-infinite medium. An ensemble average is created over measurements at different locations.

Using a broadband light source in conjunction with a single-mode fiber optic-based Michelson interferometer as illustrated in Figure 2, we directly infer the distribution of path-length of multiply scattered light. Notably, dynamic ranges of more than five orders of magnitude can be readily obtained with a corresponding temporal resolution of 30fs. In backscattering from semi-infinite media, the coherence gating permits isolating the contribution from optical paths of specified length s and, therefore, the corresponding probability density $p(s)$ are directly determined. The measurement configuration corresponds to the situation where the point source and point detector coincide. An ensemble average can be constructed over realizations of the medium or over measurements at different locations as suggested in Figure 2.

To study systematically the occurrence of these phase transitions, we examined solid media which were specifically designed to maintain prescribed volume fractions of well-dispersed, alumina surface treated TiO_2 submicron particles. Here we present data on samples composed of 5% to 50% volume fractions of 300nm diameter TiO_2 particles embedded into a polymer matrix (Latex). Spectra were recorded using a broadband source with a bandwidth of 30nm centered on a wavelength of 1310 nm. Measurements were performed over more than six hundred different regions of the samples, to ensure appropriate ensemble average.

The main results are summarized in Figure 3. As explained before, the optical path-length distribution associated with normal diffusion through a semi-infinite medium should exhibit an $s^{-5/2}$ asymptotic dependence. This is exactly what is observed for low TiO_2 concentrations for more than two decades of path lengths.

However, as the concentration of particles increases, this behavior begins to change: in the short path-length domain the power law exponent starts to deviate from $-5/2$ and approaches -2. This evolution towards a time-dependent diffusion coefficient is anticipated according to theories on wave localization, as we discussed before [87]. The progression is more evident as the TiO_2 concentration increases indicating significant contributions from recurrent scattering or loops of energy flows. This unmistakable sub-diffusive behavior of light propagation in 3D random media is a clear signature of an incipient regime where coherent wave effects cannot be neglected anymore.

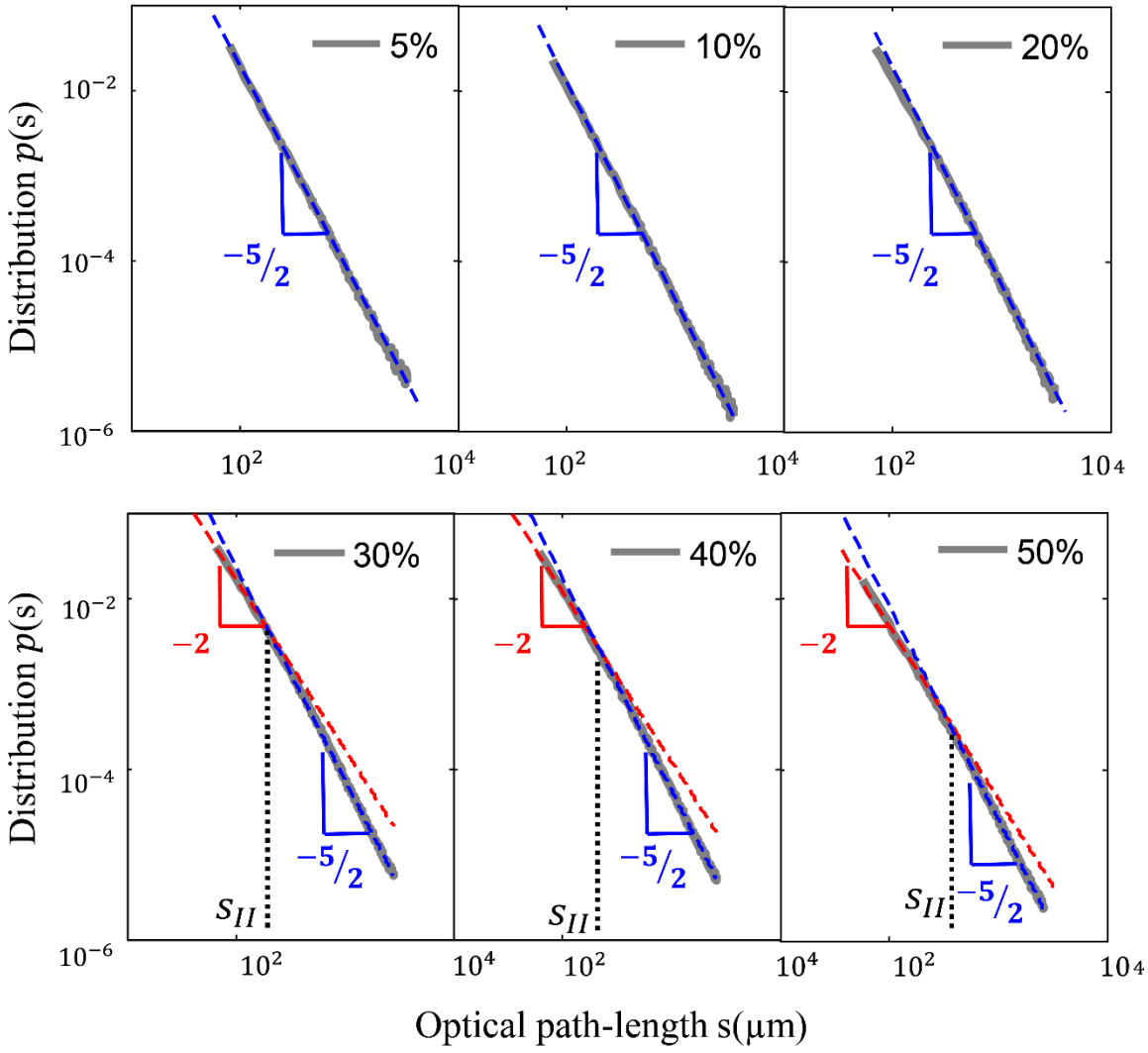

Figure 8: Experimental probability distributions of path-lengths corresponding to semi-infinite random media comprising dispersions of TiO_2 particles with different volume fractions as indicated. The black dotted lines at 233.6μm, 326.7μm and 395.9μm indicate the s_{II} values corresponding to 30%, 40% and 50% volume fractions of TiO_2 particles, respectively.

But most remarkable in Figure 3 is the conversion back to an asymptotic $s^{-5/2}$ decay. This cross-over represents the first experimental evidence for the second phase transition from anomalous back to normal diffusion, which we anticipated in the preceding discussion. Microscopically, it can be explained by realizing that when scattering particles are in close proximity of each other they start interacting through their evanescent fields.

This additional interaction opens up new channels for transferring the energy throughout the medium [22]. Recovering the diffusive behavior for longer optical paths is a consequence of the tradeoff between the competing mechanisms of recurrent scattering and NF coupling.

2.3.5 Discussion

Let us now discuss in more detail the conditions in which these two phase transitions occur. The probability for a wave to return close to its starting point (recurrent scattering) should be independent of the geometry of a measurement. This probability is determined solely by the ratio between the trajectory volume and the volume explored by light inside the multiple scattering medium [91]. In reflection from a semi-infinite medium, longer paths penetrate through larger volumes and, therefore, the size of the explored medium evolves as $V_m(s) \propto L^3(s)$. The linear scale of this medium expands as $L(t) = \sqrt{6D(t)t}$ with a diffusion coefficient $D(t) = (\frac{D_B^2 l^2}{6})^{\frac{1}{3}} t^{-\frac{1}{3}}$. It then follows that $L(t) = \left[6(\frac{D_B^2 l^2}{6})^{\frac{1}{3}} t^{-\frac{1}{3}} t\right]^{1/2} = \sqrt[3]{6} D_B l t^{1/3}$, which, in terms of the length of trajectories, means that $L^3(s) = 6(D_B l)\frac{s}{c}$. In these conditions, the probability of recurrent scattering becomes

$$p_\times = \frac{V_{tr}}{V_{m(s)}} = \frac{\lambda^2 s}{L^3} = \frac{c\lambda^2}{6lD_B} = \frac{\lambda^2}{2l^2}\,, \qquad (4)$$

which is independent of the path-length. In other words, once the diffusion becomes scale-dependent, the probability of recurrent scattering does not depend on the path-length.

In fact, because, in reflection, there are no constraints on possible trajectories, one can also find $p_\times$ using simple mesoscale arguments [91].

We note that the situation is quite different when the size of the explored medium is a constant V, as in the case of a transmission measurement. The probability of trajectory crossing in this case would be given by the ratio $p_\times = \frac{V_{tr}}{V} = \frac{\lambda^2 \cdot s}{V} \propto s$. It depends linearly on the length of trajectories because of the macroscopic constraint imposed by the finite size of the medium.

Let us now analyze the near-field coupling, the competing mechanism that inhibits recurrent scattering. At high volume fractions of particles, the energy can leak out of the diffusive channels because of the near field interactions between scatterers situated at less than a wavelength apart. To determine the associated probability, let us consider a typical propagation channel of length s and cross-section λ^2. Due to NF interactions, energy can leak out of this channel that at $\frac{s}{\lambda}$ locations. The strength of NF coupling to particles outside the trajectory is measured by the total area A_{NF} of potential interactions, which, in turn, is determined by the size of the near-field cross-section σ_{NF} and the number of such possible events. In other words, $A_{NF} = \sigma_{NF} \cdot (3n_0\lambda^3)$. At each location along the trajectory, the process happens with an efficiency dictated by ratio between A_{NF} and the total area $A = 2\pi\lambda^2$surrounding a typical location. Thus, the probability of energy leaking along the entire trajectory of length s is

$$P_{leak} = \frac{3\pi n_0 \lambda^3 \times \sigma_{NF}}{2\pi\lambda^2} \frac{s}{\lambda} = \frac{3}{2} n_0 \bar{\sigma}_{NF} s. \quad (5)$$

Aside from optical size, the near-field cross section $\overline{\sigma}_{NF}$ accounts for angular and polarization averaging [22].

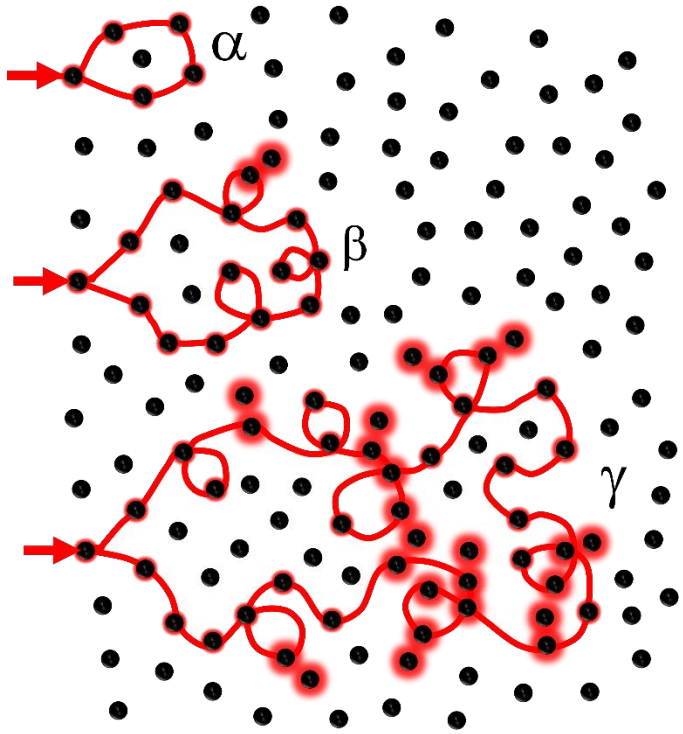

Figure 9: Competing mechanisms of interaction dominate different stages of transport evolution. Initially, the wave starts to expand normally (α) but then loops of energy flow are created with a certain probability (β). The competing mechanism of energy leaking destroys these loops and dominates at even larger scales of interaction (γ).

Notably, the probability in Eq. (2) does increase with the length of the trajectory as opposed to the crossing probability in Eq. (1). It means that, as the path-length through the medium grows, the rate at which loops are destroyed can exceed the rate at which they are created! Eventually, the "anomaly" caused by recurrent scattering ceases and the diffusion recovers its normal behavior with a diffusion constant that is scale-independent. This is the

second phase transition of light. The different stages of transport evolution are schematically illustrated in Figure 4.

It is also instructive to examine these two probabilities in the context of the number density of scattering centers. Clearly, because $l \sim 1/n_0$, the probability of recurrent scattering $p_\times$ depends quadratically on concentration, i.e. $p_\times \sim n_0^2$. The leaking probability on the other hand grows linearly with both concentration and path-length, $p_{leak} \sim s n_0$ as seen in Eq. (2). As the threshold for the 2nd phase transition can be set when these two probabilities become comparable, from $P_{leak} = P_\times$ it follows that

$$S_{II} = \frac{2\lambda^2 \sigma^2 n_0}{3\bar{\sigma}_{NF}}. \quad (6)$$

It can be concluded that this transition happens at larger and larger path-lengths when n_0 increases. When using Eq. (3) for 30%, 40% and 50% volume fractions of TiO_2 particles, one finds that S_{II} is, respectively, 227.7μm, 303.6μm and 379.5μm, in very good agreement with the s_{II} data extracted experimentally and shown in Figure 3.

In closing we will like to comment on diffusion as a general concept associated with evolution. Most common is, of course, the particle diffusion starting from the Brownian one but the concept expands to social phenomena and, of course, waves. Waves bring in certain specific manifestations but the parallel with particle diffusion is always meaningful and instructive. In this context, the two phase transitions in the diffusion of light discussed here bare a strong similarity with the phenomenon of particle diffusion in spatially-correlated random potentials [92–95]. At short times, particles execute a free, Brownian-like diffusion before encountering any influence from the external, constraining

potential. However, once the spatial dispersion reaches scales comparable with the correlation length of this potential, the diffusion starts to slow down. One could argue that, at these intermediate scales, the particles' diffusion is somewhat "caged". This can happen because an externally applied random potential [96–98], the structural inhomogeneity of gel-like media through which the particles diffuse [99,100], or simply because of the direct influence of particle crowding [101,102]. In the long-time limit, the particles eventually tunnel through these potential cages and the normal diffusion recovers, as expected at the asymptotic thermodynamic equilibrium [103]. These three regimes of diffusion are equivalent to the three stages of path-length evolution depicted in Figure 6 and Figure 9.

The different evolution stages of EM wave transport also bear similarities with the thermalization of matter waves due to atomic collisions. In this case, even when the interaction is weak, an atomic cloud released in a disordered potential never reaches a localized stationary state [104].

2.3.6 Conclusions

Light interaction with complex media is a unique testbed for a variety of physical phenomena and the physics of multiple scattering phenomena is periodically revisited. This is perhaps because technology advances permit uncovering situations previously unattainable. Our results demonstrate the existence of unexplored regimes for wave propagation through complex media. Going beyond traditional random walk descriptions, the circumstances we created provide access to new aspects of the universal process of diffusion in external potentials.

We have shown that the propagation of waves in unbounded systems is naturally subjected to opposing mechanisms of interaction. As a result, the diffusive-like evolution of optical waves encompasses different phases. The process is similar to the diffusion of particles subjected to additional time-dependent random potentials. In the case of electromagnetic waves, the locally strong interferences create an effective random potential that constrains the overall diffusion of waves. Our results demonstrate that the average residence time in this confining potential is regulated by the strength of the inherent evanescent coupling between microscopic parts of the complex medium. In particular, we have shown that strong recurrent scattering due to on-shell propagating fields is impeded by strongly localized evanescent couplings (off-shell wave manifestations). The fact that transport of optical waves cannot slowdown indefinitely is of high relevance for the elusive Anderson localization of light in three-dimensional media [105].

We presented a microscopic model that describes the phenomenological diffusion of electromagnetic waves in random media and provides a familiar thermodynamical description similar to an equilibrium fluctuation-dissipation relation. Aside from its fundamental relevance, understanding all the wave aspects governing such interactions could lead to new means to engineer materials where the nature and the extent of anomalous transport can be controlled at will.

2.4 Summary

The intricate process of light interacting with complex random media is fascinating both for unveiling fundamental physics in systems easy to control experimentally and for

a plethora of technological applications. Because of the complex light scattering phenomenology, modeling is an invaluable tool. This is commonly done by using the detailed small-scale characteristics of the composite (usually simplified to spherical Mie scattering) to generate macroscopic descriptions of transport properties. The progress, however, is hampered by the need to characterize scattering properties in conditions closer to reality, i.e. at mesoscopic scales where scattering centers can be in the near-field of each other.

Here, we have quantitatively described the characteristics of multiple light scattering in dense composite media where particles are located in close proximity and interact through evanescent near fields. We present a novel propagation model that is developed in terms of measurable far- and near-field scattering properties. The use of such detailed descriptors for individual scattering events improves the macroscopic description of light propagation in random media and enhances the predictive capabilities of light transport models. We also study how optical signal might change when the light propagates through larger volumes of the mesoscopic system. It was a long time belief that, with increasing the scattering strength of multiple scattering media, the transport of light gradually slows down and, eventually, comes to a hold corresponding to a localized state. Here we present experimental evidence that different stages emerge in this evolution, which cannot be described by classical diffusion with conventional scaling arguments. A microscopic model captures the relevant aspects of electromagnetic waves propagation and explains the competing mechanisms that prevent the three-dimensional wave localization.

We demonstrate that strong evanescent-field couplings hinder the localization of wave resonances and, therefore, impede the slowing down of diffusion [25].

CHAPTER 3:
ENGINEERING MATTER AT MESOSCOPIC SCALES: EFFICIENT CONTROL FOR PROPERTIES OF LIGHT

3.1 Introduction

The main focus of this Chapter is guiding the process of designing material structures that can provide unique outcomes when interacting with light. Structural modifications of mesoscale systems can be used in order to control the interaction between light and matter and, as the result, to control the properties of the scattered light. The question is, why structuring the material system could help us to achieve extreme optical properties without having to impose uncommon values for the intrinsic optical properties of the material?

Modifying optical scattering, in particular, can be achieved by tuning the structure of the mesoscopic system at the level of single scatterer, for example, by sculpting the internal three-dimensions of multimaterial micro- and nano-particles. By tuning the morphology of an isolated particle one can achieve micro or nano internal structures with different refractive indices. Therefore, the number of reflections or refractions inside the particles would be increased and, as a result, the phase distribution of the scattered waves would be broader. Thus, this new set of scattered waves can interfere constructively or destructively in specific directions, which gives rise to new optical properties for the scattering particle. Moreover, these structured elements constitute the building blocks for adjusting the collective interactions in multiple scattering regimes where most important applications of composite materials exist.

Moreover, by modifying the spatial distribution of a collection of particles one can affect the characteristics of the scattered waves. In general, manipulating the spatial distribution of the ensemble of scatterers, will change locally the average scattering properties determined by the pair-correlation function and the structure factor. In turn, this will affect the multiple scattering processes and will give rise to new optical properties.

The overall goal of this chapter is to guide the process of designing material structures that can provide unique outcomes when interacting with light. It should be pointed out that in this study we will mainly address the linear non-dissipative interactions, such as scattering of electromagnetic wave in linear dielectric media. Since scattering is the major theme, a very brief overview would be helpful.

As result of the interaction of electromagnetic wave with a heterogeneous medium (inhomogeneous in the scale of interaction), some energy from the waves will transfer to the medium. This is known as elastic scattering if the medium reradiates this energy with the same frequency. If the radiation frequency changes, these phenomena are described as quasi-elastic or inelastic scattering. In both cases, the electromagnetic wave will be re-radiated in all directions but with different weights. In this transferring process, the medium may transform the radiation energy into other forms of energy, such as heat. This is typically the phenomenon of absorption. The total amount of energy transferred into the medium through scattering and absorption is measured by the radiation's extinction (extinction = scattering+ absorption) [28,106]. Here we briefly review the different approaches that can be used to calculate the scattering of electromagnetic wave from a single particle.

To explain the scattering from single particle we should first clarify what we mean by a particle. Conventionally a homogenous object smaller or comparable with the wavelength of the incident light is known as a particle. An object with well-defined optical properties, size and shape is known as a particle.

To describe the scattering from an individual particle we have to consider the fact that the particles are isolated, far enough from each other such that light interacts with one single scatterer at the time and the effect of multiple scattering is neglected. In order to understand the physics of scattering by an individual particle let us consider an arbitrary particle illuminated with an electromagnetic wave. The oscillating electromagnetic field induces dipoles in the particle which are also oscillating at the frequency of the incident field. Therefore, they emit radiation in all directions with different phase and amplitude. The result of the interaction of these wavelets, very far from particle, is known as scattering pattern. The phase and amplitude of these wavelets depend on the material property of the particle, and the phase relation between these wavelets depends on the size, shape and the scattering direction [28,106–108].

To describe quantitatively the properties of the scattered light in far field, one needs to define parameters such as scattering function, scattering cross section, and scattering phase function. When an arbitrary particle is illuminated with a plane electromagnetic wave, at distance much larger than the particle size and incident wavelength, the scattered waves appear as spherical waves which are centered by the particle with different phase from the incident wave. One of the properties of this scattered wave is its intensity, *I*, which is the energy flux per unit area. Therefore the energy flow at far distance from the particle

through a spherical surface element is equal to $Ir^2 sin\theta d\theta d\varphi$, which is proportional to the intensity of incident field I_0 which can be written as [106]:

$$Ir^2 sin\theta d\theta d\varphi = I_0 \left(\frac{\lambda}{2\pi}\right)^2 F(\theta, \varphi, \lambda) sin\theta d\theta d\varphi, \quad (7)$$

where λ is the wavelength of the incident wave and $F(\theta, \varphi, \lambda)$ is the dimensionless scattering function which depends on optical property, size and shape of the particle and the wavelength of the incident wave. It should be pointed out that by knowing only the intensity of the scattered wave one could not characterize the scattered wave, some other optical properties of the scattered wave such as polarization and the phase are also needed.

The strength of the interaction between the electromagnetic field and the particle is quantified by the so-called scattering cross section. Let the total energy scattered in all directions by particle be equal to the energy of the incident beam falling on the area C_{sca} [28]:

$$C_{sca} = \frac{1}{I_0} \int_0^{2\pi} \int_0^{\pi} Ir^2 sin\theta d\theta d\varphi = \frac{1}{(2\pi/\lambda)^2} \int_0^{2\pi} \int_0^{\pi} F(\theta, \varphi, \lambda) sin\theta d\theta d\varphi, \quad (8)$$

which has the dimension of the area, and it can be larger or smaller than the particle's geometrical cross-section. The ratio between the scattering cross section and the geometrical cross section is a dimensionless parameter known as scattering efficiency, $Q_{sca} = C_{sca}/S_g$, where, S_g is the geometrical cross section.

The differential scattering cross section, $\frac{dC_{sca}}{d\Omega}$, or in other words, the phase function, P, is the amount of energy for the unit incident irradiance scattered in the unit

solid angle which identifies the angular distribution of the scattered light, $\int_{4\pi} P\, d\Omega = 1$ [28].

To summarize, scattering from a single particle depends on the size, refractive index, the shape of the particle, and the wavelength of incident light. There are many different methods and approximations to calculate the scattering from a single particle; here we very briefly summarize a few of them.

Mie Theory (Rigorous Solution): This approach is an analytical solution of the vectorial electromagnetic problem of the interaction between a plane electromagnetic wave and spherical and homogeneous particle embedded into a non-absorbing medium. In other words, the Mie solution is the solution of the Maxwell's equations in the spherical coordinate with a suitable boundary conditions. It should be pointed out that there is no size limitations for scattereres in Mie scattering theory [28,109].

Rayleigh scattering (The Zeroth-order Approximation): This is also known as the dipolar approximation of the particle response in the quasi-static picture. Technically, this approximation applies to particles much smaller than the wavelength of light for which each part of the particle experiences the same excitation field, which is uniform in time and space. In these conditions, the incident electromagnetic field induces an oscillating electrical dipole inside the particle which radiates in all directions with the same intensity [89,91].

Rayleigh Debye-Gans scattering (The First-order Approximation): This is the regime in which the size of the particle is larger and its shape is arbitrary but the phase or the amplitude of the incident wave do not change considerably after the interaction with

the particle. Moreover, this approximation requires that the refractive index of the particle is close to that of the surrounding medium such that the phase difference between different parts of the particle is independent of the material property and it is determined by their position. The main difference between the Rayleigh and Rayleigh Debye-Gans scattering is the angular distribution of the scattered light [16, 18].

Geometrical optics: In this approach the particle size is much larger than the incident wavelength which is illuminated by plane waves. Therefore, nee can describe the plane wave illumination in terms of a large number of rays. By using the Snell's law and the Fresnel equation at the particle-medium interface one can determine the path of each light ray through the particle. The rays that take different paths are out of phase with each other and can therefore interfere constructively and destructively. Of course, each ray that enters the particle can also experience successive reflections or refractions [16].

Particle diffraction (The Large-end Approximation): When the size of the particle is much larger than the wavelength of incident light, the edge effects play the main role in redistributing the energy. As such, an incident beam of light will bend when it passes around the edge of the particle, which is the essence of the phenomenon of diffraction. Therefore, in this case one can use various diffraction theories to describe the scattering pattern [108,110].

In this chapter, we will demonstrate how to design the internal structure of a single spherical scatterers to obtain unique outcomes when interacting with the electromagnetic waves. First, we will show that large size, core-shell dielectric structures with spherical symmetry provide the necessary flexibility for exciting higher-order spherical modes and,

consequently, allow us to control the directivity of the scattered radiation [111,111–113]. Significant scattering can be generated over angular domains that were formerly believed to be accessible only to dipolar scattering. Then, we will demonstrate that a thermally induced in-fiber fluid instability permits creating multimaterial photonic particles by a precise allocation of high-refractive-index-contrast materials at different radial and azimuthal coordinates within three-dimensional structures. Exploiting this unique capability in all-dielectric systems, one can tune the scattering cross-section of eqi-sized particles via radial structuring, and induce polarization-sensitive scattering from spherical particles with broken internal rotational symmetry. In the last section of this Chapter, we address another functionality that can be realized at the level of individual scattering structures. We will demonstrate how an angularly symmetric power flow can be achieved around heterogeneous composite particles [114–116].

3.2 Directional Control of Scattering by All-Dielectric Core-Shell Spheres

The optical size and the intrinsic material properties of scattering particles introduce inherent restrictions on their scattering patterns. In this Chapter we will show that large size, core-shell dielectric structures with spherical symmetry provide the necessary flexibility for exciting higher-order spherical modes and, consequently, allow controlling the directivity of scattered radiation. Significant scattering can be generated over angular domains that were believed to be accessible only to dipolar scattering.

The direction in which optical fields propagate is usually controlled by optical elements like mirrors, prisms, lenses, etc. operation on the basis of reflection, refraction or

diffraction [117]. A deterministic change in the direction of propagation is easily accomplished but it requires specific alignment or realignment of the optical elements.

Propagating light also changes its course due to scattering. The directionality of the outgoing flow of energy is determined by the direction of incident light and by the material properties and the length scales involved in the interaction between light [28,106] and scattering particle. Thus, in common cases such as scattering off small particulates, the size of the particle determines in great degree the way in which the light is scattered or redirected [118].

In this context, an interesting question can be asked. Can one have scattering objects with the same size which can direct the flow of energy differently? It turns out that dipolar particles much smaller than the wavelength are one such example. These subwavelength and spherically symmetric particles have remarkable electric and magnetic Mie resonances. The subsequent interference between these electric and magnetic modes leads to specific angular distributions of the scattered fields. Notably, unique scattering features have been demonstrated for particles characterized by (I) zero backscattering, (II) minimum forward scattering, and (III) zero asymmetry parameter [107,118–127] [15, 27-35]. Nevertheless, such dipolar particles are also quite ineffective in manipulating the light because of their inherent weak scattering ability.

From a practical perspective, one would like larger particles to scatter more efficiently and would prefer the natural isotropy of spherically symmetric structures which do not require any alignment. In addition, in many situations, lossless materials may be desired in order to minimize other dissipative processes. Unfortunately, due to

restrictions imposed within the Mie scattering theory, such size and shape requirements impose severe limitations in the angular distribution of scattering.

In the following we will show that modifications in the internal structure of large particles permit not only tuning the extinction cross section but, importantly, allow to significantly control their scattering directivity. This task can be achieved using appropriately designed core-shell structures made of realistic and lossless dielectric materials. We will show that dielectric core-shell structures with similar macroscopic sizes can have both high scattering efficiencies (high Q) and radically different scattering phase functions.

We start by briefly reviewing the conditions in which small particles manifest specific scattering behavior. The simplest situation when manipulation of scattering directionality is possible is the case of particles which can be described just with electric and magnetic polarizabilities. Examples of such particles could be sub micrometer semiconductor particles in visible or near-infrared spectral range [119,120]. In this case, the contribution of higher-order multipolar modes is negligible and the scattered field is the superposition of electric and magnetic dipolar emissions. In particular, the case of zero backscattering (type I) occurs when the electric and magnetic dipoles have the same magnitude and oscillate in phase. Due to the nature of this dipolar radiation, their contributions interfere constructively in the forward direction and destructively in the exact backward direction: forward scattering is enhanced while backscattering is completely suppressed. In terms of Mie coefficients $a_n = |a_n|e^{i\gamma_n}$ and $b_n = |b_n|e^{i\delta_n}$ [106], this zero

backscattering condition is also known as the 1st Kerker condition (Huygens sources) and it requires that:

$$a_1 = b_1. \quad (9)$$

When the electric and magnetic dipoles have the same strength but oscillate anti-phase, the backward interference becomes constructive while the forward one is reduced (it does not vanish completely as required by the optical theorem). This is the case of so-called minimum forward scattering (type II) which is described as the 2nd Kerker condition:

$$|a_1| = |b_1|,\ \gamma_1 - \delta_1 = \pi. \quad (10)$$

Finally, the type III scattering corresponds to the situation where the average cosine of the scattering function is zero, i.e. the so-called asymmetry parameter $g \equiv \langle \cos\theta \rangle = 0$. For small particles, one can show that $g \propto 3\{|a_1||b_1^*| \cos(\gamma_1 - \delta_1)\}/2$ and, therefore, the scattering will be symmetric in forward and backward directions if the electric and magnetic dipoles emissions have a quarter-wave phase difference:

$$\gamma_1 - \delta_1 = \frac{\pi}{2}\ . \quad (11)$$

We note that the first two circumstances require the contribution from two dipoles, one electric and one magnetic, which oscillate in- or out- of phase. The zero-asymmetry however is also observed in the isotropic radiation of a single electric dipole. Note here the difference between "isotropic scattering" and the "$g = 0$" conditions.

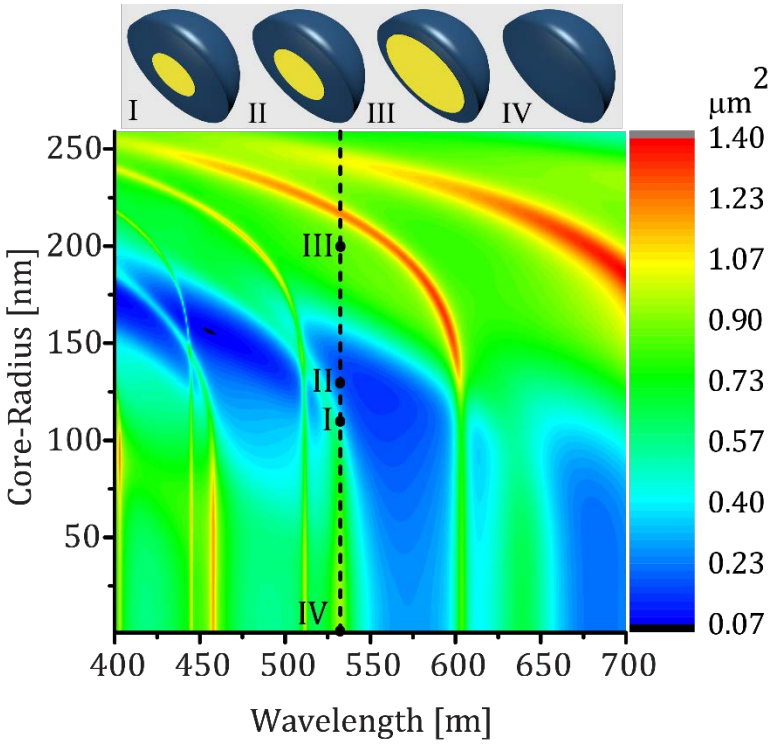

Figure 10: Color map of scattering cross section as a function of core radius and wavelength corresponding to core-shell particles with 520 nm outer diameter and refractive indices of 1.5 and 2.5 for core and shell, respectively. Positions of dots indicate particles with corresponding cross-sections of the structures illustrated at the top. The core radii are (I) 110 nm, (II) 130 nm, (III) 200 nm, (IV) a solid sphere with index of refraction 2.5 and radius 260nm

Some of the above mentioned scattering conditions have already been demonstrated for homogeneous, dipolar, spherically symmetric particles [128–130]. In Ref. [126], metal-dielectric core shell particles were employed to create ultra-directional forward scattering (type I scattering). To achieve this, the authors of Ref. [126] used a concept similar to Eq. (2) trying to equate electric and magnetic Mie coefficients for higher multipoles.

Nevertheless, many practical situations require redirecting significantly larger amounts of energy. This necessarily entails bigger particles which have higher scattering cross section (see Figure 10 cross section line). Unfortunately, by simply increasing the size of the particle it is impossible to satisfy all three types of scattering in visible region.

This can be seen for instance in Figure 11 where cross-section line corresponding to a solid sphere (zero core radius) exhibits primarily forward scattering.

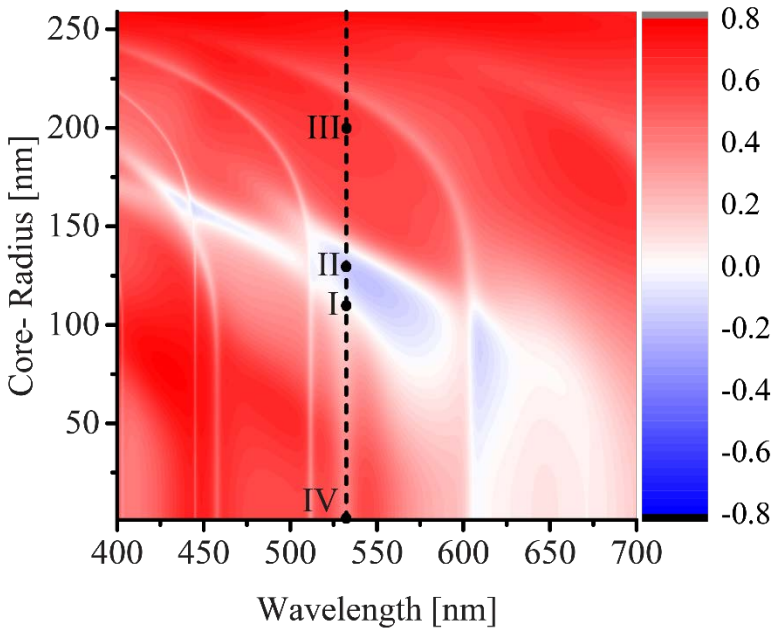

Figure 11: Color map of the asymmetry parameter as a function of core radius and wavelength corresponding to core-shell particles with 520 nm outer diameter and refractive indices of 1.5 and 2.5 for core and shell, respectively. Positions of dots indicate particles with corresponding structure as in Figure 10

The question is, can one cover all three very different scattering regimes while maintaining significant scattering cross-sections? As we will see in the following, the task can be achieved by changing the internal structure of the scatterer and transforming it into a core-shell spherical particle. Moreover, in certain cases, a structured particle can even have a higher scattering cross section than the corresponding solid sphere. The performance of core-shell structures is illustrated in Figure 10 and Figure 11, which depict, as color maps, the main scattering characteristics, scattering cross-section and asymmetry parameter, as functions of both the core radius and the wavelength of illumination. Let us

note that the scattering cross-sections of the discussed structured particles are between one or two orders of magnitude larger than those of magneto dielectric particle reported earlier [131,132].

As can be seen in Figure 11, the asymmetry parameter of core-shell particles can be positive, negative (as low as -0.2), or zero thus covering the different types of scattering denoted by I, II, and III. Meanwhile, from Figure 10 one can see that the scattering cross-section for corresponding particles remains large and comparable to the one of solid sphere. It is worth to mention that we have suggested a structure with the negative value of g in visible region, which can reduce the transport mean free path for a medium composed of such particles. Let us note that negative asymmetry parameter ($g \approx -0.04$) was also found in Ref [124], in visible region for lossless dielectric sphere with refractive index of 2.2 which is much smaller in module compared with what we present here for the core shell spherical particle. Also in Ref [124] the authors predict lower negative asymmetry parameter but requires using higher refractive index materials which are accessible only in infrared region.

We would like to point out that, because of the dimensionality of the scattering structures, the analysis of the Mie scattering coefficients is more involved than the simple dipolar description in Eqs. (3), (4) and (5). An entire spectrum of higher order multipoles is necessary to describe the scattering phase functions as illustrated in Figure 12 for the specific cases marked in Figure 10 and Figure 11. A direct predictive analysis appears to be difficult. However, from the magnitude and phase of the Mie coefficients shown in Figure 12, one could realize that, for a solid spherical particle, the first several multipoles

(up to hexadecapoles for our specific examples) have dominant contributions and that their magnitudes usually decrease with increasing the multipole order. This is not always the case for core-shell particles.

However, the problem of scattering by core-shell particles can also be considered from a different perspective. For large particles, the overall scattering properties can be understood as the result of multiple scattering between effective elements of a complex dielectric structure. This is similar to the classical problem involving three-layer optical thin films (where shell could be thought as two outer layers). It is known that judicious adjustments of materials and thicknesses leads to overall effective properties (refractive index and phase accumulations) that cannot be realized using a single layer material [133]. Most importantly, a simple three-layer combination of two different materials can create an effective optical layer with a variety of equivalent phase thicknesses and with an effective refractive index that can be lower or larger than any of the constituent indices.

This Fabry-Perot problem can be recast using vector spherical harmonics to describe the scattering from core-shell structures. For instance, a Debye scattering series approach has been used to describe the scattering of light by coated spheres [134].

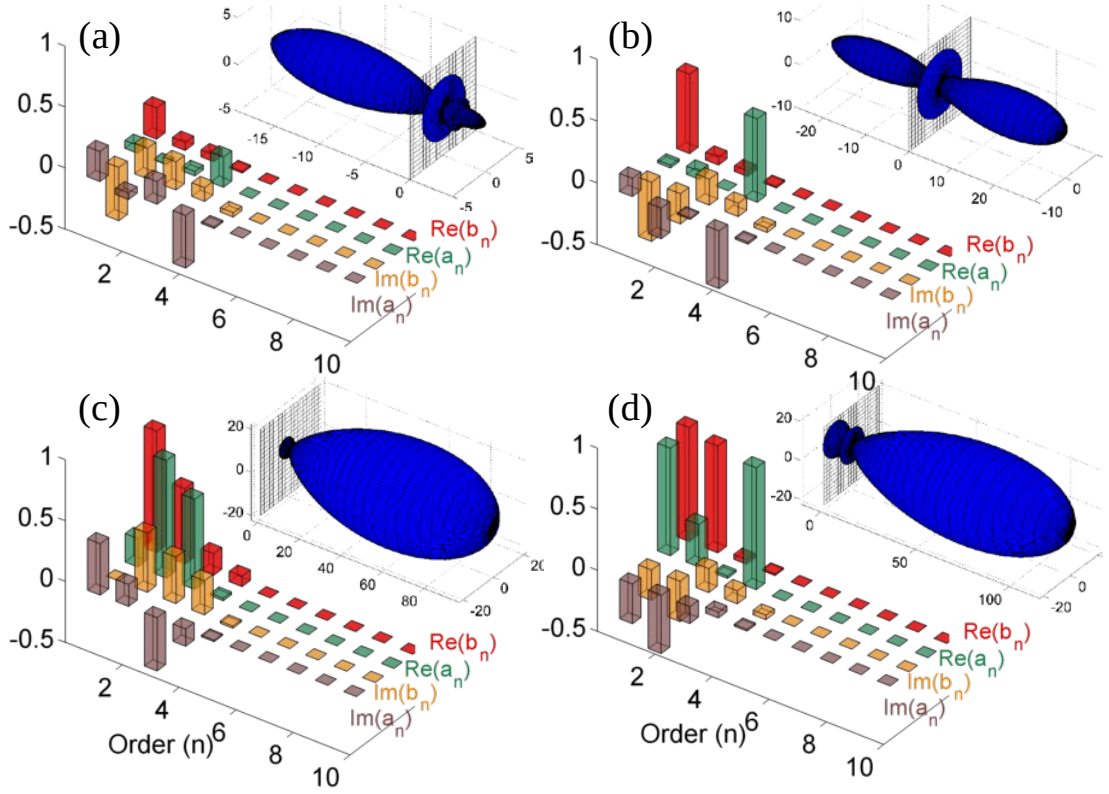

Figure 12: Real and imaginary part of electric and magnetic Mie coefficients corresponding to a 520 nm diameter core-shell spherical particle with refractive indices of 1.5 and 2.5 for core and shell, respectively. The core radii are (a) 130 nm, (b) 110 nm, (c) 200 nm, (d) a solid sphere with index of refraction 2.5 and radius 260nm. All calculations are for λ=532nm. Insets show the corresponding scattering phase functions

The scattering diversity seen in Figure 12 is introduced by the core-shell interface which constitutes an additional interaction surface for the partial waves describing the scattering. At a specific wavelength, the optical properties of a core-shell assembly are, in fact, determined by a multiple scattering process involving essentially four different optical sizes [134,135]. The order of scattering depends on these effective sizes and controls the emerging phase diversity. A heavier multiple scattering leads to a broader distribution of phases across different multipolar contributions and, consequently, increases the diversity of scattering patterns that can be generated by the core-shell structure. This is exemplified

in Figure 13where we show the internal field distributions corresponding to the structures with the same parameters as in Figure 12. As can be seen, the electric field distribution inside the particle changes due to internal multiple scattering which affects the contributions of different higher-order multipoles. This, in turn, changes significantly the far field emission pattern.

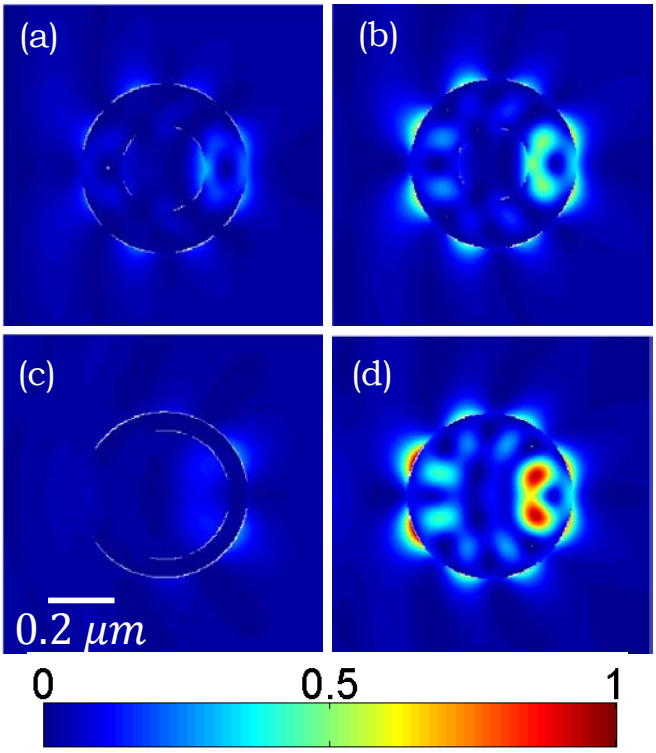

Figure 13: Internal intensity distributions calculated for the core-shell spherical particles as in Figure 10.

It should be emphasized here that the properties of the simplest spherical composite – a core-shell structure – can cover a parameter space broader than the one corresponding to a solid sphere of any acceptable material. This includes the three special cases mentioned in the preamble, which cannot be attained in the case of solid spheres with dimensions of

the order of the wavelength. The insets in Figure 12 depict the scattering phase functions that can be achieved when changing the core size of a 520nm diameter particle demonstrating that very directive scattering can be achieved. For example, in the case of the minimum forward scattering the forward to backward scattering ratio is 0.24 which is in the same order as reported in Ref [128] for dipole-size solid silicon particle satisfying 2nd Kerker condition. Note that, contrary to Ref. [126], the structures considered here are purely dielectric.

Moreover, the exclusive scattering performance can be obtained with lossless dielectric materials having refractive indices as low as 2.5. It is remarkable that, even for modest refractive index contrasts and for relatively large particles, all these very different scattering patterns can be realized by changing only the thickness of the shell while maintaining the outer diameter and incident wavelength constant.

The examples presented in this Chapter demonstrate that a viable design strategy could be developed to control angular field distributions, which makes use of the broader parameter space available for core-shell structures [111]. Core-shell dielectric structures with spherical symmetry provide the necessary flexibility in exciting higher-order spherical modes providing therefore means to control the directivity of scattered radiation. It is worth mentioning in closing that the proposed structures could be practically implemented by taking advantage of novel fabrication pathways [136].

What's more, an inverse scattering problem can be cast based on conventional field matching conditions at the spherical shells boundaries [137]. It will be demonstrated that the inverse problem can be solved starting from the external Mie coefficients $a_n =$

$\frac{1}{2n(n+1)}\int_0^{\pi}[S_2(\theta)\tau_n(\theta)+S_1(\theta)\pi_n(\theta)]\,sin\theta\,d\theta$ and $b_n=\frac{1}{2n(n+1)}\int_0^{\pi}[S_2(\theta)\pi_n(\theta)+S_1(\theta)\tau_n(\theta)]\,sin\theta\,d\theta$, where $S_1(\theta)$ and $S_2(\theta)$ are the chosen scattering amplitudes. Then, by recombining the boundary conditions to eliminate the internal Mie coefficients, one can find the combination of refractive indices, core, and shell radii which provides the desired angular scattering. This should permit a significant flexibility in designing spherically symmetric dielectric structures capable to control at will the directivity of scattered radiation.

3.3 Control Over the Optical Scattering Efficiency in Core-Shell Particles

To date, tailoring the optical scattering efficiency Q_{sca} (defined as the ratio of the scattering to geometric cross sections [28]) from particles have relied on either changing their size or refractive index. Realizing high Q_{sca}, as necessary, for example, in optical coatings to achieve opacity in thin layers without absorption, typically requires increasing the refractive index, an approach fundamentally limited by naturally available materials [138]. Recently, it has been shown that using the in-fiber fluid instabilities [136,139,140], one can produce spherical particles having – in principle – arbitrary internal structure. In this approach, a centimeter-scale axisymmetric cylindrical 'core' rod is assembled as a prototype of the intended particle structure from pre-fabricated segments of different materials, which is then embedded in a cladding matrix to form a 'preform' [141–143]. A fiber that is thermally drawn from this preform with reduced transverse feature size defines the initial conditions for a cylinder-to-sphere geometric transformation by thermally inducing the Plateau-Rayleigh capillary instability

(PRI) [144,145] at the heterogeneous interfaces along the whole fiber length [139,146]. Since the geometric morphing associated with this fluid instability is predictable, the axially symmetric core is converted into spherical particles with a target architecture that follows from the macroscopic preform structure. This processing strategy permits to radially control the layer thicknesses in multilayered particles and also allows to azimuthally control the structure in particles with discrete rotational symmetry.

We examined the possibility that multilayer dielectric particles with controlled radial structure and high refractive-index-contrast (*without* incorporating metals) can provide control over Q_{sca} solely through the internal architecture. This point is made clear through a calculation of Q_{sca} at a wavelength $\lambda = 532$ nm for a core-shell particle of fixed radius $a = 500$ nm (polymer-core and glass-shell refractive indices are $n_{\mathrm{c}} = 1.5$, $n_{\mathrm{s}} = 2.51 + i0.28$, respectively), which reveals a modulation in Q_{sca} while varying the core radius r_{c} between two limits: an all-glass particle ($r_{\mathrm{c}} = 0$) and an all-polymer particle ($r_{\mathrm{c}} = a$); Figure 14(a). Thus, by adjusting an internal *geometric* degree of freedom, Q_{sca} may be varied below or above that of equi-sized uni-material particles made of either of the constitutive materials, as a result of multipolar interferences ($ka = \frac{2\pi}{\lambda} a \approx 6$).

We confirm these theoretical predictions by examining specifically designed and manufactured particles having three different core-shell ratios, structures A ($r_c = 0$ nm), B ($r_c = 325$ nm), C ($r_c = 400$ nm) highlighted in Figure 14(a) and selected to confirm experimentally that varying r_c can reduce *or* enhance Q_{sca}. Critically, to isolate the effect of the internal particle structure on Q_{sca} and eliminate the impact of particle-particle interactions, we carry out the measurements on one single particle. The formidable

challenge of identifying the extremely weak scattered signal off a single particle from the strong background of incident light is addressed by constructing a dark-field light-scattering setup in which the particle is excited by an evanescent optical field at a wavelength of 532 nm. For this purpose, the particles are deposited on a cover slip that is placed on the prism. The intensity distributions were measured across a 10×10 μm^2 plane situated at a height ≈ 2 μm above the particle. For this purpose, we used a Nanonics MultiView 4000 tuning-fork near-field scanning optical microscope (NSOM) working in standard collection mode. In tapping mode, we determined the plane of the particle, then retracted the tuning fork 2 μm above that plane. In the experiment, the test particles were placed on the surface of a prism of refractive index $n = 1.5$ and illuminated in total internal reflection by 532-nm-wavelength continuous wave laser beam (100 mW power) slightly focused via a 4× microscope objective, Figure 14(b). Scattered light is collected using a Cr-Au coated tapered silica fiber probe (Nanonics) with 50-nm-diameter aperture connected to a photon multiplying tube (PMT; Hamamatsu, H7421). The same neutral density filter was used with all the samples to avoid saturation of the PMT and guarantee that the measurements of the scattered profiles are all on the same intensity scale.

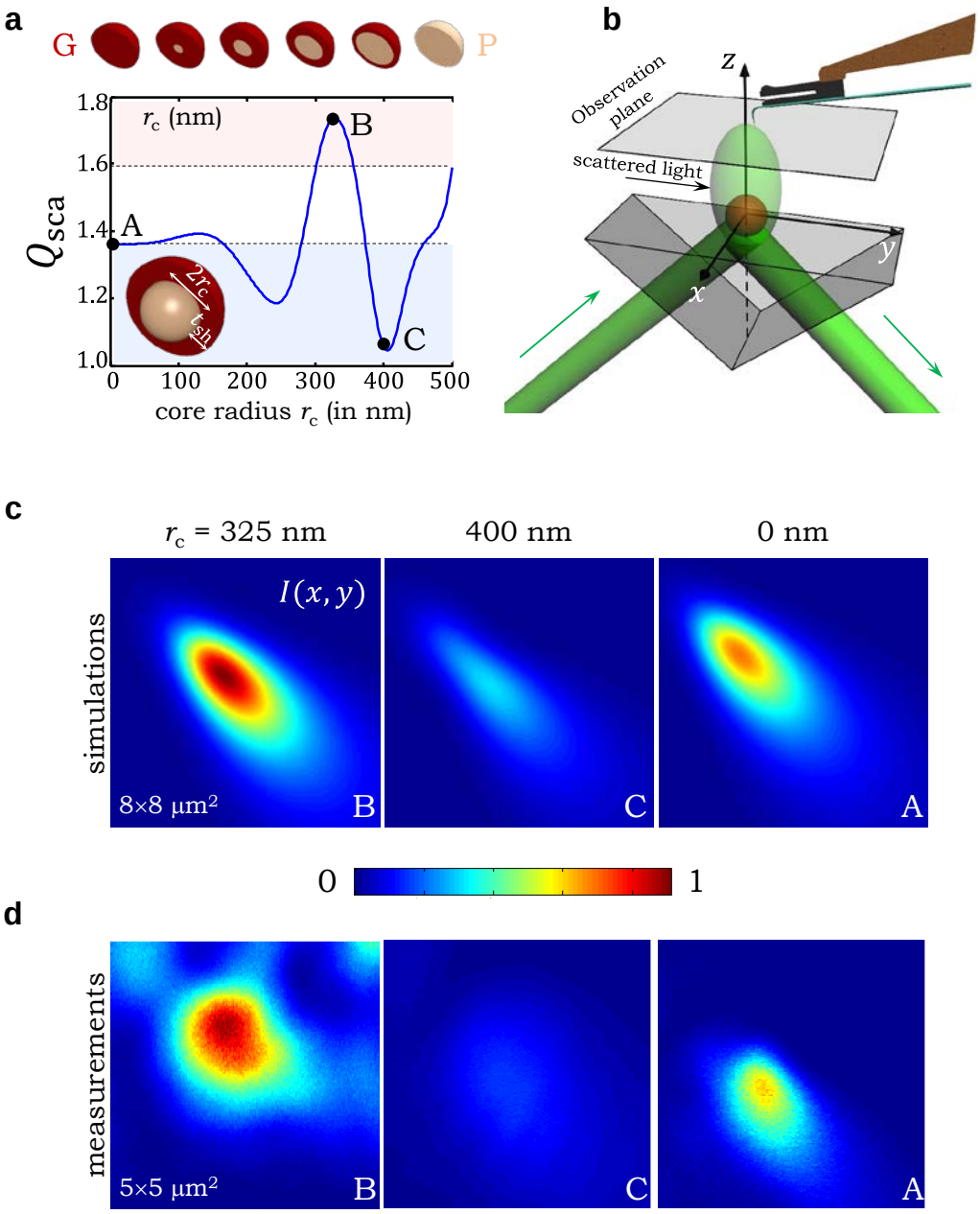

Figure 14: Tailoring the scattering cross section in high refractive-index-contrast core-shell photonic particles.(a) Calculated Q_{sca} for a core-shell particle of fixed outer radius 500 nm, core is the (polymer-P) PES having radius r_c while the shell is the (glass-G) As_2S_3 (refractive indices given in text). (b) Schematic of the optical system for dark-field near-field optical scanning microscope (NSOM), which is based on a Nanonics MultiView 4000 NSOM working in standard collection mode. (c) Calculated scattered field intensities from three particle structures corresponding to cases A, B, and C in (a). (d), Measured intensity distributions corresponding to those in (c).

Measurements of the scattering phase functions for structures A, B, and C are plotted in Figure 14(d). The measurements presented in Figure 14(d) are 'absolute' in the sense that the same intensity scale is employed for the three particles. While symmetry in standard Mie scattering based on propagating plane-wave-excitation excludes any cross-polarization terms in the scattering matrix, the exponentially decreasing amplitude in the evanescent-wave-scattering arrangement introduces an asymmetry that leads to cross-polarization terms. Consequently, the scattered intensity depends on the specific polarization and direction of the incident beam. The results shown in Figure 14(d) correspond to *p*-polarized incidence.

To model this evanescent excitation scenario, the usual Mie theory [28] – describing scattering of a propagating electromagnetic plane wave from spherical particles – falls short. While previous modeling attempts either generalize Mie theory or rely on purely computational techniques [52,53], we make use instead of a recent theoretical advance in which the conventional Mie theory is directly applied to scattering of evanescent waves through a complex-angle rotation of the standard Mie solution [16,54]. By rotating both the direction and the distribution of the incident electric $\vec{E}(\vec{r}) = \hat{R}_y(-\gamma)\vec{E}\,[\hat{R}_y(\gamma)\vec{r}]$ and magnetic $\vec{H}(\vec{r}) = \hat{R}_y(-\gamma)\vec{H}\,[\hat{R}_y(\gamma)\vec{r}]$ fields by a complex angle γ, a z-propagating plane wave can be transformed into an evanescent field [54]; here $\vec{E}$, $\vec{H}$, and $\vec{r}$ are electric field, magnetic field, and position vectors, respectively, and $\hat{R}_y(\gamma)$ is a vector-rotation operator around the y-axis by an angle γ. This transformation was applied to the solution of conventional Mie theory to obtain the evanescent wave scattering from a spherical particle. In the conventional Mie theory, γ defines the orientation of the

incident plane wave which is a real quantity; in contrast, γ is a complex angle in the method we employed. In our simulations we adapted a standard Mie scattering code written in MATLAB and included the aforementioned transformation in which the complex angle γ was obtained as the refraction angle of a plane wave incident on the hypothetical interface between the high-index and low-index media. By exploiting this complex-angle-rotation methodology to calculate the field scattered by spherical core-shell particles excited by the evanescent-field-configuration in Figure 14(b), we predict the scattered intensity distribution $I(x, y)$ in a plane 2-μm above the particle (Figure 14(c)) which is in excellent agreement with the measurements Figure 14(d)).

3.4 Control over polarization in optical scattering

Structuring a spherical particle azimuthally – rather than radially – has traditionally been a more demanding fabrication task, and to date is limited to 'Janus' structures in polymers in which two materials are compartmentalized in two hemispheres or only the surface is treated [147–149]. While symmetry principles may potentially enable higher-order discrete rotational symmetry through directed template growth, arbitrary control over the azimuthal structure of a spherical particle displaying no symmetry is out of reach of current approaches. The in-fiber breakup strategy permits sophisticated yet *facile* and *systematic* azimuthal-symmetry engineering via core segmentation.

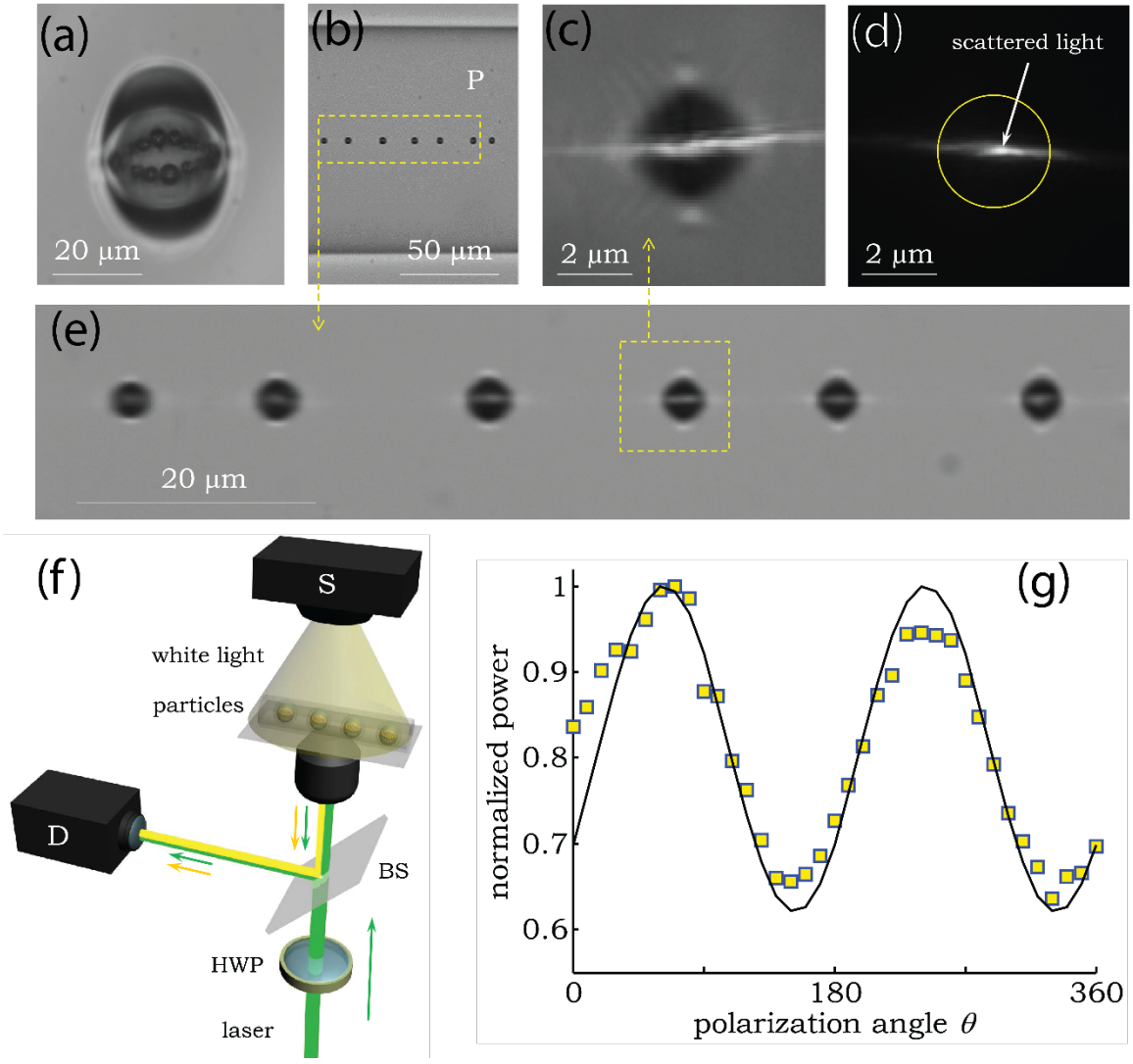

Figure 15: (a) Optical transmission micrograph through a micro-particle.(b) Transmission optical micrograph of a section of fiber containing a necklace of 3-µm-diameter particles with the same structure as in a.(e), Higher-magnification micrograph of a section of the fiber in (b). White light is used in imaging, while a green laser is imaged in reflection (the horizontal white line) and scatters strongly parallel to the axis along which the internal high-index nanoparticles are aligned. (c), A micrograph of a single particle from (e) with combined laser and white-light scattering. (d), Micrograph of laser light scattering from a single particle (white light turned off). The yellow circle is a guide to the eye and corresponds to the particle surface. (f), Schematic depiction of the optical arrangement for measuring the polarization-dependent scattering. The yellow beam indicates the transmitted white light used to align the sample, while the green one corresponds to the laser radiation used to measure the backscattering. HWP: half wave plate; BS: beam splitter; S: source; D: detector. (g), Sinusoidal modulation of the integrated scattered intensity (squares) as a function of incident polarization angle. The maximum occurs when light is polarized along the direction of the internal nanoparticle strings. Squares are the data and the solid line is a sinusoidal fit.

Moreover, radial and azimuthal structuring can be realized *simultaneously* in a single geometry. An example of combined radial and azimuthal structural control in a tri-material particle (two glasses and one polymer) is shown in Figure 15 in which four thin high-index glass threads are embedded in a low-index polymer surrounded by a high-index thin glass shell. The disparity between the diameters of the glass threads and the polymer results in the threads first breaking up into four parallel strings of smaller particles followed by breakup of the polymer into spherical particles containing the smaller glass particles.

Azimuthal structural engineering of a particle can enable controlling the polarization of electromagnetic waves. In particular, a spherical photonic particle with broken internal azimuthal symmetry of sufficiently high refractive-index-contrast exhibits polarization-dependent scattering. When a plane wave illuminates a spherical particle whose diameter is much smaller than the wavelength, there is no phase shift between the electric fields components polarized parallel and perpendicular to the scattering plane. We designed the internal structure of the particles such that the four lines of high-refractive-index small nanoparticles inside each particle break its azimuthal symmetry by scattering light in a similar fashion to finite cylinders. We demonstrate polarization-dependent scattering from these structured particles using the arrangement shown in Figure 15(f). For this purpose, we retain the particles in the fiber and do not dissolve the cladding. As such, the particles all have the same orientation with respect to the fiber axis. The sample is first illuminated with white light to identify and align the particle (Figure 15(b-e)), and then with a green linearly polarized laser (532-nm wavelength) focused at approximately mid-plane of the particle to determine the strength of the polarization-dependent scattering (the

horizontal bright lines through the particles in Figure 15(c,d)). Both images are recorded using an Eclipse Ti – Nikon microscope (cooled to -55 °C). With the white light turned off, we imaged the scattered green light across a single particle (Figure 15(d)) and evaluate the integrated scattered intensity as a function of incident polarization, which is rotated via a half-wave plate (HWP). We observe significantly stronger scattering when the incident polarization is aligned parallel to the internal lines of nanoparticles with respect to the orthogonal polarization (Figure 15(g))

3.5 Control over isotropy of scattered power

Aside from the wave-specific properties such as the scattering phase function or polarization, modifying the power flow around mesoscopic scattering systems is also of interest. In particular, creating circumstances for isotropic scattering is, unfortunately, limited to inefficient dipolar units as mentioned in section 3.2. As we will show here, structures can be created that distribute isotropically the scattered energy similar to a point-like dipole but many orders of magnitude more intensely. For this purpose, we will introduce here the use of heterogeneous composite microspheres composed of a polycycloolefin matrix integrated with a random distribution of TiO2 nanoparticles.

A novel methodology has been recently developed for the fabrication of structured and functionalized composite polymeric micro- and nano-spheres. This unique approach utilizes a thermally-induced fluid instability occurring at the interfaces within multimaterial fibers by which the internal structuring and composition of the fibers are imparted upon the generated spheres [136,142]. As we have seen in the preceding sections

of this Chapter, a variety of scattering properties can be controlled by tuning the internal three-dimensional structure of multimaterial micro- and nano-particles [111,150]. Such structured elements constitute the building blocks for adjusting collective interactions in multiple light scattering regimes, which are typical for most important applications of composite materials.

The scattering of coherent light from homogeneous dielectric microspheres is well-described by the Mie theory [28]. As shown earlier, the directionality of scattering from a spherical particle depends on the optical size and the intrinsic material properties. In a heterogeneous sphere on the other hand, the addition of nano-scale dielectric inclusions leads to a composite system that alters significantly the behavior of the scattered light. When the concentration of inclusions is very low, the structure is close to being optically homogeneous and the incident field undergoes a simple single-scattering pointed mainly in the forward direction while maintaining the input polarization [28,106][ref]. Likewise, when the concentration of inclusion approaches 100%, the structure is once again homogeneous and the scattered field behaves again in the conventional manner. However, at intermediate concentrations, the Mie theory alone does not adequately describe the behavior of the scattered light, and a more rigorous treatment is required.

When the inclusions generate strong multiple scattering within a spherical particle that is much larger than the transport mean free path, one can consider that the heterogeneous composite acts as a diffusive sphere. To estimate the power flow around such particle, one should solve the diffusion equation in spherical coordinates. For this purpose, we consider that a narrow collimated light beam is normally incident on the

surface of the sphere. We will assume that the diffuse photon fluence rate $\varphi(\vec{r}, s)$ satisfies the diffusion equation [60,73]

$$\frac{\partial}{\partial t}\varphi(\vec{r}, s) - D\nabla^2\varphi(\vec{r}, s) + \mu_a\varphi(\vec{r}, s) = S(\vec{r}, s), \quad (12)$$

where c is the speed of light and D is the diffusion constant $D = (3(\mu_a + (1-g)\mu_s))^{-1}$, μ_a is the linear absorption coefficient, μ_s is the linear scattering coefficient, g is the mean cosine of the scattering angle, and $S(\vec{r}, s)$ denotes the source of photons. For a short pulse from an isotropic point source, $S(\vec{r}, s) = \delta(0,0)$ it may be shown, that in an infinite medium the solution of Eq. (1) is $\varphi(\vec{r}, s) = c(4\pi Ds)^{-3/2} \exp\left(-\frac{r^2}{4Ds} - \mu_a s\right)$ [60,73]. One can use this result to solve the problem in the spherical geometry by making two further assumptions. First, one can assume that all the incident photons are initially scattered at a depth $z_0 = [(1-g)\mu_s]^{-1}$ such that the source term becomes a simple δ-function as considered above. This localization of the first interactions will be sufficiently accurate if we are interested in the fluence rate far from the source. Second, one must also specify a boundary condition, which, for simplicity, can be taken as $\varphi(\vec{r}, s) = 0$ on the physical boundary $\vec{r} = a$ [73]. This boundary condition can be met by adding a negative or image source of photons to the infinite medium problem as shown in Figure 16. The fluence rate per incident photon can then be written as the sum of contributions from these two sources:

$$\varphi(r,\gamma,s) = c(4\pi Ds)^{-\frac{3}{2}}\exp(-\mu_a s)\left\{\exp\left[\frac{-(r^2+r'^2-2rr'\cos\gamma)}{4Ds}\right] - \exp\left[\frac{-\left(\frac{r'}{a}\right)^2(r^2+\frac{a^4}{r'^2}-\frac{2ra^2}{r'}\cos\gamma)}{4Ds}\right]\right\}. \quad (13)$$

We want to know the number of photons reaching the surface per unit area per unit time $\left|\vec{J}(a,\gamma,s)\right|$ which can be calculated from Fick's law $\vec{J}(a,\gamma,s) = -D\nabla\varphi(r,\gamma,s)|_{r=a}$ to become $\vec{J}(a,\gamma,s) = (4\pi D)^{-\frac{3}{2}}cs^{-\frac{5}{2}}\left[\frac{(r'^2-a^2)}{2a}\right]exp\left[\frac{-(a^2+r'^2-2ar'cos\gamma)}{4Ds}\right]$.

This leads eventually to the final expression for the reflectance $R(\gamma,s) = \left|\vec{J}(a,\gamma,s)\right|$

$$\int R(\rho,s)ds = A\left[\frac{e^{-B/s}}{B\sqrt{s}} - \frac{\sqrt{\pi}\,erfi\left(\frac{\sqrt{B}}{\sqrt{s}}\right)}{2bB^{3/2}}\right],$$

where, $A = (4\pi D)^{-\frac{3}{2}}\left[\frac{(r'^2-a^2)}{2a}\right]$ and $B = \frac{(a^2+r'^2-2ar'cos\gamma)}{4D}$.

The power flow at each point on the surface of the particle can be obtained by integrating over all possible paths in (Eq. 9). This power flow is plotted in Figure 16(b) as function of γ. As can be seen the diffusive sphere does not provide a spherically symmetric outgoing power flow. This is due to the fact that, irrespective of the transport mean free path and the size of the sphere, the reflection cannot be diffusive. In other words, a composite sphere that is essentially diffusive cannot provide an isotropic power flow unless is uniformly illuminated from all directions.

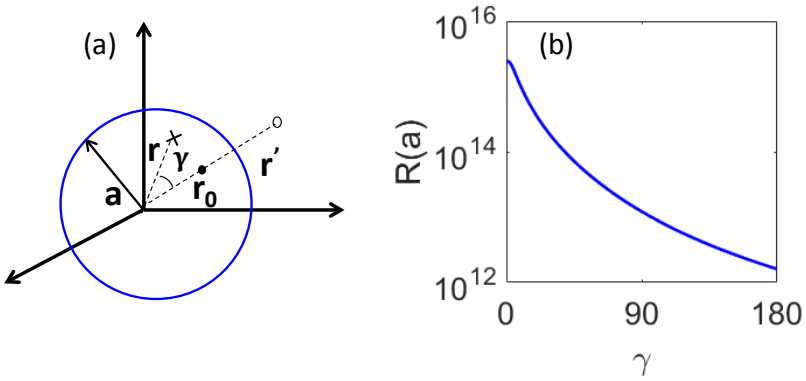

Figure 16: Reflectance

It appears that different strategy is necessary to obtain an isotropic power flow around a composite particle. Achieving the angular symmetry still requires significant multiple scattering inside the sphere but, in addition, one has to establish a certain balance between the scattering mean free path, which is controlled through the concentration of inclusions, and the overall size of the composite particle. Practically, one has to operate in sub-diffusing regimes and new methods are needed to evaluate how efficiently these heterogeneous composites can randomize the input light.

When a coherent optical field interacts with an optically inhomogeneous structure, most of its properties are affected in a statistical way. The emerging complex fields are characterized by statistical distributions of intensity, phase, and states of polarization. The spatial distribution of intensity (the so-called speckle patterns) and the distribution of polarization states are direct indicators of the regime of interaction between the incident optical field and the particular randomly inhomogeneous medium [151–153]. Multiple scattering determines a complicated interference pattern but, when the coherence length of the incident radiation exceeds the largest delays introduced by multiple scattering trajectories, the emerging speckle pattern is still fully polarized at each spatial location. Of

course, the state of polarization may vary from point to point and this variation has actually been used to describe the regime of optical interaction [154,155]. When single scattering dominates, the spatial variability of the polarization states is limited even though the speckle pattern is fully developed, i.e. the phase varies randomly according to a uniform distribution. On the other hand, when the direction of propagation is efficiently scrambled by the process of multiple scattering, the polarization states across the speckle pattern are efficiently randomized and the speckle field appears globally as unpolarized [156,157].

Models have been constructed to relate the degree of linear polarization P to the evolution of multiple scattering in random media. For instance, the intensity contribution in polarization channel parallel, $I^{\parallel}$, and perpendicular, $I^{\perp}$, to the direction of incident polarization can be expressed in terms of the probability density of scattering events $I(n)$ predicted by a scalar diffusion approach as $I^{\parallel,\perp}(n) = I(n)f^{\parallel,\perp}(n)$, where the polarization factors are estimated from the Bethe–Salpeter equation as $f^{\parallel}(n) = \frac{1}{3}\left[\left(\frac{10}{15}\right)^{n-1} + 2\left(\frac{7}{15}\right)^{n-1}\right]$ and $f^{\perp}(n) = \frac{1}{3}\left[\left(\frac{10}{15}\right)^{n-1} - \left(\frac{7}{15}\right)^{n-1}\right]$, respectively [10]. This analytical description can be used to estimate the evolution of the degree of polarization from single scattering (n=1) to any regime of stronger scattering. This description, however, is limited to dipolar scattering. Nevertheless, efforts were also directed towards describing the evolution of polarization properties in realistic particulate systems with various optical densities. The characteristic depolarization lengths in a medium composed of uncorrelated spherical particles were shown to depend on both the geometry and the effective size parameter of the scatterers [151,158–161].

For specific conditions of incident polarization and coherence properties, an experiment that measures the global degree of polarization of a stationary speckle field can be used to determine the scattering regime of interaction. A globally unpolarized field is a strong evidence for heavy multiple scattering. A series of experiments was conducted on composite spherical particles fabricated from a thermoplastic cyclic olefin polymer (COP: Zeonor® 1420R, $n \cong 1.5$) as the matrix material due to its low optical absorption and solvent resistance and the nanoparticle titanium dioxide (R-706 TiO2, DuPont®), selected for their performance as white pigments -their linear dimension is $d \approx 300$ nm with the refractive index $n \cong 2.67$– and are thus optimal for broadband visible scattering.

In the experiments, we illuminate the particle with polarized monochromatic laser beam in three different configurations as illustrated in Figure 17. A $\lambda = 532$ nm (Nd:YAG) linearly polarized laser beam is split into a transmission and reflection arm to illuminate the composite micro-sphere which is placed onto a glass coverslip. In reflection configuration the laser beam passes through a spatial filter and focused down to the sphere mid-plane (Figure 17(a)). The beam was focused using a long-working-distance LD EC Epiplan Neofluar 100× reflected-light dark-field objective lens. The back-scattered field was imaged using the same objective lens and recorded. The dark-field configuration is similar with a reflection despite the fact that the expended laser beam passes through a dark-field filter (patch stop) as shown in Figure 17(b). For the measurement of the transmitted scattered field, we block the reflection arm and the beam focused through a 50× long working distance Nikon objective lens. The field was then imaged and recorded using the distance LD EC Epiplan Neofluar 100× objective plane (Figure 17(c)).

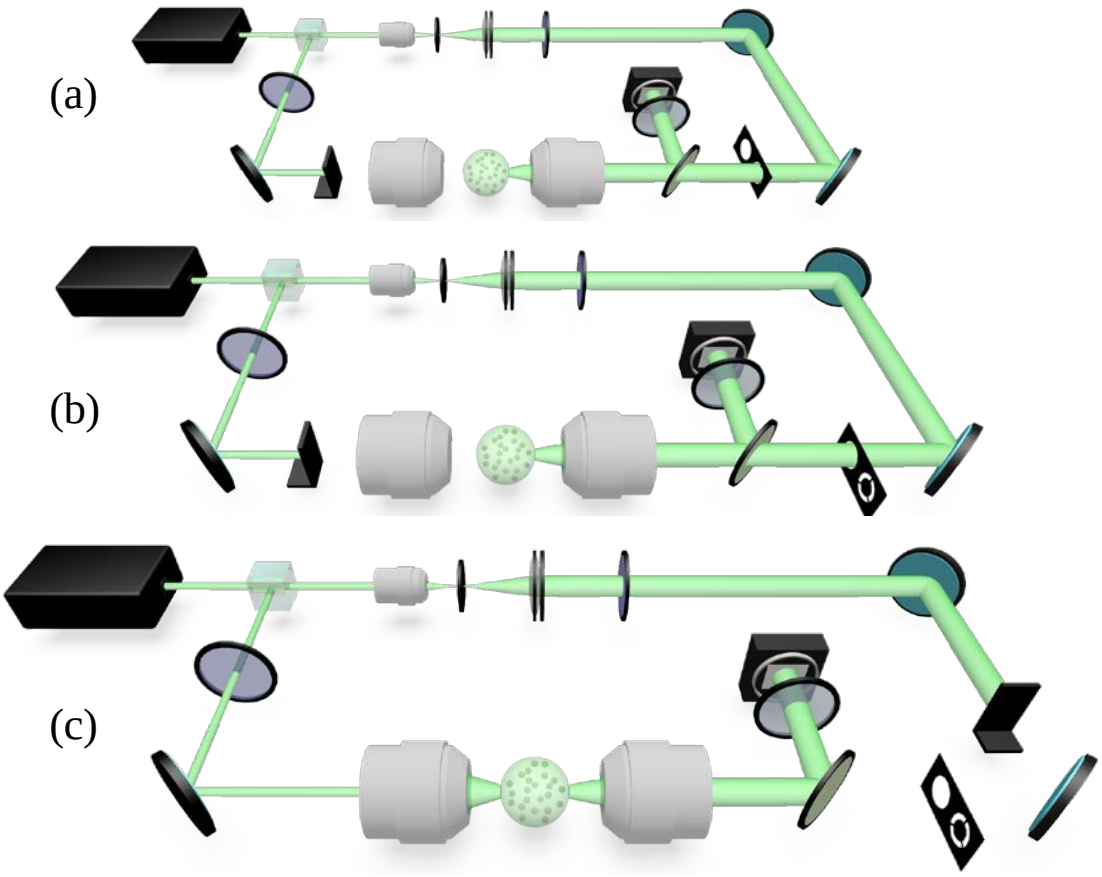

Figure 17: Schematic of experimental set up, a) reflection , b) dark-field, and c) transmission configurations

In all measurements, an analyzer was used to determine the degree of linear polarization. Moreover, using an imaging geometry in all configuration we ensured that no additional wave mixing occurred; that is, the field was recorded at the sphere mid-plane. The degree of linear polarization measured for the backscattered field was determined to be 0.251, while for the transmitted field it was found to be 0.012 and for the dark-field 0.060.

From the observed speckle patterns and the measured degree of linear polarization it can be concluded that the fields in both forward and backward directions were diffusively scattered. The spatially random variations of the amplitude and phase of the field confirm that multiple scattering events occur uniformly throughout the volume of the composite particle. Based on the uniform distribution of these fluctuations it can be further concluded that the inclusions are both well-distributed and well-dispersed throughout the composite microsphere volume. This observed behavior is very different from that of Mie scattering from a homogenous microsphere as can be seen in Figure 18(c) for the case of a 10 μm polystyrene particle for which the DOP values measured in the same conditions are 0.99, 0.99, and 0.43, respectively.

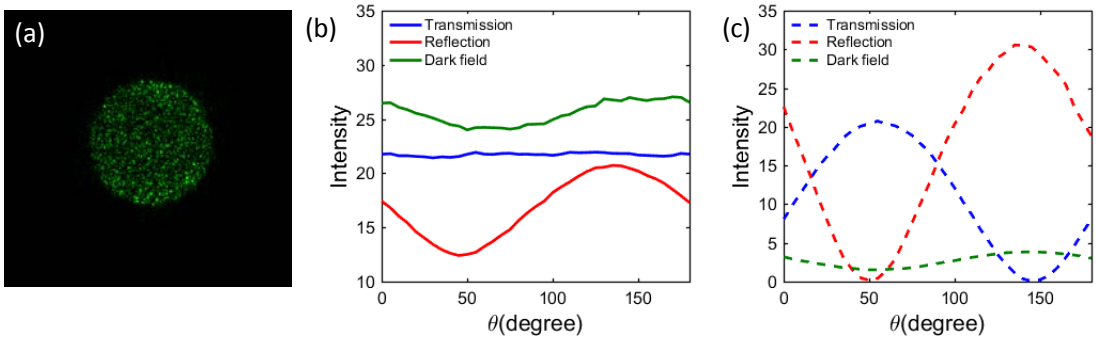

Figure 18: (a) Micrograph of the composite microsphere in the dark-field configuration, Integrated scattered intensity as a function of the orientation of polarization analyzer (b) 60 μm composite microsphere and (c) 10 μm polystyrene particle.

In a separate experiment, we have also evaluated the integrated scattered intensity for both transmission and reflection configuration. The ratio between the transmitted and reflected powers, normalized with respect to the input power, are illustrated in Figure 19(b). It is readily observed that by changing the size of the composite microsphere we are

able to control the ratio between the power flow in forward and backward directions. We conclude that such composite microsphere could create centers of omni-directionally diffuse light within a larger scale medium, thus increasing the overall scattering efficiency. We note that, due to their inherent forward scattering, homogenous scattering centers cannot create similar situations within a scattering medium. For example, the ration between forward and backward scattering is 17.5 for a 10 μm polystyrene particle, more than one order of magnitude higher than in the case of the composite sphere discussed here.

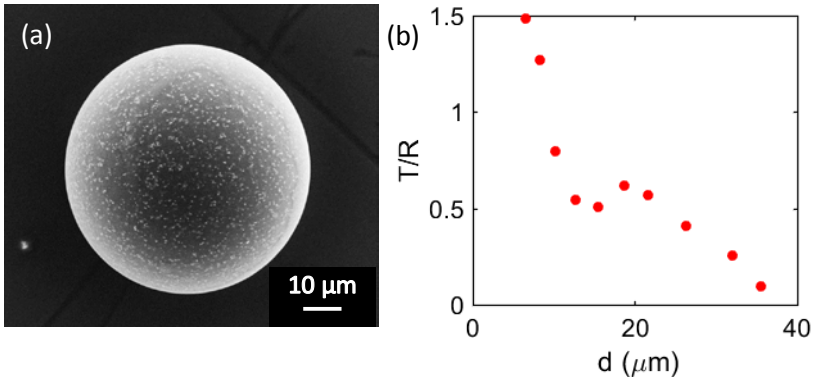

Figure 19: (a) SEM micrograph of a composite microsphere. (b)Ratio of the normalized transmitted to the reflected power as a function of the overall diameter of composite spheres.

3.6 Summary

In this chapter, we examined how the internal structural of scattering centers affects the outcome of light-matter interaction. We have shown that the design of the internal structural of a single scatterer can be used to control the characteristics of the scattered light. We have demonstrated that the simple structural modifications in all-dielectric materials provide means to achieve extreme optical properties without having to appeal to exotic materials or complicated manufacturing procedures. More specifically, we have

demonstrated that designing multi-material dielectric particles with controlled radial and azimuthal structure allows adjusting the extinction cross section, control the scattering directivity, and control the polarization-dependent scattering. Such structures can be obtained using thermally induced fluid instability in extended composite fibers. In this approach, controlling the internal three-dimensional geometry of a multi-material photonic particle enables the precise allocation of the desired materials. We demonstrated that dielectric core-shell structures with similar macroscopic sizes can have both high scattering cross sections and radically different scattering phase functions. In addition, a specific structural design can be implemented to break the azimuthal symmetry of the spherical particle and, therefore, control the polarization-dependent scattering of electromagnetic waves. We also shown that small inclusions with high refractive index can be manipulated within larger size composites to effectively create the desired structural asymmetries. We have also demonstrated that a heterogeneous composite microsphere containing a polymer matrix integrated with a random distribution of nanoparticles can distribute uniformly the scattered power. Practically, from a scattering power standpoint, such entity has a dipolar behavior. However, its scattering efficiency is many orders of magnitude higher than that of a point dipole.

Further work can involve modifying individual scatterers to manipulate other properties of light. For example, particles can be designed to affect preferentially specific wavelengths without dissipating the energy. A further step in this design process is to solve the associated inverse Mie scattering problem for a core-shell spherical particle. Achieving this task will provide a considerable flexibility in manipulating the properties of the

scattered light. One can envision that, starting from a desired far-field or near-field optical scattering phase function for a single particle, a complex inverse problem could to solved to describe the necessary particle structure, i.e. its internal 3D refractive-index distribution. This complex design could of course involve both the real and imaginary parts of the refractive index. Nevertheless, such inverse optical problem has not yet been solved in its entirety.

CHAPTER 4:
OPTICAL SENSING AT MESOSCALES: LIGHT-MATTER INTERACTIONS FOR CHARACTERIZING COMPLEX MEDIA

4.1. Introduction

Mesoscale optics defines a framework for understanding phenomena occurring in multitude material systems such as biological tissues, optical coatings, colloidal and polymer fluids, 2D materials, fabricated nanostructures, etc. The focus of this chapter is quantifying and controlling the statistical properties of the radiation emerging from complex media and using these measurable properties for surface and subsurface diagnostics. In this chapter we demonstrate and develop a number of optical techniques that link the scattered light to material information. For this, one needs to understand the nature of the light-matter interaction in random media.

Under illumination by coherent light, the waves transmitted through random media consist of contributions from many independent and multiple scattering. Propagation of this light to a distant observation point results in the addition of these various scattered components with relative delays, which may vary from several to many wavelengths. The interference of these de-phased but coherent wavelets results in the granular pattern which know as *speckle pattern*. This extremely complex pattern bears no obvious relationship to the properties of the illuminated object. Rather, it appears chaotic and unordered, and it is best described quantitatively by the methods of probability and statistics. The entire speckle pattern changes if the interaction changes due to, for instance, changes in the medium's configuration. Characterizing the intensity fluctuations within a speckle pattern may require an ensemble of such realizations of wave-matter interactions. In the other words,

one could consider that the random medium is an ensemble of realizations of disorder. Each particular realization of disorder determines its own specific pattern of fluctuations in the emerging waves. Traditionally, multiple light scattering is considered to wash out all structural information and, as a result, inhomogeneous media are sometimes expected to behave as perfect Lambertian diffusers. Contrary to this conventional wisdom, however, the field properties in close proximity to inhomogeneous media are influenced by the detailed structural characteristics.

According to the central limit theorem (CLT), under rather general conditions, the statistics of the sum of a large number of independent random variables is asymptotically Gaussian. Therefore, if a large number of independent waves interfere at each observation point while having ae uniform phase distribution, one could consider that the real and imaginary parts of the complex scattered field obey Gaussian statistics. It follows that the amplitude of the field has a Rayleigh distribution and the corresponding intensity is decay exponentially. However, there are many situations that can infringe on CLT, such as finite illumination size, localization effect, insufficient averaging, correlation between scatterers, existence of high-order correlations and etc.

In this chapter we first demonstrate that the spatial correlation between scatterers, results in a non-Gaussian statistic of the waves in the close proximity of the interface of a random medium. Moreover, we will show that the near-field statistics renders details of both the structural morphology and the distribution of large field enhancements. This is critical for understanding the role of disorder in enhancing the interaction between light

and matter. Then, we will demonstrate that the near-field coherence properties can also be an extremely effective tool for characterizing interfaces.

Based on the conventional coherence theory, the fields radiated by statistically homogeneous sources correlate over spatial regions of the order of the wavelength irrespective of the distance from the surface of the source and the detailed characteristics of the source of radiation. However, in practice sources have finite extends and their particular structure cannot always be neglected. For a finite source, the correlation domain is larger and depends on the propagation distance, a property that is framed in the famous Van Cittert-Zernike theorem. However, the situation is different in the proximity of the source where the influence of evanescent components can be dominant. In these conditions the coherence properties are non-universal. because the presence of inhomogeneous waves can affect the overall statistical properties of optical fields. It has been shown that the spatial coherence length of the field close to the surface of a random media depend on the distance from the interface and, moreover, their extent can be significantly smaller than the wavelength and it is related to the coherence properties at the interface.

In this chapter, we will demonstrate that the coherence properties can be related to the structural morphology of the medium emitting the radiation and, therefore, can act as distinctive characterization tools. Specifically, we will show that the spatial extent of the near-field correlations is a direct indicator of defect density in two-dimensional atomic lattices [26,162–164].

Finally, in this chapter we will also demonstrate experimentally that spurious effects caused by interference can be eliminated in passive nearfield imaging by

implementing a simple random illumination. We will show that typical imaging artifacts are effectively eliminated when the radiation emitted by a pseudo-thermal source illuminates the sample and the scattered field is collected by an aperture probe over essentially all angles of incidence. This novel pseudothermal source can be easily implemented and it enhances significantly the performance of passive nearfield imaging.

4.2. Disorder Fingerprint: Intensity Distributions in the Near-Field of Random Media

Waves propagation through disordered media determines strong variations of their intensity. The dominant contribution to these fluctuations, the common speckle pattern, is governed by the Rayleigh law of universal Gaussian statistics [9]. However, when waves interact with a small number of scattering centers or with a finite volume of inhomogeneous media, the scattered field does not reach this universal behavior [165–168]. In such cases where the complete randomization of phases of scattering waves does not occur, the emerging scattered field is described as a non-Gaussian process.

Interestingly, non-Gaussian statistics can be also caused by the strong disorder generating additional correlations between scattering paths. In particular, it was suggested that the deviation from Gaussianity can be quantified by a single scaling parameter, the crossing probability between any two Feynman trajectories [169]. The corresponding intensities do not follow the Rayleigh statistics anymore, as observed in the microwave domain [170].

The appearance of stretched exponential intensity distributions was discussed by several authors [169,171,172].

Conditions for non-Rayleigh statistics can also be imposed by specially prepared phase masks [173], by random structures supporting highly localized modes [174], by disorder systems characterized by crossing Feynman paths [175], or can be a consequence of localized field enhancements in resonant metal-dielectric structurs [176].

Statistical properties of the electromagnetic fields interacting with complex media is a subject of broad interest. These properties are usually discussed in terms of general (universal) characteristics, which are of limited use for both material characterization and for designing specific outcomes of light-matter interaction. In this chapter we demonstrate that subtle structural details can be revealed by the distribution of near-field scattered intensities.

Through systematic numerical calculations and experiments we will show that, in spite of the massive overall randomness of scattering media, the short-range correlations of disorder determine specific, non-universal non-Rayleigh statistics, which can be practically measured. We will demonstrate that long-tail distributions of intensity evolve in the near-field of effectively semi-infinite disordered media even for non-absorbing, purely dielectric materials.

In realistic media, the unavoidable short-range correlations of disorder and near-field interactions (NFI) require a rather microscopic description of the electromagnetic field distribution [177,178]. The consequences of NFI should be even more significant for systems with finite-size disorder where the field description involves multipolar interactions. In these circumstances, the structural morphology determines the level of NFI and, consequently, new regimes of macroscopic transport are established [22].

Due to evident non-stationarity, relating the fluctuations of the electromagnetic field to the structural characteristics of disorder requires a multi-scale analysis. To pursue this numerically, we first generated different types of disordered media containing rigid spheres with 11% volume fraction. We study structures generated by (i) randomly packing hard spheres, (ii) by implementing a typical adhesive spheres packing [179] with a stickiness parameter $\tau = 0.11$, and (iii) by creating a clustered structure by agglomerating about 70 particles around randomly chosen clustering centers. Typical three-dimensional structures generated by these three methods are illustrated in Figure 20(a-c). An appropriate way to characterize the randomness of disordered structures is to evaluate the corresponding spectrum of the configuration entropy (CE) [180]

$$H^*(l) = -\frac{\sum_{k=0}^{N_{max}} p_k(l) \log p_k(l)}{\log(N_{max}+1)}, \qquad (14)$$

which involves analyzing the structure through an sliding block with dimensions $l \times l \times l$. In the CE definition, $p_k(l)$ are the probabilities for the sliding block to contain k particles and N_{max} is the maximum number of spheres that can be fitted into a sliding block. The CE spectra calculated for the three three-dimensional structures are shown in Figure 20(d-f) and clearly reveal the different morphologies. Notably, in all cases, the CE reaches a maximum for a certain size of the analysis block. This specific scale, the entropy optimum length l_H (EOL), is a measure of the spatial inhomogeneity and indicates the scale length at which a particular structure is most disordered [180]. In our examples, the EOL values corresponding to random packing of hard spheres and adhesive particles are rather similar with $l_H = 2.6$ and $l_H = 3.4$ sphere diameters, respectively, reflecting the fairly similar type of disorder. The spatial variability in the more lacunar clustered structure on the other hand is characterized by a significantly larger EOL of 5.2 sphere diameters. It has been shown that the EOL magnitude relates to the characteristic dimensions of particles or pores in the structure [181]. Thus, the larger porosity seen in Figure 20(c) explains the greater EOL evaluated for the clustered structure (iii). Again, all these structural differences correspond to media containing the same overall volume fraction of spheres.

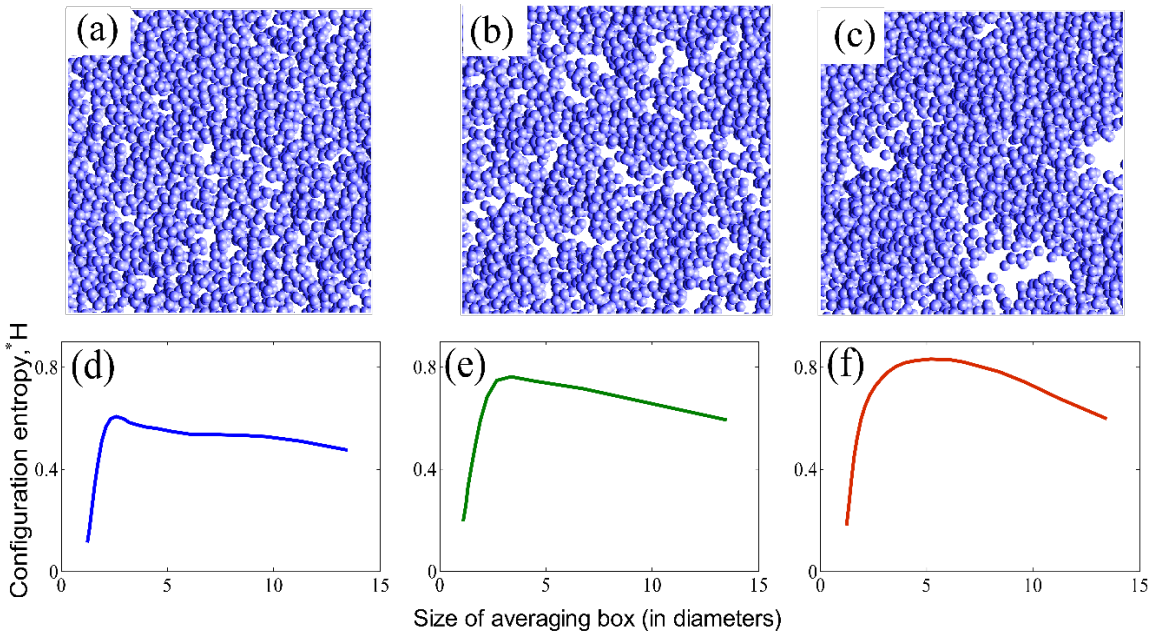

Figure 20: Top view of the randomly packed 3D structures of (a) hard spheres, (b) adhesive spheres, and (c) clustering distribution of spheres. The volume fraction of spheres is 11% in all cases. (d)–(f) Corresponding configurational entropy spectra

At the second stage, we calculate the electromagnetic field distribution in the vicinity of these disordered samples using the multiple sphere T-matrix code (MSTM version 3.0) [20]. Typical results are illustrated in Figure 21 and correspond to 250nm diameters spheres of TiO_2 with refractive index 2.67 that are packed into cylindrical slabs of thickness 3.5μm and a diameter of 14μm. Each slab contains 6586 particles. Even for calculations performed on a cluster of parallel computers, the number of simulated particles is limited to several thousands and, to increase the overall scattering, we consider that particles are placed in air. In all cases, the thickness of the slab is larger than ten times the transport mean free path and the strong multiple light scattering

randomizes effectively the electromagnetic field. The slab is illuminated with a Gaussian beam with the wavelength 532nm which propagates along the axis of the cylinder. The small waist of the beam of 1.5μm allowed minimizing boundary effects. The MSTM calculations provided all six electric $\mathbf{E}(\mathbf{r})$ and magnetic $\mathbf{H}(\mathbf{r})$ complex field components. This approach provides a complete and realistic description of the electromagnetic field distribution as it accounts for all possible light matter interaction within the slab.

The distribution of electromagnetic field in the close vicinity of the surface is usually measured with near-field scanning optical microscope (NSOM) probe that couples, with specific succeptibilities, different electric and magnetic fields components depending on their geometry and material properties [182–186]. In the case of aperture NSOMs, the measured signal is usually proportional to the electric field density [187–189]. However, in near-field literature the term "near-field intensity" is often used to describe this signal. For brevity, in the following we will also use the term intensity, which, in the case of near-field measurements, would not necessarily mean Poynting vector. Maps of such measured signals can be used to derive both the distribution of intensities [167] and the two-point statistics of the near fields [186,187].

Typical distributions of electric energy density $u(\mathbf{r}, \omega_0) = \varepsilon_0 \langle \mathbf{E}(\boldsymbol{r}, \omega_0) \cdot \mathbf{E}^*(\boldsymbol{r}, \omega_0) \rangle$ across a plane situated in the near-field at 50nm above the slab are

shown in Figure 21(a-c) for the specific cases of the three types of disorder examined in Figure 20.

It should be noted that the complex field in the proximity of the interface represents the overlap of three field components. If these field distributions would be uncorrelated, their overlap would lead to a Gamma distribution of intensities [12]. A reference curve corresponding to this distribution, $p_s(I_s) = \frac{N^N I_S^{N-1}}{\Gamma(N)\bar{I}^N} \exp\left(-N\frac{I_s}{\bar{I}}\right)$, with N=3, $\bar{I}$ the mean intensity , and I_s being the intensity and $\bar{I}$ its mean value, is included in Figure 21(a-c).

As can be seen in Figure 21, localized intensity hot spots emerge when disorder increases. To estimate the distribution of near-field intensities, the entire procedure was repeated for ten different realizations of disorder. The results are summarized in Figure 21(a-c) where the role of structural morphology is readily observed in the tails of intensity distributions. The distributions for hard spheres and adhesive particles are fairly similar while the tail in the distribution for clustered structure is more extended. This situation reflects the structural differences already seen in Figure 20.

A quantitative measure of these dissimilarities is given by the normalized variance $\mathrm{Var}[u(\mathbf{r},\omega)]/\langle u(\boldsymbol{r},\omega)\rangle^2$. The corresponding values for the random packing, adhesive spheres, and clustered structure are 0.3, 0.32, and 0.52, respectively. For comparison, the normalized variance of the Gamma-distribution plotted in Figure 21 is 0.5. The magnitude of normalized variance

smaller than 0.5 in Figure 21(a, b) can be explained by the fact that near-field field is essentially a three-dimensional field. As the disorder extends over larger scales, the near-field intensity distributions become more and more asymmetric (larger values of their high-order moments). The enhanced level of intensity fluctuations is a signature of the higher variability in the local dielectric environment in media with extended scales of disorder. These additional effects increase the value of normalized variance in Figure 21(c) above 0.5. This indicates that even small changes in EOL are reflected in the variance of near-field intensity distribution, in contrast to macroscopic examinations.

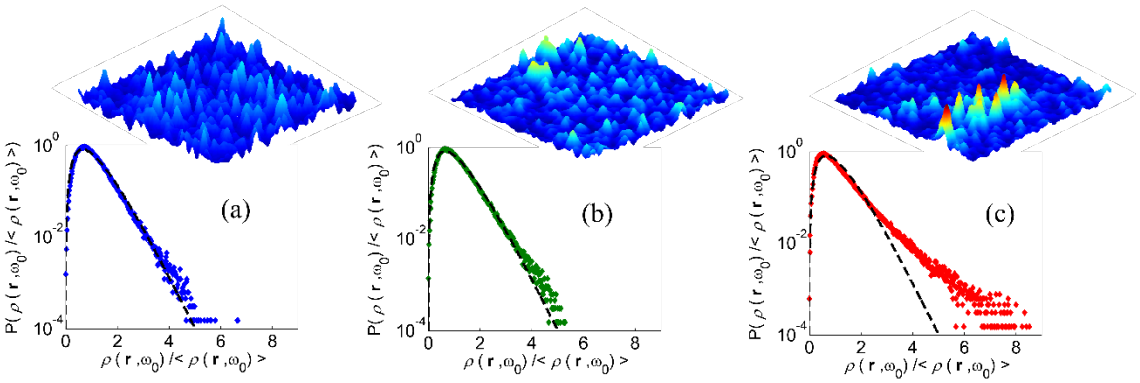

Figure 21: a), b) and c) Typical near-field intensity distributions and intensity probability density functions evaluated over 8x8 μm^2 areas at 50 nm above cylindrical slabs with 7μm radius and 3.5 μm thickness containing 11% volume fractions of 250 nm in diameter TiO_2 particles in air. The slabs have different types of structural disorder as shown in Figure 20. The intensity probability density functions are evaluated from 10 different realizations of disorder. The dashed line denotes the Gamma probability distribution corresponding to the superposition of three uncorrelated speckle patterns

We have also examined experimentally the near-field intensity fluctuations in media with controlled disorder. We designed a unique set of random media to create conditions similar to the situation depicted in simulations. Using 250nm in diameter TiO_2 particles embedded in a polymer matrix, we constructed composite media that macroscopically have ~10% volume fractions of scatterers. As clearly seen in the SEM micrograps shown in Figure 22(a,b), the media considered here differ only by the type of disorder, one having the TiO_2 particles homogeneously dispersed and the other manifesting an evident non-uniform clustering that makes these samples comparable to the cases (i) and (iii) in numerical simulations. This structuring was achieved by carefully mixing alumina surface treated TiO_2 submicron particles into stable emulsions of polymer microparticles with different sizes. The EOL values calculated from the 2D micrographs are 1.3 and 2.5 particle diameters for the case of uniformly dispersed (Figure 22(a)) and clustered TiO_2 particles, respectively (Figure 22(b)).

The TiO_2 particles embedded in the polymer matrix formed compact layers with a thickness of several tens of microns. The samples were illuminated with 532nm laser radiation through the exit port of an integrating sphere that created an effective randomization of the incident electromagnetic radiation.

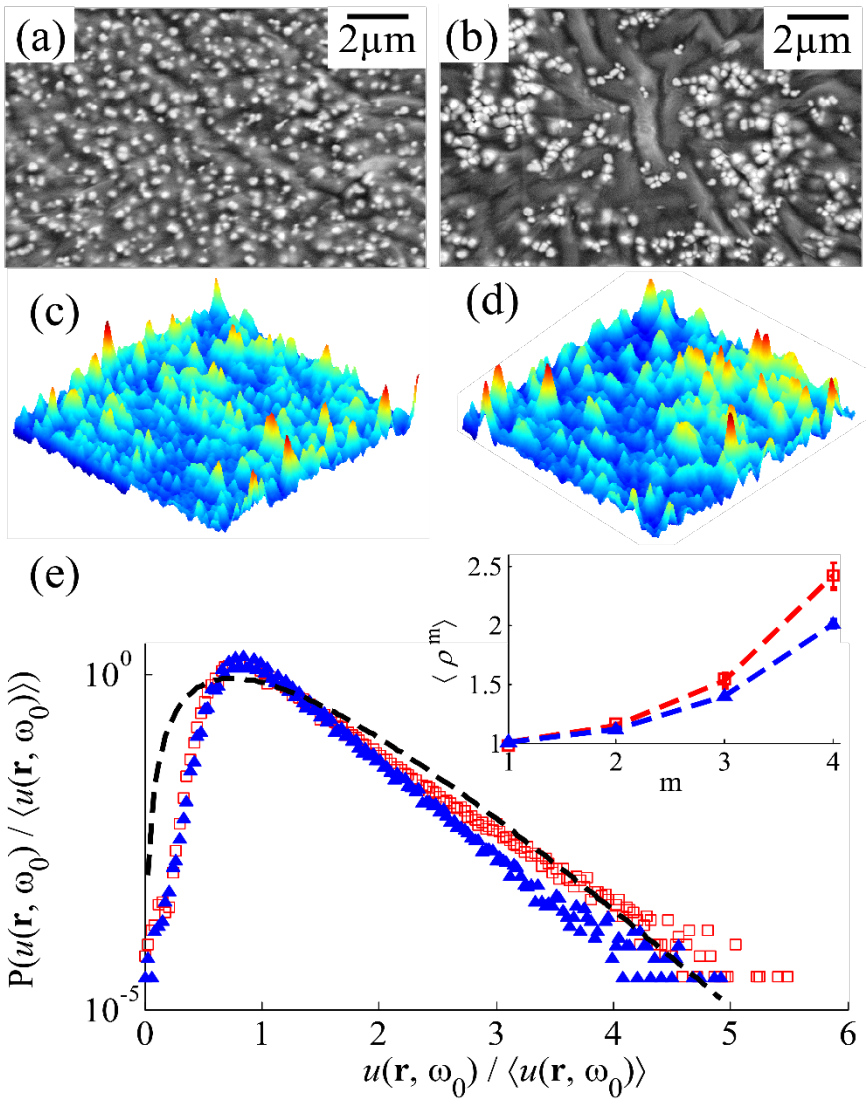

Figure 22: Scanning electron micrographs of locally uniform (a) and locally non-uniform (b) distributions of nanometer size TiO_2 particles embedded in a polymer matrix. c) and d) Corresponding NSOM scans collected over 10x10 μm^2 areas in intermittent contact mode. e) Intensity probability density functions evaluated from scans over 10 different regions of the sample (a) (blue triangles) and sample (b) (red squares). Each intensity ensemble contains more than 10^6 values. The dashed line denotes the Gamma probability distribution corresponding to the superposition of three uncorrelated speckle patterns. The inset shows the values of the first four moments of measured intensity distributions. The error bars in the insert indicate the uncertainty in evaluating the moments with 0.9 confidence.

The measurements were performed with a Nanonics MultiView 4000 tuning fork NSOM working in standard collection mode. Near-field intensity

distributions were collected across a 10x10 μm^2 plane using a Cr-Au coated pulled silica fiber probe with 100 nm aperture diameter and operating in intermittent contact mode with a probe oscillation amplitude of several tens of nanometers. Measurements were performed over ten different regions to ensure an appropriate ensemble average. More than 10^6 values of the measured intensities, corrected for the background noise, were used to generate the probability distributions corresponding to each sample. Even though near-field measurements are to some extent non-local, the small size of the probe clearly permits resolving the fluctuations of the electromagnetic field. As can be seen in Figure 22(c,d), the measurements provide high-resolution maps of near-field intensity values over extended dynamic ranges. This allows identifing the asymmetric tails specific to non-Gaussian distributions.

In weakly disordered systems, the underlying near-fields are Gaussian distributed because of a limited number of possible structural configurations. This result was obtained in one of our previous work [167]. However, when disorder increases as in the case illustrated in Figure 22, optical modes are sporadically confined to smaller volumes and, consequently, the intensity distributions aquire longer tails indicating strong variations in the level of disorder of the local environment.

The calculated normalized variance $\mathrm{Var}[u(\mathrm{r},\omega)]/\langle u(\mathrm{r},\omega)\rangle^2$ for the uniform and non-uniform distributions shown in Figure 22 are 0.113 and 0.144, respectively. These values are lower than the variances estimated for the simulated media because of the inherent experimental noise, which is Gaussian distributed as opposed to the intensity signal. The experimental values of the normalized variance are further reduced due to the presence of out-of-plane magnetic field components [12,184]. Moreover, the components of the electromagnetic field are not all independent and are not detected with the same sensitivity by the NSOM probe.

Even though a direct comparison with numerical results is not possible, the experimental situation is similar with the simulation results depicted in Figure 21(a-c): it is evident that increasing the structural non-uniformity leads to more asymmetric intensity distributions. It is also obvious that when describing the disorder fingerprints of different media one has to account for differences that go beyond the simple variances of these distributions. The values of increasingly higher-order moments demonstrate that small changes in extent of local disorder modify appreciably the shape of the intensity probability distribution, as shown in the inset in Figure 22(e).

In conclusion, these numerical experiments demonstrate that the near-field intensity distribution is a signature of the local scale-dependent morphology determined by variations of the local dielectric function. In

addition, we have shown that near-field intensity measurements expose spatial features of statistically homogeneous disorder which cannot be revealed by macroscopic ensemble methods [162]. We emphasize that this systematic study focused on media which differ only on their degrees of local structural homogeneity. Thus, these results establish a new and direct way to distinguish the scale-dependent morphology of random structures. Moreover, the results are pertinent for media which differ only on their degrees of local structural homogeneity as opposed to studies where different optical regimes are created by varying the average density of scatterers thus also influencing the overall macroscopic properties [65].

To exploit disorder as a design constituent, one needs to first characterize it and understand its role [190]. In this respect, measuring near-field statistics as demonstrated here renders details of both the structural morphology and the distribution of large field enhancements in complex media. This ability is critical for understanding the role of correlated disorder for enhancing the interaction between light and matter. Creating and controlling extreme photonic states in all-dielectric materials is of paramount importance not only for basic science but also for efficient engineering of light sources, for energy harvesting and sensing and for enhancing other optical effects such as, for instance, surrface-enhanced Raman scattering.

4.3 Near-Field Coherence Reveals Defect Densities in Two-Dimensional Materials

Conventional coherence theory describes universal properties of fields radiated by statistically homogeneous sources [191]. In practice however, sources have finite extends, their particular structure cannot always be neglected, and, sometimes the field correlations are measured in the proximity of the source where the influence of evanescent components can be dominant. As a result, the coherence properties are non-universal [187,192]. Most interestingly, coherence properties can be related to the structural morphology of the medium emitting the radiation and, therefore, can act as distinctive characterization tools [193]. For instance, in Refs. [166,194–196] it was shown that the extent of spatial coherence depends on the distance from the source of radiation and also on the field properties at its surface. Recently, a connection between the near-field speckle pattern and the internal structure of a randomly inhomogeneous medium has been revealed [186]. Based on measurements of spatial coherence, we introduce here a novel material characterization technique. In this section we demonstrate that the density of impurities or defects in two-dimensional crystalline lattices can be inferred from the spatial extent of the near-field correlations.

Defects in crystalline materials act as genuine Rayleigh scatterers. In two-dimensional structures, the inherently lower number of disturbance centers and their extremely weak scattering renders power measurements

practically impossible. We will introduce an elastic scattering method that mitigates these limitations and permits characterizing the structural homogeneity of two-dimensional materials. We will demonstrate that the simultaneous excitation along an ensemble of $\boldsymbol{k}$–vectors creates ideal conditions for examining the coherent elastic scattering that originates within the interface.

Practically, the efficacy of this new method will be exemplified on monolayer graphene, a material whose transport properties are severely affected by defects in its crystalline structure [197,198]. As recently shown [199–202], defective sites open new channels for electron cooling by providing extra momentum that allows for super-collisions with non-center acoustic phonons. This processes dramatically decrease the electron relaxation times, relatively long in pristine graphene, due to the high frequency of the optical phonons that hampers electron-optical phonon scattering rates. In this scenario, defect characterization processes are considered as essential steps throughout the fabrication chain of graphene-based devices, from synthesis to assembling [197,198,203,204]. Accordingly, the defect characterization in graphene has been broadly explored by different techniques such as scanning [205] and transmission [206] electron microscopies (SEM and TEM, respectively), scanning probe microscopies such as atomic force microscopy

(AFM) [207,208] and scanning tunneling microscopy (STM) [209], and Raman scattering [210–215].

The inelastic scattering of light by phonons in graphene (vibrational Raman scattering) is extremely sensitive to the amount and type of defects, and this sensitivity relates to the breaking-down of momentum conservation in the scattering processes mediated by the broadband spectrum of spatial of frequencies (wave vectors, $\boldsymbol{k}$) provided by the defects [210,211]. The relaxation of this momentum conservation-based selection rule gives rise to disorder-induced bands in the Raman signal, and the shape and relative intensity of these features provide both quantitative and qualitative information about the defects [210–215].

Although the inelastic scattering of light has been broadly employed to investigate defects in graphene [210,211], to the best of our knowledge, assessing the elastically (Rayleigh) scattered component has been, so far, out of reach. Since the defects are proven to act as important sources of extra momentum in the inelastic component of the scattered light, it is expected that momentum-related effects should be observed on the elastic part as well. Although commercially available dispersive spectrometers are able to analyze broad ranges of temporal-frequencies with high sensitivity, they are limited in terms of $\boldsymbol{k}$-space analysis (spatial-frequency domain). Besides, frequency analysis has no use for extracting information contained in monochromatic

Rayleigh lines generated in laser-based spectroscopy. For these reasons, the Rayleigh signals are usually treated as unwanted features in light scattering spectroscopy.

In the following we show that a ***k***–space spectroscopy can be developed where the Rayleigh component of scattered light is used directly to investigate the influence of defects on two-dimensional lattices such as graphene. The technique relies on illuminating the monolayer from underneath with a quasi-thermal monochromatic field (uniform ***k***-vectors distribution) and recoding the intensity of the transmitted radiation by means of a scanning near-field optical microscope (SNOM) using an aperture probe. Based on measurements of spatial coherence, this scheme allows practically for a ***k***–space analysis without the need of angle-dependent measurements. The approach takes into account the statistical properties of radiation in the near-field regime, where the defects provide a broadband source for extra momentum, which influences the ***k***-vectors distribution in the scattered field and, thus, modifies the spatial coherence properties of the emerging field. The information about the defect density is extracted from the spatial extent of the intensity-intensity correlations measured right above the graphene surface.

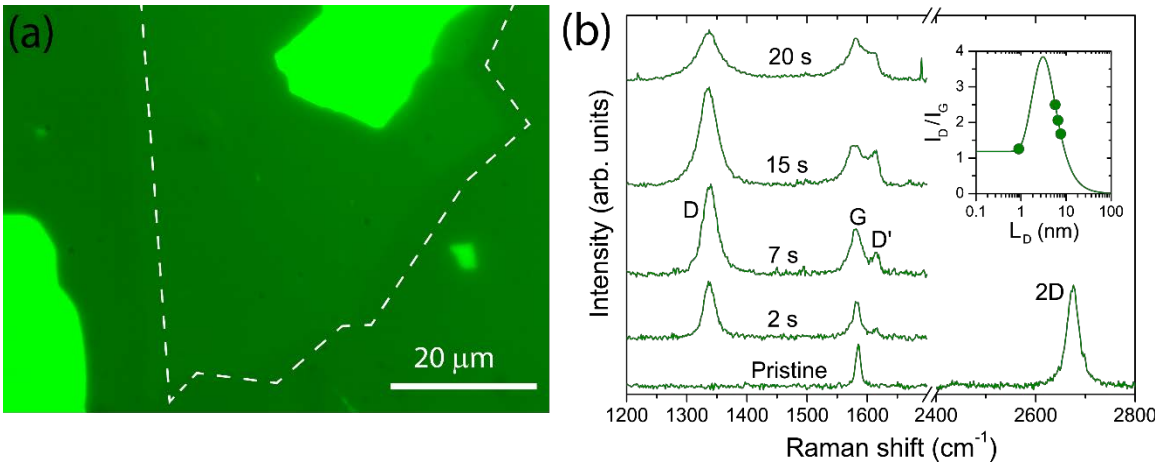

Figure 23: (a) Micrograph image of the graphene sample sitting on a cover glass substrate acquired in reflection mode. The green color is a digital filter applied for better visualization of the graphene layer. The dashed line reproduces the contour shape of the monolayer piece, and is slightly displaced from the edges (to the right) for better visualization. (b) Raman analysis of the graphene sample. The bottom spectrum corresponds to freshly produced sample. The one-phonon spectral range (1200-1700 cm^{-1}) shows the bond-stretching G mode at ~1580 cm^{-1}. The absence of the D band indicates that the sample is pristine. The single Lorentzian shape of the two-phonon 2D band (at ~2680 cm^{-1}) is evidence that the sample is single layer. Additional spectra were obtained after distinct steps of oxygen-plasma etching (the gradually increasing etching time is indicated for each spectrum). The presence of the D and D' bands at ~1330 and ~1620 cm^{-1}, respectively, indicate that the oxygen plasma etching has introduced structural defects in the graphene lattice. The inset depicts the I_D/I_G ratio as a function of the average distance between adjacent point defects, L_D. The solid line is a theoretical curve taken from Refs. [212,213]. The Raman spectra were obtained using a *Renishaw invia* Raman spectrometer equipped with a 514.5 nm laser line source. The sample was measured in back scattering with a 50X objective lens (NA 0.75, Leica) used for both illumination and collection. The laser power was kept below 1 mW to avoid sample damage

An optical image (micrograph) of a graphene flake sitting on a glass cover slip is shown in Figure 23(a). The graphene was produced following the mechanical exfoliation method reported in Ref [216]. Raman spectroscopy was used to monitor the sample's quality as detailed in Figure 23(b). The Raman spectrum of the freshly produced graphene (bottom spectrum in Figure 23(b)) reveals that the flake is a pristine monolayer without detectable defects.

To probe the elastic light scattering in the proximity of the graphene surface, the monolayer was illuminated through the supporting cover glass by a pseudo-thermal light source created at the output port of an integrating sphere (Thorlabs - IS200-4 - Ø2", 12.5 mm port diameter), which effectively scrambled the radiation from a 532 nm continuous wave laser radiation (100 mW power and spectral linewidth of <0.01 pm). The sample was positioned atop the exit port of the integrating sphere, and the near-field measurements of the resulting speckle patterns were performed using a *Nanonics MultiView 4000* NSOM system, working in standard collection mode, as schematically depicted in Figure 24(a). Near-field intensity distributions were collected across 6x6 μm^2 regions using a Cr-Au coated pulled silica fiber probe with 150 nm aperture diameter. The probe was attached to a quartz tuning fork and operated in intermittent contact while the optical signal was detected using a photon multiplying tube (PMT; *Hamamatsu, H7421*).

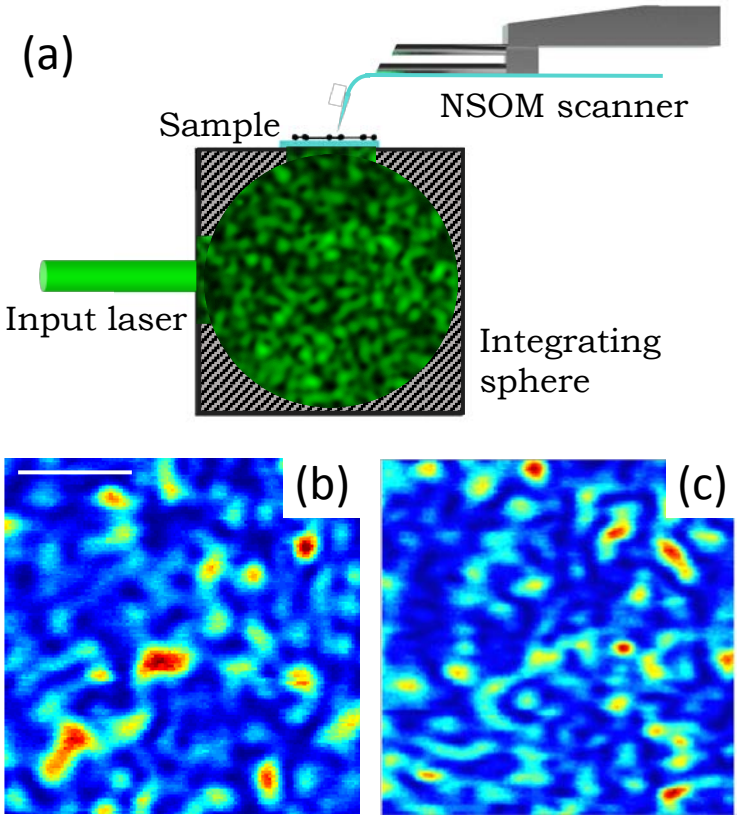

Figure 24: (a) Sketch of experimental setup used to analyze the light spatial coherence in the proximity of the graphene layer. b) High-resolution intensity maps corresponding to pristine graphene (lower left panel) and graphene with defect density of $n_D = 5.54\times10^{12}\text{cm}^{-2}$ (lower right panel). Scale bar is 2 μm.

A typical speckle image (high-resolution intensity map) recorded over a 6×6 μm² area of pristine graphene is shown in Figure 24(b). Similar measurements were performed over more than twenty different regions, which practically covers the whole sample area and to ensure appropriate ensemble average. Subsequently, the second-order intensity-intensity correlation was evaluated from the recorded intensity distributions. Using standard properties of Gaussian random variables, the field correlation function can be expressed in terms of the intensity correlation function. Following this procedure, the

average size (δ) of the speckle distribution was extracted from the radially-averaged full width at half maximum (FWHM) of the autocorrelation peak. For the pristine graphene, we found $\delta = 242$ nm. The same procedure applied to the field measured on the surface of bare glass results in an average speckle size $\delta = 243.5$ nm.

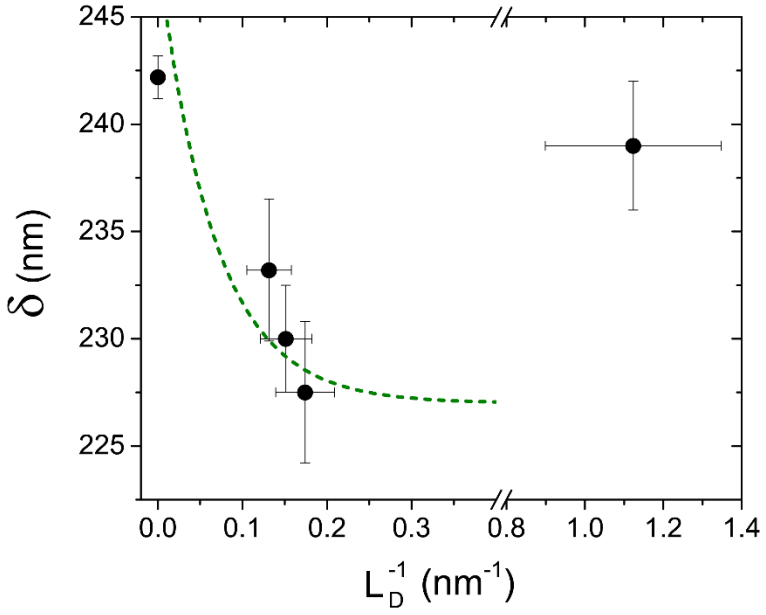

Figure 25: Average speckle size (δ) as a function of the inverse of the average distance between two point defects (L_D). The dotted line represents the exponential decay indicated in the coherence model (see text) corrected for the measurement point spread function.

To explore the effects of defective structures, we generated point defects in the same graphene piece through oxygen-plasma etching [217]. For that, the samples were exposed to oxygen plasma in a reactive ion etching (RIE) system, model *Plasma-Therm 790 SERIES*. An oxygen flow rate of 5 sccm diluted by a 50 sccm of helium flow was used. Gradual levels of defect densities were obtained by increasing the etching time, and the amount of defects was

monitored by Raman spectroscopy. The Raman spectra of the sample obtained after distinct steps of oxygen-plasma etching are shown in Figure 23(b). The intensities were normalized by the amplitude of the first order bond-stretching G band (~ 1580 cm^{-1}). The disorder induced D and D' bands (at ~1330 and ~1620 cm^{-1}, respectively) are absent (undetectable) in the Raman spectrum taken before the oxygen plasma etching starts (confirming that the starting sample was pristine), but become more and more intense as defects are introduced by the oxygen plasma etching process. Following previously established protocols [212,213], the average distance between point defects (L_D) was extracted from the I_D/I_G ratio (I stands for intensity, and the subscripts D and G label the respective bands). The experimentally obtained values of I_D/I_G are plotted as a function of L_D in the caption to Figure 23(b). The values of L_D were obtained from the solid line, which is a previously established model that links L_D to I_D/I_G [212,213]. It should be noticed that, although the first three steps of plasma etching generated defects in the sample, the graphene was not amorphous yet. This conclusion is based on the fact that the respective data points in the I_D/I_G vs. L_D plot fall on the right side of the theoretical peak curve indicating that, although the sample has structural defects, most of the net crystalline structure is still preserved. On the other hand, the Raman spectrum obtained after the fourth step of oxygen plasma etching (20 s) clearly shows that the I_D/I_G ratio recoiled (see top spectrum in

Figure 23(b)), indicating that the sample was in an advanced degree of amorphization.

A typical intensity map corresponding to defective graphene layer is shown in the lower panel of Figure 24(b) and, as can be seen, the average speckle size appears to be smaller than in the case of pristine graphene. The average speckle size was evaluated for all samples and the results are summarized in Figure 25 as a function of the inverse of L_D. We emphasize that the data were obtained from the same sample (albeit treated with different exposure times of oxygen plasma etching) in order to effectively cancel any possible influence from additional structural variations such as wrinkles of roughness. Moreover, all intensity maps were recorded using the same near-field probe. The data at $L_D^{-1} = 0$ corresponds to the starting sample of pristine graphene. It can be readily observed that, initially, the speckle size decreases when the density of defects rises. Note that increasing the defect density above a certain limit should eventually saturate this reduction of measured coherence length (speckle size). This can be explained by the finite dimension of each defective site, which can be attributed to the coherence length photo-excited electrons in graphene [218,219]. For sparse defect densities, each defective site acts independently to diminish the measured size of the speckle. However, when the effective defect sizes start to overlap at high densities, the sample becomes homogenously amorphous and the speckle size increases back to the values

corresponding to optically homogenous media close to that of pristine graphene. Therefore, it is clear that the scattering at the defective sites in graphene modifies rather significantly the extent of near-field spatial coherence.

The results summarized in Figure 25 can be understood as a modification of the angular spectrum of transmitted radiation. The strong scattering inside the integrating sphere randomizes effectively the electromagnetic field and creates at the exit port an emerging field with uniform angular spectrum typical to a Lambertian source. After passing through a dielectric interface, this uniform ***k***–space distribution is modified due to the angular dependence of the corresponding Fresnel transmission coefficients. In general, the effect of a dielectric slab will be to suppress the contributions of ***k***-vectors at small angles from the interface and, therefore, to increase the transversal correlation length. When additional isotropic scatterers are distributed across the surface, the ***k***-vector distribution tends to recover its initially isotropic shape because of the angularly uniform contributions from all the Rayleigh scattering centers. At very high defect densities, the monolayer acts again as a homogeneous structure with an effective dielectric constant as clearly seen in Figure 25.

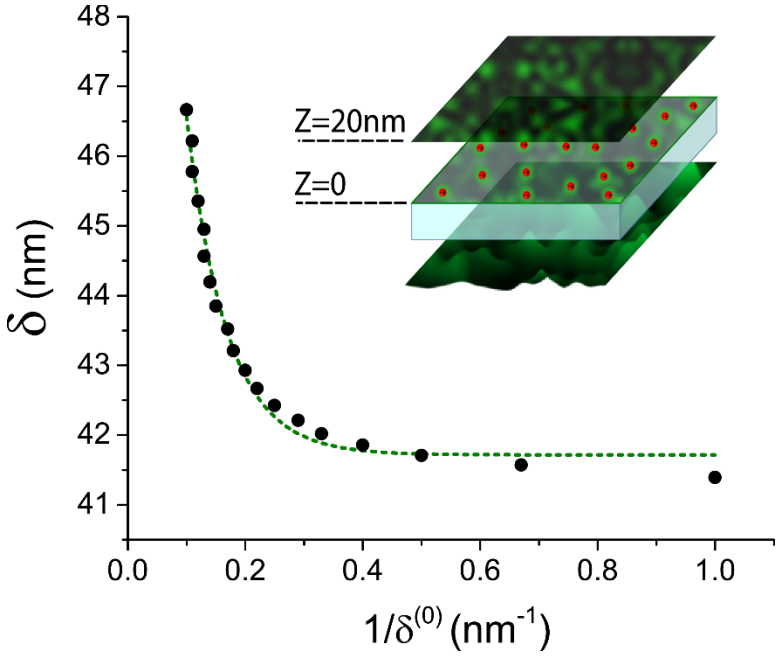

Figure 26: Spatial coherence length estimated in a plane situated at 20 nm from the surface of a source of radiation characterized by field-field correlations of extent $\delta^{(0)}$. The dotted line indicates an exponential decay

Nevertheless, the measurements are performed near the interface, at distances $z \ll \lambda$, where the field distribution is more complex. Here, the non-universal properties of spatial coherence above an interface are expected to reveal the characteristic length scales of medium's morphology [192]. An effective description considers the interface as a homogenous, planar, statistically stationary source of radiation which is characterized by a field-field correlation function $W^{(0)}(\delta) = \langle E(r)E^*(r+\delta)\rangle$ that extends over a characteristic distance $\delta^{(0)}$. Above the interface, the homogeneous and inhomogenous components of the field-field correlation function, $W^{(z)}(\delta) = W_{hom}^{(z)} + W_{ev}^{(z)}$, both depend on $W^{(0)}(\delta)$ but evolve differently with distance

z [187]. This is illustrated in Figure 26 where the width of the normalized correlation function, $\mu(\delta) = \langle E(r)E^*(r+\delta)\rangle / \langle |E(r)|^2 \rangle$ evaluated at $z = 20$ nm, is plotted as function of inverse of the extent $\delta^{(0)}$ of field-field correlations in the plane of the source. The sharp decay of this function suggests that measurements of spatial coherence should be quite sensitive to variations in the field distribution across the interface. This is the reason why, in our experiments, the measured speckle size in Figure 25 depends significantly on the average distance between point defects L_D, the length scale that determines the span of field-field correlations in the plane of the sample. Although we cannot provide an exact quantitative relationship between a measured average distance between two point defects and a generic model describing a statistically stationary source of radiation, the decays of the spatial coherence lengths are evidently similar. This suggests that the model captures the main features of the experimental behavior and, therefore, one can safely conclude that the two quantities L_D and $\delta^{(0)}$ are essentially the same.

We note that, in fact, we do not measure $W^{(z)}(\delta)$ directly. However, the strong field randomization produced by the integrating sphere effectively generates a statistically stationary field obeying circular Gaussian statistics. In this case, high-order correlation functions factorize into products of second-order correlations and, therefore, determining the spatial extent of the degree of spatial coherence $\mu(\delta) = \langle E(r)E^*(r+\delta)\rangle / \langle |E(r)|^2 \rangle$ amounts practically to a

measurement of the intensity-intensity spatial correlation function $\langle I(r)I(r+\delta)\rangle = 1 + |\mu(\delta)|^2$. This is exactly the correlation that can be inferred from intensity maps such as the ones illustrated in Figure 24. Of course, a direct comparison between the measured speckle size and the estimations based on the coherence model outlined here should also include corrections due to the point spread function (PSF) of the NSOM probe. This is illustrated in Figure 25, where the predictions of this model corrected for the experimental PSF (dotted line) make a good description of the dependence between the measured speckle size and the average distance light. between point defects in the graphene monolayer.

In conclusion, we have demonstrated a novel and counter-intuitive phenomenon: an effectively transparent atomic monolayer is cable of modifying the coherence properties of radiation transmitted through it. We have proved a direct relationship between statistical properties of the optical near fields and the structural properties of two-dimensional materials. This demonstration can lead to new means for controlling complex properties of optical radiation at subwavelength scales.

We have shown that spatial coherence measurement in the proximity of two-dimensional interfaces constitute a rather general, elastic scattering approach for establishing the presence and assessing the density of defects in two-dimensional crystalline materials. This is notoriously difficult for

transparent materials where the amount of scattered power is minimal and the so-called Rayleigh scattering is most of the time impractical.

The new technique was validated on two-dimensional graphene lattices with controllable defect densities and we have shown that, notably, finding the average number of surface defects does not require elaborate inelastic measurements. A relative assessment of the spatial coherence length characterizing the incident and the scattered fields is sufficient to determine the density of defects, which is in the order of thousands of defects per square wavelength. The use of the coherence as a degree of freedom in characterization protocols is largely unexplored in material sciences. Our findings provide a simple and robust way to access structural properties that are traditionally accessed by inelastic scattering of light.

4.4 Passive Near-Field Imaging with Pseudo-Thermal Sources

There is a plethora of techniques aimed at measuring optical fields in the proximity of interfaces and relate them to the properties of material systems [220–222]. The term "near-field" is applicable to those situations in which the detection is performed at distances shorter than the characteristic wavelength λ of the optical field [220–222]. Near-field optical techniques are usually regarded as either passive or active, depending on how the probe and sample come into play. If the probe acts to control the incident radiation field, the technique is usually said to be active. The approach closest to being passive is the common collection mode where the sample (interface) is illuminated from the far zone,

and an aperture probe is used to collect the scattered field [223,224]. Of course, the sole presence of the probe in the near-field modifies the field and, in this sense, there is no absolute passive near-field measurement.

The detection of evanescent components of optical fields at sub-wavelength regimes allows for accessing spatial resolutions [223–227] and coherence lengths [186,187,194,196,228–230] shorter than $\lambda/2$ (the diffraction limit), contrary to the far-field case. For these reasons near-field scanning optical microscopy (NSOM) has been employed to study novel manifestations of light-matter interactions at deep sub-wavelength levels, and for performing optical imaging at nano-scale [150,151,159,161,185–195] However, the close-proximity between the probe and the interface has several undesired consequences [231–237]. Here we will focus in a specific type of artifact, caused by the strong interferences that occur when coherent radiation is used for illumination [234–237]. Previous theoretical works have asserted that, due to these interference effects, the actual profile of a scattering surface is unlikely to be correctly recovered, even if complex inversion algorithms are applied to the recorded intensity profile [234–237]. In these conditions, the measurements cannot be truly passive. It was also suggested that the detrimental effect of interference could be diminished by reducing the state of coherence of the illumination field [235–237].

In this section we will demonstrate that the effect of multiple scattering in passive near-field imaging can be effectively eliminated when the sample is illuminated with a dynamic spatially incoherent source. The efficient randomization of the incident field allows for the scattered field to be essentially integrated over all possible angles of incidence. As a result,

the recorded intensity becomes an effectively incoherent superposition of fields that washes out interference effects. The profile of the scattering surface can be readily reconstructed from the detected intensity image by taking into account the convolution with the point spread function of the aperture probe.

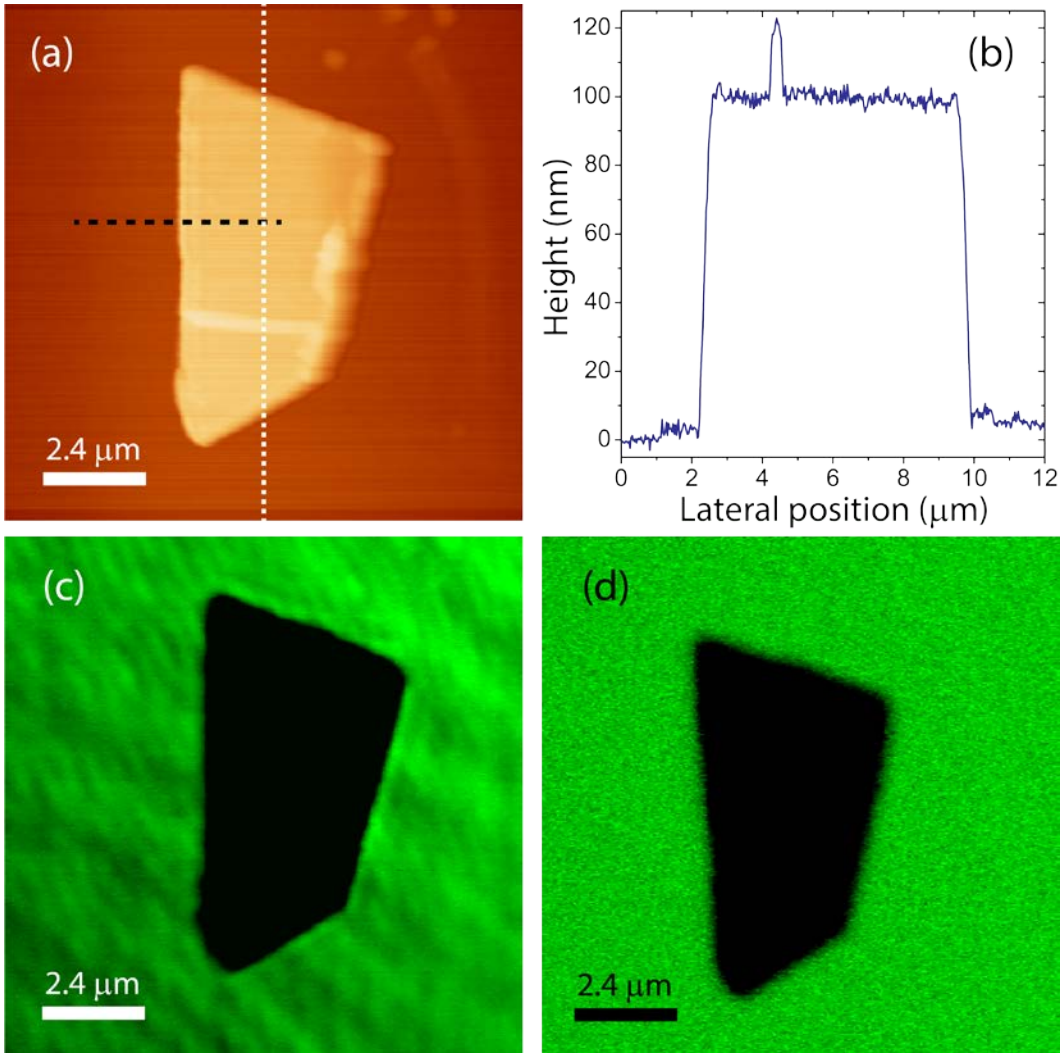

Figure 27: (a) Topographic image of a graphite flake on a glass substrate. (b) Height profile extracted along the vertical dotted line in (a). (c) Aperture-NSOM image obtained simultaneously with the topographic image shown in panel (a). A linearly polarized laser source was used to illuminate the sample, as depicted in Figure 28(a). (d) Like (c), but using the pseudo-thermal source illustrated in Figure 28(b).

Figure 27(a) shows the topographic image of a graphite sheet sitting on a glass substrate. The height profile [Figure 27(b)] reveals that the piece is ≈100 nm thick. The topographic image was obtained by means of atomic force microscopy (AFM), using a Nanonics MultiView 4000 NSOM setup. The schematics of the setup is illustrated in Figure 28(a). The AFM image was obtained simultaneously with the optical image shown in Figure 27(c), for which the graphite sheet was illuminated from underneath by an unfocused (wide field) linearly polarized laser beam (532 nm wavelength, 100 mW output power). The optical signal was collected with a Cr-Au coated pulled silica fiber probe with 150 nm aperture diameter, also used as AFM probe. The probe was attached to a quartz tuning fork and operated in intermittent contact while the optical signal was detected using a photon multiplying tube (PMT; Hamamatsu, H7421).

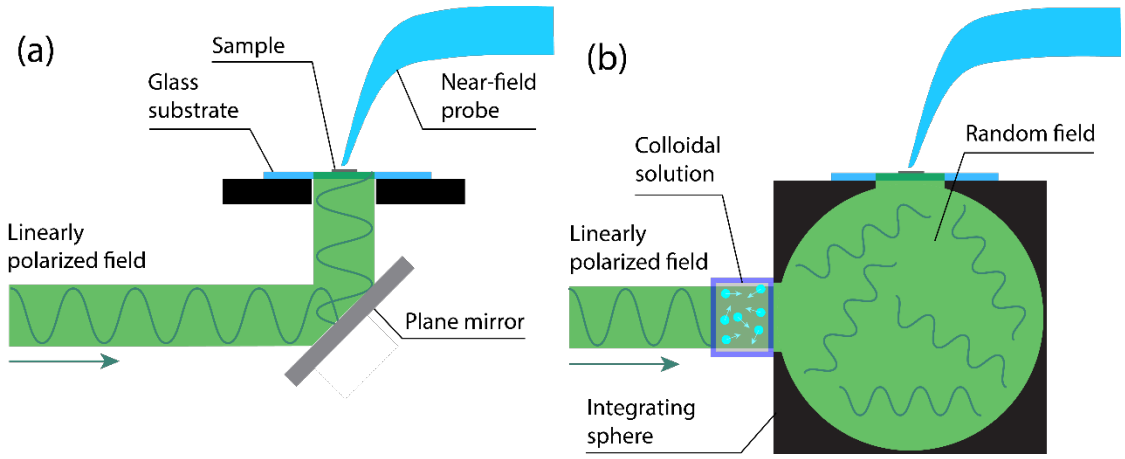

Figure 28: Schematics of aperture-NSOM measurements. (a) Typical wide field coherent illumination: the sample is illuminated from underneath by a linearly polarized laser beam and the near-field is collected with a Cr-Au coated silica fiber tip. (b) Pseudo-thermal illumination: the laser beam first impinges on a colloidal suspension where it undergoes a dynamic multiple scattering and then is coupled to the input port of an integrating sphere. The sample is positioned against the exit port of the integrating sphere and the near-field is detected by the same fiber tip as in (a).

As shown in Figure 27**(c),** the shape and position of the graphite piece is clearly seen in the optical image due to the strong contrast generated by absorption and reflection of the illuminating laser beam. However, the image is severely marked by interferences, also found in similar images obtained from other pieces (not shown). There are multiple sources for these interferences including minimal perturbations due to scattering by small particles attached to the substrate or inhomogeneities of the substrate itself. It is this high-susceptibility to small perturbations that makes the coherent wide field illumination unsuitable for passive near-field imaging.

Besides those surface-related perturbations, the near-field distribution is also affected by interferences due to multiple scattering between the sample and the probe [232,234,235] . This effect can be seen in Figure 29(b), showing the intensity profile of the graphite edge obtained along the dashed line in Figure 27(a). The profile presents fringes generated by the superposition of coherent fields. Similar fringes were observed in other line profiles obtained from several different pieces, with distinct thicknesses and shapes. One example is presented in Figure 30, which show similar data obtained by a much thinner piece ≈10 nm thick, according to the height profile extracted from the AFM image show in Figure 30(a)]. The upper graphic in panel (d) shows the intensity profile of the near-field signal taken along the dashed line indicated in panel (a). This intensity profile was obtained through coherent illumination [schematics shown in Figure 28(a)], and presents similar interference patterns shown in Figure 29(b). These patterns are generated by the superposition of fields from multiple scattering events.

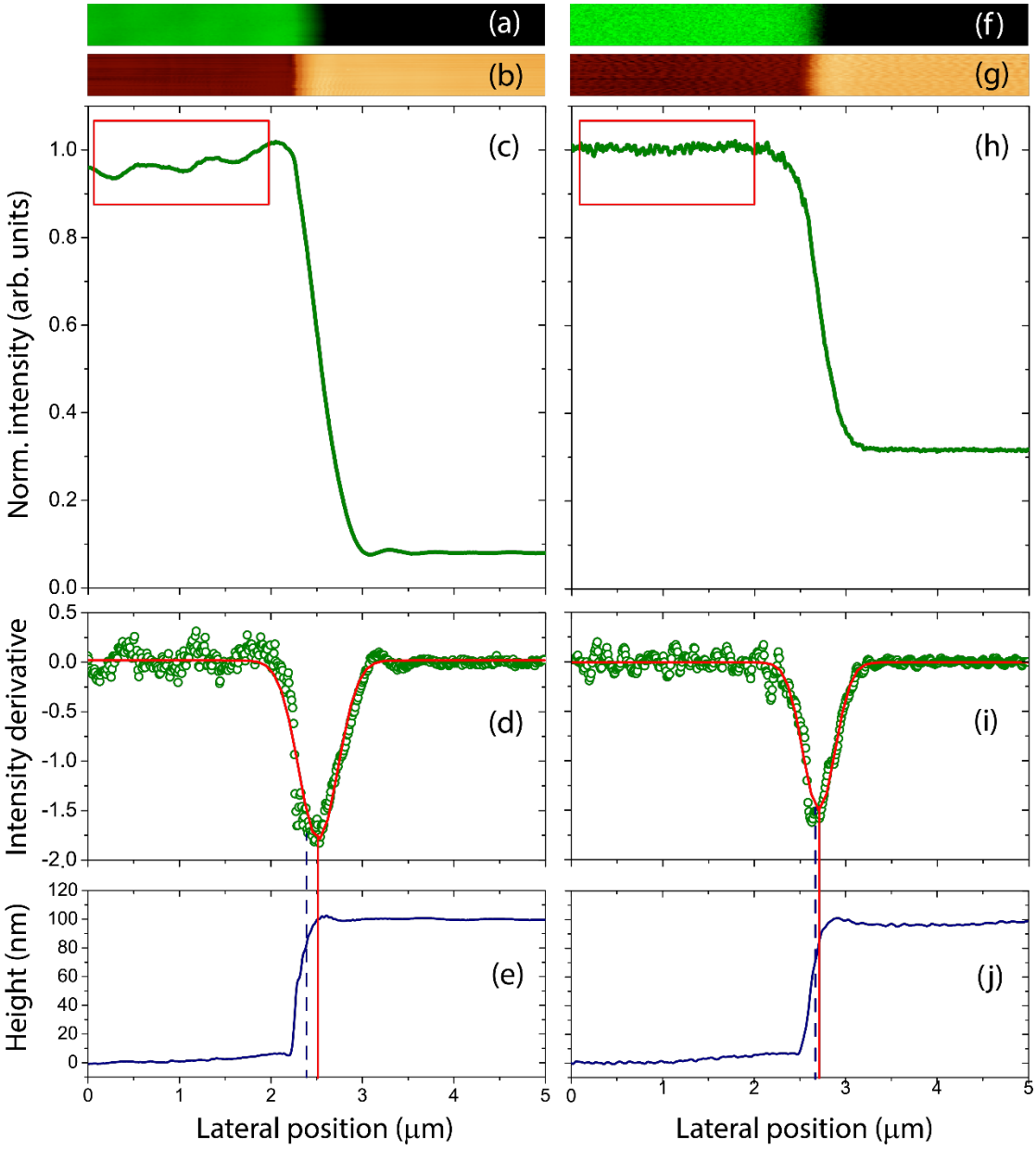

Figure 29: Data recorded along the dashed line in Figure 27(a) under coherent illumination (left panels) and pseudo-thermal illumination (right panels). (a,f) and (b,g) Near-field intensity and AFM images, respectively, obtained by performing 50 scan lines at the same position along the slow scan axis (slow scan off). (c,h) Near-field intensity profiles obtained by averaging the 50 lines shown in (a,f). (d,i) Derivatives of the intensity profiles shown in (c,h). The red lines are Gaussian fit. (e,j) AFM height profiles obtained by averaging the 50 lines shown in (b,g). The solid and dashed vertical lines in panels (d,e) and (i,j) indicate, respectively, the lateral position of the center of the Gaussian functions in (d,i), and the lateral position of the edge extracted from the height profiles in (e,f).

To overcome the problem with the interference patterns observed in the aperture-NSOM images, we designed the setup illustrated in Figure 28(b). As depicted in the schematics, the incident laser passes first throughout a colloidal dispersion made of polystyrene beads with 330 nm diameter in distilled water with concentrations of 1% wt. The room temperature Brownian motion of the beads makes this dispersion to work as a dynamical diffuser with long stability time. The dynamical scattering of the incident laser field gives rise to quickly changing uncorrelated speckle patterns [238,239]. The decorrelation times of this dynamic speckle field is on the order of 1 μs [238,240]. This time frame is significantly shorter than the integration time of the measurement which is in the order of 10 ms per pixel. As a result, the outgoing field distribution resembles closely a thermal field examined at the laser frequency.

To minimize scattering losses and homogenize the intensity distribution even more, we placed the colloidal solution next to entrance port of an integrating sphere (Thorlabs - IS200-4 - Ø2", 12.5 mm port diameter), as illustrated in Fig. 2(b). Thus, the sample, which is positioned at the exit port, is practically exposed to a monochromatic, depolarized, and uncorrelated random field. Because the size of the exit port is five orders of magnitude larger than that of a typical NSOM scan, the field distribution across the exit port effectively represents an infinitely extend source of monochromatic and spatially incoherent radiation. Such pseudo-thermal source generates a Lambertian distribution of intensities. The corresponding results of using this pseudo-thermal monochromatic source for aperture-NSOM imaging are shown in Figure 27(d) and Figure 30(c). As clearly seen, the interference patterns are effectively eliminated, and the intensities are uniform.

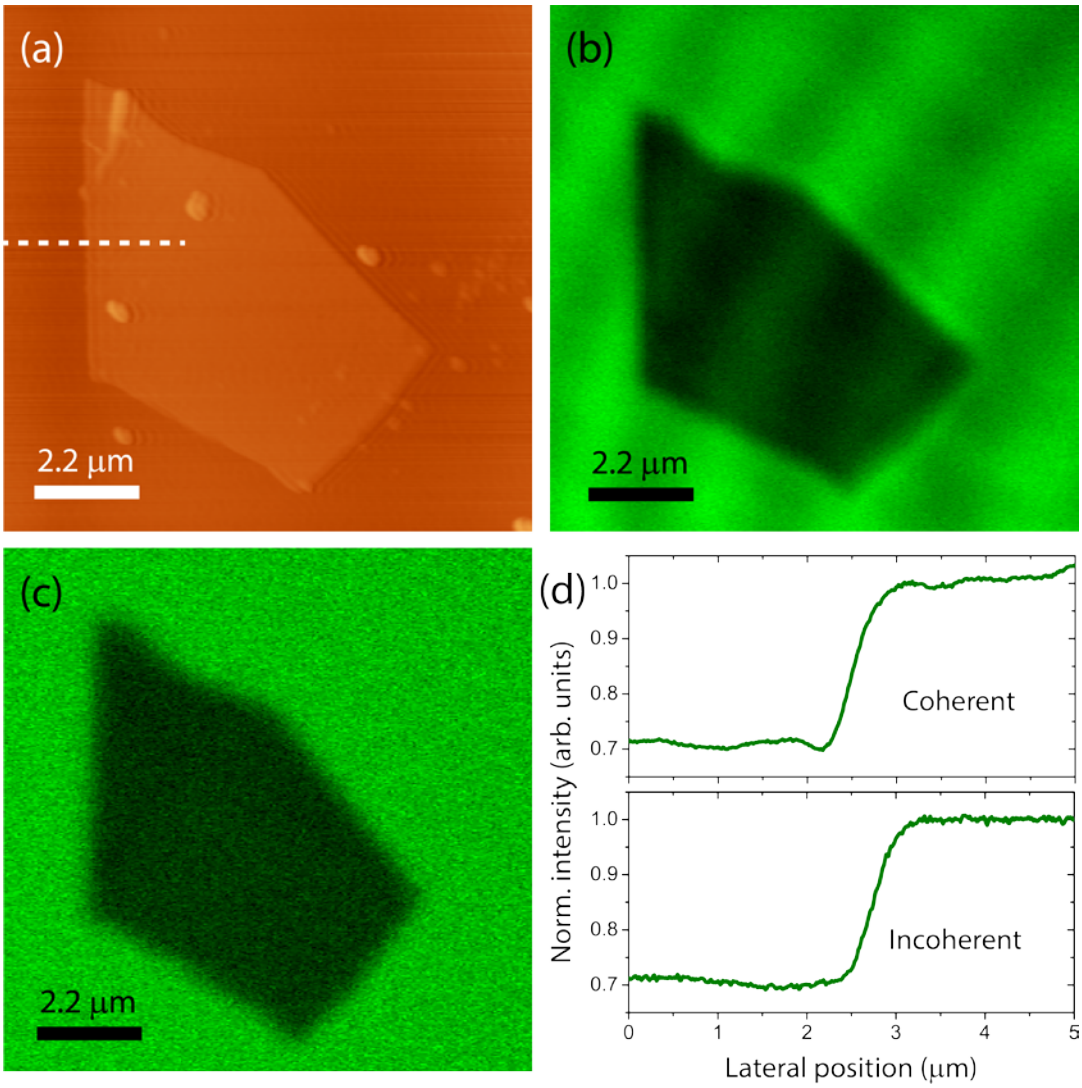

Figure 30: (a) Topographic image of a graphene flake on glass substrate. The height profile (not shown) reveals that this flake is ≈10 nm thick. Aperture-NSOM images were obtained under (b) coherent and (c) pseudo-thermal illumination. (d) Intensity profiles recorded along the dashed line in panel (a). The upper and lower graphs were obtained with the linearly polarized coherent laser source and the pseudo-thermal source, respectively. Both profiles are the average of 50 scan lines at the same position (slow scan axis off).

It should be noticed that all data shown in this letter were obtained with the same aperture probe, excluding differences caused by different probes. Therefore, we can directly analyze the imaging performance of the two illumination modalities depicted in Figure 28 by comparing the line profiles across an interface. This analysis is presented in

Figure 29. It is evident that the near-field intensity profile in Figure 29(h), obtained with the pseudo-thermal source [schematics shown in Figure 28(b)], is sharper and less affected by spurious artifacts than the one in Figure 29(c), obtained using the coherent laser source in wide illumination geometry [schematics shown in Figure 28(a)]. A quantitative notion about the uniformity of these two intensity profiles can be obtained by evaluating the variance of the data confined in the boxed areas in Figure 29(c,h), which cover a 2 μm extent (located at least 1 μm far from the edge) on top of the bare glass. Indeed, the variance is 8.5 times larger in the case of wide field coherent illumination (3.4×10^{-4} versus 4.0×10^{-5} for the pseudo-thermal light source). A similar qualitative comparison can be made by simple visual inspection of the upper and lower graphs in Figure 30(d), showing the intensity profiles obtained across the few-layer graphene's sharp edge.

Another important information extracted from the comparative analysis shown in Figure 29 is a considerable improvement in spatial resolution provided by the pseudo-thermal illumination. As proposed in Ref [235], the actual profile of the scattering surface can be extracted from a near-field intensity image resulting from the superposition of images obtained at different angles. The imaging processing can be evaluated by considering the point spread function of the collecting optics, which is determined by the near-field aperture probe in the present case. Of course, the opposite is also possible: prior information about the profile of the scattering surface can be used to reveal the point spread function of the probe. Since the optical response from the knife edge approximates to a step function, the derivative of the intensity profile reflects the point spread function of the near-field probe, which in turn defines the spatial resolution achieved in the imaging

process. These derivatives are shown in Figure 29(d,i) (open circles) for the data obtained with the coherent laser and the pseudo-thermal light source, respectively. As can be seen in the plots, the intensity derivative is close to a symmetric Gaussian in the pseudo-thermal illumination [Figure 29(i)], as opposed to the case of coherent illumination [Figure 29(d)] for which the tentative Gaussian fit (solid line) visibly fails. The Gaussian fitting procedure reveals a full-width at half maximum of ≈350 nm for the pseudo-thermal illumination, and of ≈430 nm for the coherent laser wide illumination, indicating ≈20% higher spatial resolution in the case of pseudo-thermal illumination. The gain in spatial resolution was expected, since the pseudo-thermal source provides a broadband spectrum of spatial frequencies. The cost for this wide angular spectrum is the loss of contrast due to the extra light collected through the lateral of the probe. The lower contrast is evident by comparing the intensity profiles shown in Figure 29(c) and (h). This loss of contrast is much less evident in the measurement performed at the few-layer graphene sample [see profiles in Figure 30(d)].

Finally, we use the data presented in Figure 29 to analyze the gain in position accuracy due to the pseudo-thermal illumination. The lateral position of the step edge can be extracted from the AFM height profiles shown in Figure 29(e,j), which were obtained concomitantly with the respective nearfield intensity profiles shown in Figure 29(c,h). The edge position is marked by the vertical solid line in each case. These lines extend up to Figure 29(d,i) for direct comparison with the center of the Gaussian function obtained in each case. Considering the geometry of our experiment, the lateral position of the derivative maximum (center of the Gaussian) should occur at the edge's position. In the

case of the wide-field coherent illumination [panels 3(d,e)], the center of the spurious Gaussian is shifted by 130 nm from the actual edge position defined by the AFM height profile. This discrepancy is a direct consequence of the asymmetric shape the near-field intensity profile. For the pseudo-thermal light source, the center of the Gaussian is dislocated by 40 nm from the edge position. This value is ≈10% of the spatial resolution achieved in the experiment, and certainly smaller than the uncertainty in the AFM measurement.

The results presented in this section illustrate a simple solution for a significant deficiency of near-field microscopy. We demonstrated that spurious interference patterns can be effectively removed from passive near-field images obtained with aperture probes [241]. These artifacts originate in the coherent superposition of fields scattered at different locations within the illuminated volume and have been theoretically discussed more than two decades ago [232,234,235,237]. A pseudo-thermal monochromatic source that effectively eliminates the interferences due to multiple sources of scattering within the illuminated volumes that includes both the sample and the necessary substrate. The new source for passive near-field imaging is based on a common off-the-shelf CW laser, a colloidal solution, and an integrating sphere and is considerably simpler than alternatives such as random lasers [238,242,243], broadband or multiple lasers [244], or low spatial coherence multimode lasers [245].

4.5 Summary

In this Chapter, we first demonstrated that the structural correlation of disorder influences the outcome of light matter interaction even in the regime of multiple scattering. We present a detailed experimental and computational study on how the spatial correlation between individual scattering centers influences the fluctuations of intensity in the near-field of highly scattering media. We have shown that the far-field measurements depend only on averaged characteristics such as scattering mean free path. Therefore, the information specific to material structure is limited. Near-field measurements on the other hand Measuring the statistical property of intensity as demonstrated in this Chapter, renders details of both the structural morphology and the distribution of large field enhancements in complex media. This ability is critical for understanding the role of disorder for enhancing the interaction between light and matter.

Creating and controlling extreme photonic states in all-dielectric materials is of paramount importance not only for basic science but also for efficient engineering of light sources, for energy harvesting and sensing. describe local field configurations and reflect essentially non-Gaussian processes determined by the detailed material structure. We have also demonstrated that the coherence properties, measured in the proximity of the source where the influence of evanescent components can dominate, are non-universal and can be related to the morphology of the medium emitting the radiation. Therefore, this extent of spatial coherence can act a distinctive characterization tool. More specifically, based on measurements of spatial coherence in the proximity of an interface we have demonstrated

that the spatial extend of the near-field correlations depends on the density of impurities or defects in two-dimensional crystal lattices.

Finally, we discussed another direct consequence of the coherence properties of the proximity of material interfaces. We demonstrated experimentally that the effect of multiple scattering in passive near-field imaging can be effectively eliminated when the sample is illuminated with an effectively spatially incoherent radiation. The efficient randomization of the incident field allows for the scattered field to be essentially integrated over all possible angles of incidence. As a result, the recorded intensity becomes an effectively incoherent superposition of fields that washes out interference effects.

CHAPTER 5: CONCLUSIONS AND SUMMARY OF ORIGINAL CONTRIBUTIONS

Mesoscopic Optics is benefitting from continuous conceptual and experimental progress. During the last decades, remarkable advances were achieved in a variety of fields ranging from biological tissues to composite materials, and from colloidal physics to fabricated nanostructures. Mesoscopic optics describes the interaction between electromagnetic waves and complex material systems. This regime is dominated by very strong scattering, a rather complicated but still linear and deterministic process. The prefix "meso-" originates from the Greek word "mesos", which means middle. but there is no well-defined mesoscopic length scale somewhere between micro and macroscales.

In fact, the "mesoscale" is defined by the interacting system's properties, which includes both the medium and the electromagnetic field. Therefore, the properties of a mesoscopic system are specified by the scale, the duration, and the strength of the electromagnetic interaction. The typical characteristic length scales of such a system are the average size of the scatterers, the wavelength of incident field, the scattering and the transport mean free paths, the phase coherence length, and the overall size of the medium. At mesoscales, the scattering is strong (scattering length is in the order of the wavelength) but it does not destroy completely the coherence, which means that we are in a regime where the interaction scale is smaller than the coherence length of radiation. Therefore, the interaction is dominated by local interferences. Due to the phase correlation between the scattered waves, each realization of the light matter interaction is a member of a statistical ensemble that has its own pattern of fluctuations.

A variety of interesting optical effects occur in the mesoscopic regime of interaction. Taking advantage of this phenomenology for designing new sensing techniques or for engineering materials that can efficiently control the properties of light requires a thorough understanding of the physics of light propagation in complex disordered media. A significant research effort was dedicated to the intricate process of light interacting with complex random media. However, in the important case of dense complex media where the separation between consecutive scattering sites is less than the wavelength of the light, the progress has been limited. After reviewing different regimes of light transport, in Chapter 2 of this dissertation, we have quantitatively described the characteristics of multiple light scattering in dense composite materials. We presented a novel propagation model for evaluating the transport mean free path throughout the entire range of possible concentrations of scattering centers in the static disordered media. We have also demonstrated the emergence of a new regime of transmission, which can be described in terms of physically meaningful and measurable quantities such a near-field scattering cross section. We have shown for the first time that, in this regime, additional transmission channels open because of the near-field interactions among scatterers placed in close proximity. A full-scale calculation of the electromagnetic field distribution in 3D random media indicates the emergence of additional channels for energy transfer. The model is also supported by the results of a comprehensive enhanced backscattering experiment. We found that the transport mean free path corresponding to the different concentrations of scatterers is in very good agreement with our model for the near-field corrected transport. The use of such detailed descriptors for individual scattering events

not only improves the macroscopic description of light propagation in random media, but also enhances the predictive capabilities of light transport models [J3,C1,C3,C7,P2,P5].

We have also provided an inclusive description of the evolution of light in dense complex media. We presented the first experimental evidence that different stages emerge in this evolution, which cannot be described by classical diffusion with conventional scaling arguments. Our results demonstrate that the average residence time in this confining potential is regulated by the strength of the inherent evanescent coupling among microscopic elements of the complex medium. In particular, we have shown that strong recurrent scattering due to on-shell propagating fields is impeded by strongly localized evanescent couplings (off-shell wave manifestations). The fact that the transport of optical waves cannot slow down indefinitely is of high relevance for the elusive Anderson localization of light in three-dimensional media [J6,C11,C14,C16,P3].

In Chapter 3, we introduced a viable design strategy to efficiently control properties of the scattered light. We have shown that by appropriate design of the internal structure of a single scatterer, one can achieve full control on the characteristics of the scattered light. We have demonstrated that simple structural modifications in all-dielectric materials provide means to achieve extreme optical properties without the necessity for appealing to exotic materials or complicated manufacturing procedures. Specifically, we have shown that a dielectric core-shell particle allows not only to significantly control the scattering directivity, but also to adjust the extinction cross section. Core-shell dielectric structures with spherical symmetry provide the necessary flexibility in exciting higher-order spherical modes and, therefore, provide means to control the directivity of scattered radiation.

Furthermore, we demonstrated that the polarization of light can be controlled by breaking the azimuthal symmetry in the internal structure of a single spherical particle [J4,J1,C9,C5,P1]. Aside from the wave-specific properties, we have also shown that heterogeneous composite microspheres can distribute uniformly the scattered power. Acting as a dipolar entity for power redistribution, such a structure is orders of magnitude more efficient than a point dipole [C6,C8,C12,C15,P4].

In Chapter 4 of this dissertation, the fundamental understanding of the physics of light propagation in disordered media at mesoscales was used to develop novel sensing modalities. We established a new and direct way to distinguish the scale-dependent morphology of random structures. Our numerical experiments demonstrated that the near-field intensity distribution is a signature of the local scale-dependent morphology determined by variations of the local dielectric function. In addition, we have shown experimentally that near-field intensity measurements expose the spatial features of a statistically homogeneous disorder, which cannot be revealed by macroscopic ensemble methods [J5,C10,C12].

We have also demonstrated a novel and counterintuitive phenomenon where an essentially transparent atomic monolayer is capable of modifying the coherence properties of radiation transmitted through it. We have proved a direct relationship between statistical properties of the optical near fields and the structural properties of two-dimensional materials. This demonstration can lead to completely new means for controlling complex properties of optical radiation at subwavelength scales. We have shown that a spatial coherence measurement performed in the proximity of two-dimensional interfaces

constitutes a rather general, elastic scattering approach for establishing the presence and assessing the density of defects in two dimensional crystalline materials. This is notoriously difficult for transparent materials where the amount of scattered power is minimal and the so-called Rayleigh scattering is most of the time impractical. We have shown that, a relative assessment of the spatial coherence of the incident and the scattered field is sufficient to determine the density of defects, without resorting to elaborate inelastic measurements. Finally, the use of the coherence degree of freedom in characterization protocols is largely unexplored. Our findings provide a simple and robust way to access structural properties that are traditionally probed only by inelastic scattering of light [J8,C13].

At the end of the Chapter 4 we suggested a simple solution to overcome the typical problem with the interference patterns observed in the aperture-NSOM images. These artifacts originate in the coherent superposition of fields scattered at different locations within the illuminated volume. We demonstrated experimentally that spurious effects caused by this interference phenomenon can be effectively eliminated in passive near-field imaging by implementing a simple illumination with spatially incoherent light [J7,C17].

PUBLICATIONS AND PRESENTATIONS

Refereed Journal Papers

J8. **Roxana Rezvani Naraghi**, Luiz Gustavo Cançado, Félix Salazar-Bloise and Aristide Dogariu, "Near-field coherence reveals defect densities in two-dimensional materials", submitted to Optica, (2016).

J7. Luiz Gustavo Cançado, **Roxana Rezvani Naraghi** and Aristide Dogariu, "Passive near-field imaging with pseudo-thermal sources", Optics Letters, **42**, 1137-1140 (2017).

J6. **Roxana Rezvani Naraghi** and Aristide Dogariu "Phase transitions in diffusion of light", Phys. Rev. Lett. **117**, 263901 (2016).

J5. **Roxana Rezvani Naraghi**, Sergey Sukhov, and Aristide Dogariu, "Disorder fingerprint – intensity distributions in the near-field of random media", Phys. Rev. B **94**, 174205 (2016).

J4. G. Tao, J. J. Kaufmann, S. Shabahang, **Roxana Rezveni Naraghi**, S. V. Sukhov, A. Dogariu, and A. F. Abouraddy. "Digital design of multimaterial photonic particles". Proceedings of the National Academy of Sciences (2016).

J3. **Roxana Rezvani Naraghi,** Sergey Sukhov, Juan Jose Sáenz, Aristide Dogariu, "Near-Field Effects in Mesoscopic Light Transport," Phys. Rev. Lett. **115**, 203903 (2015).

J2. Sergey Sukhov, Veerachart Kajorndejnukul, **Roxana Rezvani Naraghi** and Aristide Dogariu, "Dynamic consequences of optical spin–orbit interaction," Nature Photonics (2015).

J1. **Roxana Rezvani Naraghi**, Sergey Sukhov and Aristide Dogariu, "Directional control of scattering by all-dielectric core-shell spheres," Optics letters **40**, 585-588 (2015).

Conference Proceedings

C17. **Roxana Rezvani Naraghi,** Luiz Gustavo Cançado and Aristide Dogariu "Near-field Imaging with Pseudo-thermal Sources", CLEO,2017.

C16. **Roxana Rezvani Naraghi** and Aristide Dogariu "Phase Transitions in Diffusion of Light", CLEO,2017.

C15. Felix A. Tan, **Roxana Rezvani Naraghi**, Ruitao Wu, Behnaz Davoudi, Aristide Dogariu and Ayman F. Abouraddy, "Diffusive Optical Coatings Loaded with Multiscale Composite Microspheres Produced from Multimaterial Fibers", MRS Spring Meeting, 2017.

C14. Aristide Dogariu and **Roxana Rezvani Naraghi** "Phase transitions in diffusion of light", PQE,2017, invited talk.

C13. **Roxana Rezvani Naraghi**, Luiz Gustavo Cançado, Félix Salazar-Bloise, Aristide Dogariu, "Quantifying Defect Densities in Monolayer Graphene Using Near-field Coherence Measurements", Frontiers in Optics,2016.

C12. Felix Tan, **Roxana Rezvani Naraghi**, Sergey Sukhov, Aristide Dogariu, Ayman Abouraddy, "Diffusive Scattering from a Single Composite Microsphere Fabricated by an In-Fiber Fluid Instability", Australian Conference on Optical Fibre Technology, 2016.

C11. **Roxana Rezvani Naraghi**, Marielena Burdge, Sergey Sukhov and Aristide Dogariu, "Near-field interactions and anomalous diffusion of light in disordered media", CLEO, 2016.

C10. **Roxana Rezvani Naraghi**, Sergey Sukhov and Aristide Dogariu "Disorder fingerprint – the distribution of local density of states in random media", CLEO, 2016.

C9. **Roxana Rezvani Naraghi**, Guangming Tao, Joshua Kaufmann, Soroush Shabahang, Sergey Sukhov, Ayman Abouraddy and Aristide Dogariu, "Tuning Light with Photonic Particles", CLEO, 2016.

C8. Felix Tan, **Roxana Rezvani Naraghi**, Marielena Burdge, Aristide Dogariu Ayman Abouraddy, "Diffusive Scattering from Single Microspheres with Well-Dispersed Dielectric Nano-Scale Inclusions", CLEO, 2016.

C7. **Roxana Rezvani Naraghi**, Sergey Sukhov, and Aristide Dogariu. "Light transport in dense composite media: role of near-field coupling", APS March Meeting, 2016.

C6. Felix A. Tan, **Roxana Rezvani Naraghi**, Marielena Burdge, Sergey Sukhov, Aristide Dogariu, Ayman Abouraddy “Diffusive multi-scale spheres based on composite polymer systems” SPIE Photonics West,2016.

C5. **Roxana Rezvani Naraghi**, Sergey Sukhov, and Aristide Dogariu. "Designing All-Dielectric Structures for Efficient Directional Scattering." Frontiers in Optics. Optical Society of America, 2015.

C4. Sergey Sukhov, Veerachart Kajorndejnukul, **Roxana Rezvani Naraghi**, and Aristide Dogariu. "Mechanical Action of Optical Spin-Orbit Interaction." Frontiers in Optics. Optical Society of America, 2015.

C3. **Roxana Rezvani Naraghi**, Sergey Sukhov, and Aristide Dogariu. "Near-field Corrections in Mesoscopic Transport." Laser Science. Optical Society of America, 2015.

C2. **Roxana Rezvani Naraghi**, Sergey Sukhov, and Aristide Dogariu. "Near-Field Intensity Fluctuations: the Role of Disorder Correlations." Laser Science. Optical Society of America, 2015.

C1. **Roxana Rezvani Naraghi**, Sergey Sukhov, and Aristide Dogariu. "Near Field Measurements of the Scattering Phase Function with Evanescent Field Excitation." CLEO: QELS_Fundamental Science, OSA 2015.

Poster Presentations

P5. **Roxana Rezvani Naraghi,** Sergey Sukhov, Juan Jose Sáenz, Aristide Dogariu, “Near-Field Effects in Mesoscopic Light Transport”, Graduate Research Forum, UCF, 2016.

P4. Felix A. Tan, **Roxana Rezvani Naraghi**, Marielena Burdge, Sergey Sukhov, Aristide Dogariu, Ayman Abouraddy, “Diffusive Optical Scattering from TiO2/Polymer Composite Microspheres”, MRS, 2016.

P3. **Roxana Rezvani Naraghi**, Marielena Burdge and Aristide Dogariu. “Anomalous diffusion of light in complex media”, APS March Meeting, 2016.

P2. **Roxana Rezvani Naraghi,** Sergey Sukhov, Juan Jose Sáenz, Aristide Dogariu, “Near-Field Effects in Mesoscopic Light Transport”, CREOL Industrial Affiliates Symposium,2016.

P1. **Roxana Rezvani Naraghi**, S. Sukhov, G. Tao, J. J. Kaufmann, A. F. Abouraddy, A. Dogariu “Tuning Light with Photonic Particles”, Graduate Research Forum, UCF, 2015.

Patents

2. A. Abouraddy, A. Dogariu, J. Kaufman, **Roxana Rezvani Naraghi**, S. Sukhov, F. Tan, “Structured Granular Composite Materials, Method of Fabrication, and Applications,” US Patent 20,160,139,305

1. Aristide Dogariu, **Roxana Rezvani Naraghi**, Sergey Sukhov. “Plate Type Concentrator with High Light Guiding Efficiency,” Patent Pending 01/23/2015 62/106,893

LIST OF REFERENCES

1. E. Akkermans and G. Montambaux, *Mesoscopic Physics of Electrons and Photons* (Cambridge University Press, 2007).

2. P. Sheng, *Introduction to Wave Scattering, Localization and Mesoscopic Phenomena* (Springer Science & Business Media, 2006).

3. "More Is Different," in *A Career in Theoretical Physics*, World Scientific Series in 20th Century Physics No. Volume 7 (WORLD SCIENTIFIC, 1994), Vol. Volume 7, pp. 1–4.

4. F. Monticone and A. Alù, "Metamaterial, plasmonic and nanophotonic devices," Rep. Prog. Phys. **80**, 036401 (2017).

5. Y. Liu and X. Zhang, "Metamaterials: a new frontier of science and technology," Chem. Soc. Rev. **40**, 2494–2507 (2011).

6. D. M. Herlach, I. Klassen, P. Wette, and D. Holland-Moritz, "Colloids as model systems for metals and alloys: a case study of crystallization," J. Phys. Condens. Matter **22**, 153101 (2010).

7. G. A. Ozin and S. M. Yang, "The Race for the Photonic Chip: Colloidal Crystal Assembly in Silicon Wafers," Adv. Funct. Mater. **11**, 95–104 (2001).

8. A. Ishimaru, *Wave Propagation and Scattering in Random Media. Volume I - Single Scattering and Transport Theory* (1978).

9. J. W. Goodman, *Statistical Optics*, 1 edition (Wiley-Interscience, 2000).

10. E. Akkermans, P. E. Wolf, R. Maynard, and G. Maret, "Theoretical study of the coherent backscattering of light by disordered media," J. Phys. **49**, 77–98 (1988).

11. E. Akkermans, P. E. Wolf, and R. Maynard, "Coherent Backscattering of Light by Disordered Media: Analysis of the Peak Line Shape," Phys. Rev. Lett. **56**, 1471–1474 (1986).

12. J. W. Goodman, *Speckle Phenomena in Optics: Theory and Applications* (Roberts and Company Publishers, 2007).

13. B. J. Berne and R. Pecora, *Dynamic Light Scattering: With Applications to Chemistry, Biology, and Physics* (Courier Corporation, 2000).

14. M. C. Marchetti, J. F. Joanny, S. Ramaswamy, T. B. Liverpool, J. Prost, M. Rao, and R. A. Simha, "Hydrodynamics of soft active matter," Rev. Mod. Phys. **85**, 1143–1189 (2013).

15. "The Mechanics and Statistics of Active Matter," Annu. Rev. Condens. Matter Phys. **1**, 323–345 (2010).

16. D. Barchiesi and D. V. Labeke, "Application of Mie Scattering of Evanescent Waves to Scanning Tunnelling Optical Microscopy Theory," J. Mod. Opt. **40**, 1239–1254 (1993).

17. S. Chandrasekhar, *Radiative Transfer* (Courier Corporation, 2013).

18. O. S. of America, *Handbook of Optics* (McGraw Hill Professional, 2000).

19. V. K. Varadan and V. V. Varadan, "Acoustic, electromagnetic and elastic wave scattering - Focus on the T-matrix approach; Proceedings of the International Symposium, Ohio State University, Columbus, Ohio, June 25-27, 1979," in (1980).

20. D. W. Mackowski and M. I. Mishchenko, "Direct simulation of multiple scattering by discrete random media illuminated by Gaussian beams," Phys. Rev. A **83**, 013804 (2011).

21. R. R. Naraghi, S. Sukhov, and A. Dogariu, "Near Field Measurements of the Scattering Phase Function with Evanescent Field Excitation," in *CLEO: 2015 (2015), Paper JTu5A.77* (Optical Society of America, 2015), p. JTu5A.77.

22. R. Rezvani Naraghi, S. Sukhov, J. J. Sáenz, and A. Dogariu, "Near-Field Effects in Mesoscopic Light Transport," Phys. Rev. Lett. **115**, 203903 (2015).

23. R. R. Naraghi, S. Sukhov, and A. Dogariu, "Near-field Corrections in Mesoscopic Transport," in *Frontiers in Optics 2015 (2015), Paper LTh2H.3* (Optical Society of America, 2015), p. LTh2H.3.

24. R. R. Naraghi, M. Burdge, S. Sukhov, and A. Dogariu, "Near-field interactions and anomalous diffusion of light in disordered media," in *Conference on Lasers and Electro-Optics (2016), Paper FW4D.4* (Optical Society of America, 2016), p. FW4D.4.

25. R. Rezvani Naraghi and A. Dogariu, "Phase Transitions in Diffusion of Light," Phys. Rev. Lett. **117**, 263901 (2016).

26. R. Rezvani Naraghi, M. Burdge, and A. Dogariu, "Anomalous diffusion of light in complex media," in (2016).

27. R. Rezvani Naraghi, S. Sukhov, J. J. Sáenz, and A. Dogariu, "Light transport in dense composite media: role of near-field coupling," in (2016).

28. C. F. Bohren and D. R. Huffman, *Absorption and Scattering of Light by Small Particles* (John Wiley & Sons, 2008).

29. A. H. Gandjbakhche and G. H. Weiss, "V: Random Walk and Diffusion-Like Models of Photon Migration in Turbid Media," in *Progress in Optics*, E. Wolf, ed. (Elsevier, 1995), Vol. 34, pp. 333–402.

30. E. P. Wigner, "Lower Limit for the Energy Derivative of the Scattering Phase Shift," Phys. Rev. **98**, 145–147 (1955).

31. G. Cwilich and Y. Fu, "Scattering delay and renormalization of the wave-diffusion constant," Phys. Rev. B **46**, 12015–12018 (1992).

32. P. M. Saulnier, M. P. Zinkin, and G. H. Watson, "Scatterer correlation effects on photon transport in dense random media," Phys. Rev. B **42**, 2621–2623 (1990).

33. S. Fraden and G. Maret, "Multiple light scattering from concentrated, interacting suspensions," Phys. Rev. Lett. **65**, 512–515 (1990).

34. J. M. Ziman, "A theory of the electrical properties of liquid metals. I: The monovalent metals," Philos. Mag. **6**, 1013–1034 (1961).

35. N. W. Ashcroft and J. Lekner, "Structure and Resistivity of Liquid Metals," Phys. Rev. **145**, 83–90 (1966).

36. R. W. Hart and R. A. Farrell, "Light Scattering in the Cornea*," JOSA **59**, 766–774 (1969).

37. G. B. Benedek, "Theory of Transparency of the Eye," Appl. Opt. **10**, 459–473 (1971).

38. L. F. Rojas-Ochoa, J. M. Mendez-Alcaraz, J. J. Sáenz, P. Schurtenberger, and F. Scheffold, "Photonic Properties of Strongly Correlated Colloidal Liquids," Phys. Rev. Lett. **93**, 073903 (2004).

39. M. Reufer, L. F. Rojas-Ochoa, S. Eiden, J. J. Sáenz, and Scheffold, "Transport of light in amorphous photonic materials," Appl. Phys. Lett. **91**, 171904 (2007).

40. P. D. García, R. Sapienza, Á. Blanco, and C. López, "Photonic Glass: A Novel Random Material for Light," Adv. Mater. **19**, 2597–2602 (2007).

41. R. O. Prum, R. H. Torres, S. Williamson, and J. Dyck, "Coherent light scattering by blue feather barbs," Nature **396**, 28–29 (1998).

42. S. F. Liew, J. Forster, H. Noh, C. F. Schreck, V. Saranathan, X. Lu, L. Yang, R. O. Prum, C. S. O'Hern, E. R. Dufresne, and H. Cao, "Short-range order and near-field

effects on optical scattering and structural coloration," Opt. Express **19**, 8208–8217 (2011).

43. L. Cortese, L. Pattelli, F. Utel, S. Vignolini, M. Burresi, and D. S. Wiersma, "Anisotropic Light Transport in White Beetle Scales," Adv. Opt. Mater. **3**, 1337–1341 (2015).

44. P. Sheng, "Theory for the Dielectric Function of Granular Composite Media," Phys. Rev. Lett. **45**, 60–63 (1980).

45. K. Busch and C. M. Soukoulis, "Transport Properties of Random Media: A New Effective Medium Theory," Phys. Rev. Lett. **75**, 3442–3445 (1995).

46. X. T. Peng and A. D. Dinsmore, "Light Propagation in Strongly Scattering, Random Colloidal Films: The Role of the Packing Geometry," Phys. Rev. Lett. **99**, 143902 (2007).

47. R. Sapienza, P. D. García, J. Bertolotti, M. D. Martín, Á. Blanco, L. Viña, C. López, and D. S. Wiersma, "Observation of Resonant Behavior in the Energy Velocity of Diffused Light," Phys. Rev. Lett. **99**, 233902 (2007).

48. P. D. García, R. Sapienza, J. Bertolotti, M. D. Martín, Á. Blanco, A. Altube, L. Viña, D. S. Wiersma, and C. López, "Resonant light transport through Mie modes in photonic glasses," Phys. Rev. A **78**, 023823 (2008).

49. V. N. Astratov and S. P. Ashili, "Percolation of light through whispering gallery modes in 3D lattices of coupled microspheres," Opt. Express **15**, 17351–17361 (2007).

50. S. Kirkpatrick, "Percolation and Conduction," Rev. Mod. Phys. **45**, 574–588 (1973).

51. Y. P. Mamunya, V. V. Davydenko, P. Pissis, and E. V. Lebedev, "Electrical and thermal conductivity of polymers filled with metal powders," Eur. Polym. J. **38**, 1887–1897 (2002).

52. H. Chew, D.-S. Wang, and M. Kerker, "Elastic scattering of evanescent electromagnetic waves," Appl. Opt. **18**, 2679–2687 (1979).

53. C. Liu, T. Kaiser, S. Lange, and G. Schweiger, "Structural resonances in a dielectric sphere illuminated by an evanescent wave," Opt. Commun. **117**, 521–531 (1995).

54. A. Y. Bekshaev, K. Y. Bliokh, and F. Nori, "Mie scattering and optical forces from evanescent fields: A complex-angle approach," Opt. Express **21**, 7082–7095 (2013).

55. S. Torquato, "Nearest-neighbor statistics for packings of hard spheres and disks," Phys. Rev. E **51**, 3170–3182 (1995).

56. J. X. Zhu, D. J. Pine, and D. A. Weitz, "Internal reflection of diffusive light in random media," Phys. Rev. A **44**, 3948–3959 (1991).

57. G. Popescu, C. Mujat, and A. Dogariu, "Evidence of scattering anisotropy effects on boundary conditions of the diffusion equation," Phys. Rev. E **61**, 4523–4529 (2000).

58. P. N. Pusey and W. van Megen, "Observation of a glass transition in suspensions of spherical colloidal particles," Phys. Rev. Lett. **59**, 2083–2086 (1987).

59. N. M. Dixit and C. F. Zukoski, "Kinetics of crystallization in hard-sphere colloidal suspensions," Phys. Rev. E **64**, 041604 (2001).

60. A. Ishimaru, "Diffusion of light in turbid material," Appl. Opt. **28**, 2210–2215 (1989).

61. P. Sheng, *Scattering and Localization of Classical Waves in Random Media* (World Scientific, 1990).

62. S. John, "Localization and absorption of waves in a weakly dissipative disordered medium," Phys. Rev. B **31**, 304–309 (1985).

63. S. E. Skipetrov and I. M. Sokolov, "Absence of Anderson Localization of Light in a Random Ensemble of Point Scatterers," Phys. Rev. Lett. **112**, 023905 (2014).

64. N. Cherroret, D. Delande, and B. A. van Tiggelen, "Induced dipole-dipole interactions in light diffusion from point dipoles," Phys. Rev. A **94**, 012702 (2016).

65. M. D. Birowosuto, S. E. Skipetrov, W. L. Vos, and A. P. Mosk, "Observation of Spatial Fluctuations of the Local Density of States in Random Photonic Media," Phys. Rev. Lett. **105**, 013904 (2010).

66. V. Krachmalnicoff, E. Castanié, Y. De Wilde, and R. Carminati, "Fluctuations of the Local Density of States Probe Localized Surface Plasmons on Disordered Metal Films," Phys. Rev. Lett. **105**, 183901 (2010).

67. E. Amic, J. M. Luck, and T. M. Nieuwenhuizen, "Anisotropic multiple scattering in diffusive media," J. Phys. Math. Gen. **29**, 4915 (1996).

68. M. Xu, W. Cai, M. Lax, and R. R. Alfano, "Photon migration in turbid media using a cumulant approximation to radiative transfer," Phys. Rev. E **65**, 066609 (2002).

69. K. M. Yoo, F. Liu, and R. R. Alfano, "When does the diffusion approximation fail to describe photon transport in random media?," Phys. Rev. Lett. **64**, 2647–2650 (1990).

70. R. Elaloufi, R. Carminati, and J.-J. Greffet, "Diffusive-to-ballistic transition in dynamic light transmission through thin scattering slabs: a radiative transfer approach," JOSA A **21**, 1430–1437 (2004).

71. A. Yaroshevsky, Z. Glasser, E. Granot, and S. Sternklar, "Transition from the ballistic to the diffusive regime in a turbid medium," Opt. Lett. **36**, 1395–1397 (2011).

72. M. C. W. van Rossum and T. M. Nieuwenhuizen, "Multiple scattering of classical waves: microscopy, mesoscopy, and diffusion," Rev. Mod. Phys. **71**, 313–371 (1999).

73. M. S. Patterson, B. Chance, and B. C. Wilson, "Time resolved reflectance and transmittance for the noninvasive measurement of tissue optical properties," Appl. Opt. **28**, 2331–2336 (1989).

74. H. Cao, Y. G. Zhao, S. T. Ho, E. W. Seelig, Q. H. Wang, and R. P. H. Chang, "Random Laser Action in Semiconductor Powder," Phys. Rev. Lett. **82**, 2278–2281 (1999).

75. A. G. Yodh, B. Chance, D. A. Boas, and M. O'Leary, "Object imaging using diffuse light," U.S. patent US5917190 A (June 29, 1999).

76. X. Cheng, X. Xu, S. Zhou, L. Wang, M. Wang, F. Li, and G. Hu, "Self-calibrating optical imaging system," U.S. patent US6516209 B2 (February 4, 2003).

77. J. Ripoll and V. Ntziachristos, "From Finite to Infinite Volumes: Removal of Boundaries in Diffuse Wave Imaging," Phys. Rev. Lett. **96**, 173903 (2006).

78. V. Ntziachristos, J. Ripoll, L. V. Wang, and R. Weissleder, "Looking and listening to light: the evolution of whole-body photonic imaging," Nat. Biotechnol. **23**, 313–320 (2005).

79. T. Durduran, R. Choe, W. B. Baker, and A. G. Yodh, "Diffuse optics for tissue monitoring and tomography," Rep. Prog. Phys. **73**, 076701 (2010).

80. M. Störzer, P. Gross, C. M. Aegerter, and G. Maret, "Observation of the Critical Regime Near Anderson Localization of Light," Phys. Rev. Lett. **96**, 063904 (2006).

81. D. S. Wiersma, M. P. van Albada, B. A. van Tiggelen, and A. Lagendijk, "Experimental Evidence for Recurrent Multiple Scattering Events of Light in Disordered Media," Phys. Rev. Lett. **74**, 4193–4196 (1995).

82. A. Aubry, L. A. Cobus, S. E. Skipetrov, B. A. van Tiggelen, A. Derode, and J. H. Page, "Recurrent Scattering and Memory Effect at the Anderson Localization Transition," Phys. Rev. Lett. **112**, 043903 (2014).

83. P. Barthelemy, J. Bertolotti, and D. S. Wiersma, "A Lévy flight for light," Nature **453**, 495–498 (2008).

84. M. P. van Albada, B. A. van Tiggelen, A. Lagendijk, and A. Tip, "Speed of propagation of classical waves in strongly scattering media," Phys. Rev. Lett. **66**, 3132–3135 (1991).

85. P. W. Anderson, "The question of classical localization A theory of white paint?," Philos. Mag. Part B **52**, 505–509 (1985).

86. S. John, "Electromagnetic Absorption in a Disordered Medium near a Photon Mobility Edge," Phys. Rev. Lett. **53**, 2169–2172 (1984).

87. K. M. Douglass, S. John, T. Suezaki, G. A. Ozin, and A. Dogariu, "Anomalous flow of light near a photonic crystal pseudo-gap," Opt. Express **19**, 25320–25327 (2011).

88. T. Sperling, L. Schertel, M. Ackermann, G. J. Aubry, C. M. Aegerter, and G. Maret, "Can 3D light localization be reached in “white paint”?," New J. Phys. **18**, 013039 (2016).

89. L. F. Cugliandolo, "The effective temperature," J. Phys. Math. Theor. **44**, 483001 (2011).

90. G. Popescu and A. Dogariu, "Optical path-length spectroscopy of wave propagation in random media," Opt. Lett. **24**, 442–444 (1999).

91. E. Akkermans and G. Montambaux, "Mesoscopic physics of photons," JOSA B **21**, 101–112 (2004).

92. R. Zwanzig, "Diffusion in a rough potential," Proc. Natl. Acad. Sci. **85**, 2029–2030 (1988).

93. M. A. Despósito, "Superdiffusion induced by a long-correlated external random force," Phys. Rev. E **84**, 061114 (2011).

94. P. Tierno, F. Sagués, T. H. Johansen, and I. M. Sokolov, "Antipersistent Random Walk in a Two State Flashing Magnetic Potential," Phys. Rev. Lett. **109**, 070601 (2012).

95. R. D. L. Hanes, M. Schmiedeberg, and S. U. Egelhaaf, "Brownian particles on rough substrates: Relation between intermediate subdiffusion and asymptotic long-time diffusion," Phys. Rev. E **88**, 062133 (2013).

96. A. H. Romero and J. M. Sancho, "Brownian motion in short range random potentials," Phys. Rev. E **58**, 2833–2837 (1998).

97. F. Jendrzejewski, A. Bernard, K. Müller, P. Cheinet, V. Josse, M. Piraud, L. Pezzé, L. Sanchez-Palencia, A. Aspect, and P. Bouyer, "Three-dimensional localization of ultracold atoms in an optical disordered potential," Nat. Phys. **8**, 398–403 (2012).

98. K. M. Douglass, S. Sukhov, and A. Dogariu, "Superdiffusion in optically controlled active media," Nat. Photonics **6**, 834–837 (2012).

99. R. M. Dickson, D. J. Norris, Y.-L. Tzeng, and W. E. Moerner, "Three-Dimensional Imaging of Single Molecules Solvated in Pores of Poly(acrylamide) Gels," Science **274**, 966–968 (1996).

100. J. R. Guzman-Sepulveda, J. Deng, J. Y. Fang, and A. Dogariu, "In situ characterization of structural dynamics in swelling hydrogels," Soft Matter **12**, 5986–5994 (2016).

101. M. Weiss, M. Elsner, F. Kartberg, and T. Nilsson, "Anomalous Subdiffusion Is a Measure for Cytoplasmic Crowding in Living Cells," Biophys. J. **87**, 3518–3524 (2004).

102. F. Höfling and T. Franosch, "Anomalous transport in the crowded world of biological cells," Rep. Prog. Phys. **76**, 046602 (2013).

103. J. R. Guzman-Sepulveda, R. Argueta-Morales, W. M. DeCampli, and A. Dogariu, "Real-time intraoperative monitoring of blood coagulability via coherence-gated light scattering," Nat. Biomed. Eng. **1**, 0028 (2017).

104. N. Cherroret, T. Karpiuk, B. Grémaud, and C. Miniatura, "Thermalization of matter waves in speckle potentials," Phys. Rev. A **92**, 063614 (2015).

105. S. E. Skipetrov and J. H. Page, "Red light for Anderson localization," New J. Phys. **18**, 021001 (2016).

106. H. C. van de Hulst, *Light Scattering by Small Particles* (Courier Corporation, 2012).

107. M. Kerker, *The Scattering of Light: And Other Electromagnetic Radiation* (1969).

108. R. Xu, *Particle Characterization: Light Scattering Methods* (Springer Science & Business Media, 2001).

109. G. Mie, *Contributions to the Optics of Turbid Media, Particularly of Colloidal Metal Solutions* (1976).

110. E. Hecht, *Optics*, 4 edition (Addison-Wesley, 2001).

111. R. R. Naraghi, S. Sukhov, and A. Dogariu, "Directional control of scattering by all-dielectric core-shell spheres," Opt. Lett. **40**, 585–588 (2015).

112. R. R. Naraghi, S. Sukhov, and A. Dogariu, "Designing All-Dielectric Structures for Efficient Directional Scattering," in *Frontiers in Optics 2015 (2015), Paper FTh4F.6* (Optical Society of America, 2015), p. FTh4F.6.

113. R. R. Naraghi, G. Tao, J. J. Kaufmann, S. Shabahang, S. Sukhov, A. Abouraddy, and A. Dogariu, "Tuning Light with Photonic Particles," in *Conference on Lasers and Electro-Optics (2016), Paper SM1R.2* (Optical Society of America, 2016), p. SM1R.2.

114. F. Tan, R. R. Naraghi, S. Sukhov, A. Dogariu, and A. Abouraddy, "Diffusive Scattering from a Single Composite Microsphere Fabricated by an In-Fiber Fluid Instability," in *Photonics and Fiber Technology 2016 (ACOFT, BGPP, NP) (2016), Paper AW3C.3* (Optical Society of America, 2016), p. AW3C.3.

115. F. Tan, R. R. Naraghi, M. Burdge, A. Dogariu, and A. Abouraddy, "Diffusive Scattering from Single Microspheres with Well-Dispersed Dielectric Nano-Scale Inclusions," in *Conference on Lasers and Electro-Optics (2016), Paper JW2A.25* (Optical Society of America, 2016), p. JW2A.25.

116. A. Abouraddy, A. Dogariu, J. Kaufman, R. R. Naraghi, S. Sukhov, and F. Tan, "Structured granular composite materials, methods of fabrication thereof and applications thereof," U.S. patent US20160139305 A1 (May 19, 2016).

117. R. P. Feynman, R. B. Leighton, and M. Sands, *The Feynman Lectures on Physics: The New Millennium Edition: Mainly Mechanics, Radiation, and Heat* (Basic Books, 2015).

118. M. Kerker, D.-S. Wang, and C. L. Giles, "Electromagnetic scattering by magnetic spheres," JOSA **73**, 765–767 (1983).

119. M. Nieto-Vesperinas, R. Gomez-Medina, and J. J. Saenz, "Angle-suppressed scattering and optical forces on submicrometer dielectric particles," JOSA A **28**, 54–60 (2011).

120. R. Gómez-Medina, B. García-Cámara, I. Suárez-Lacalle, F. González, F. Moreno, M. Nieto-Vesperinas, and J. J. Sáenz, "Electric and magnetic dipolar response of germanium nanospheres: interference effects, scattering anisotropy, and optical forces," J. Nanophotonics **5**, 053512-053512-9 (2011).

121. A. García-Etxarri, R. Gómez-Medina, L. S. Froufe-Pérez, C. López, L. Chantada, F. Scheffold, J. Aizpurua, M. Nieto-Vesperinas, and J. J. Sáenz, "Strong magnetic response of submicron Silicon particles in the infrared," Opt. Express **19**, 4815–4826 (2011).

122. W. Liu, A. E. Miroshnichenko, D. N. Neshev, and Y. S. Kivshar, "Broadband Unidirectional Scattering by Magneto-Electric Core–Shell Nanoparticles," ACS Nano **6**, 5489–5497 (2012).

123. R. Gómez-Medina, B. García-Cámara, I. Suárez-Lacalle, L. S. Froufe-Pérez, F. González, F. Moreno, M. Nieto-Vesperinas, and J. J. Sáenz, "Electric and magnetic

optical response of dielectric nanospheres: Optical forces and scattering anisotropy," Photonics Nanostructures - Fundam. Appl. **10**, 345–352 (2012).

124. R. Gómez-Medina, L. S. Froufe-Pérez, M. Yépez, F. Scheffold, M. Nieto-Vesperinas, and J. J. Sáenz, "Negative scattering asymmetry parameter for dipolar particles: Unusual reduction of the transport mean free path and radiation pressure," Phys. Rev. A **85**, 035802 (2012).

125. S. D. Campbell and R. W. Ziolkowski, "Simultaneous Excitation of Electric and Magnetic Dipole Modes in a Resonant Core-Shell Particle at Infrared Frequencies to Achieve Minimal Backscattering," IEEE J. Sel. Top. Quantum Electron. **19**, 4700209–4700209 (2013).

126. W. Liu, J. Zhang, B. Lei, H. Ma, W. Xie, and H. Hu, "Ultra-directional forward scattering by individual core-shell nanoparticles," Opt. Express **22**, 16178–16187 (2014).

127. M. T. Tavassoly, R. R. Naraghi, A. Nahal, and K. Hassani, "High precision refractometry based on Fresnel diffraction from phase plates," Opt. Lett. **37**, 1493–1495 (2012).

128. Y. H. Fu, A. I. Kuznetsov, A. E. Miroshnichenko, Y. F. Yu, and B. Luk'yanchuk, "Directional visible light scattering by silicon nanoparticles," Nat. Commun. **4**, 1527 (2013).

129. J. M. Geffrin, B. García-Cámara, R. Gómez-Medina, P. Albella, L. S. Froufe-Pérez, C. Eyraud, A. Litman, R. Vaillon, F. González, M. Nieto-Vesperinas, J. J. Sáenz, and F. Moreno, "Magnetic and electric coherence in forward- and back-scattered electromagnetic waves by a single dielectric subwavelength sphere," Nat. Commun. **3**, 1171 (2012).

130. S. Person, M. Jain, Z. Lapin, J. J. Sáenz, G. Wicks, and L. Novotny, "Demonstration of Zero Optical Backscattering from Single Nanoparticles," Nano Lett. **13**, 1806–1809 (2013).

131. A. B. Evlyukhin, S. M. Novikov, U. Zywietz, R. L. Eriksen, C. Reinhardt, S. I. Bozhevolnyi, and B. N. Chichkov, "Demonstration of Magnetic Dipole Resonances of Dielectric Nanospheres in the Visible Region," Nano Lett. **12**, 3749–3755 (2012).

132. B. Rolly, B. Stout, and N. Bonod, "Boosting the directivity of optical antennas with magnetic and electric dipolar resonant particles," Opt. Express **20**, 20376–20386 (2012).

133. M. C. Ohmer, "Design of three-layer equivalent films," JOSA **68**, 137–139 (1978).

134. D. D. Smith, H. Chang, and K. A. Fuller, "Whispering-gallery mode splitting in coupled microresonators," JOSA B **20**, 1967–1974 (2003).

135. D. D. Smith, H. Chang, K. A. Fuller, A. T. Rosenberger, and R. W. Boyd, "Coupled-resonator-induced transparency," Phys. Rev. A **69**, 063804 (2004).

136. J. J. Kaufman, G. Tao, S. Shabahang, E.-H. Banaei, D. S. Deng, X. Liang, S. G. Johnson, Y. Fink, and A. F. Abouraddy, "Structured spheres generated by an in-fibre fluid instability," Nature **487**, 463–467 (2012).

137. I. K. Ludlow and J. Everitt, "Inverse Mie problem," JOSA A **17**, 2229–2235 (2000).

138. M. Bass, C. DeCusatis, J. Enoch, V. Lakshminarayanan, G. Li, C. MacDonald, V. Mahajan, and E. V. Stryland, *Handbook of Optics, Third Edition Volume IV: Optical Properties of Materials, Nonlinear Optics, Quantum Optics*, 3 edition (McGraw-Hill Education, 2009).

139. S. Shabahang, J. J. Kaufman, D. S. Deng, and A. F. Abouraddy, "Observation of the Plateau-Rayleigh capillary instability in multi-material optical fibers," Appl. Phys. Lett. **99**, 161909 (2011).

140. J. J. Kaufman, R. Ottman, G. Tao, S. Shabahang, E.-H. Banaei, X. Liang, S. G. Johnson, Y. Fink, R. Chakrabarti, and A. F. Abouraddy, "In-fiber production of polymeric particles for biosensing and encapsulation," Proc. Natl. Acad. Sci. **110**, 15549–15554 (2013).

141. A. F. Abouraddy, M. Bayindir, G. Benoit, S. D. Hart, K. Kuriki, N. Orf, O. Shapira, F. Sorin, B. Temelkuran, and Y. Fink, "Towards multimaterial multifunctional fibres that see, hear, sense and communicate," Nat. Mater. **6**, 336–347 (2007).

142. G. Tao, A. M. Stolyarov, and A. F. Abouraddy, "Multimaterial Fibers," Int. J. Appl. Glass Sci. **3**, 349–368 (2012).

143. G. Tao, H. Ebendorff-Heidepriem, A. M. Stolyarov, S. Danto, J. V. Badding, Y. Fink, J. Ballato, and A. F. Abouraddy, "Infrared fibers," Adv. Opt. Photonics **7**, 379–458 (2015).

144. Lord Rayleigh, "On the Capillary Phenomena of Jets," Proc. R. Soc. Lond. **29**, 71–97 (1879).

145. J. Eggers and E. Villermaux, "Physics of liquid jets," Rep. Prog. Phys. **71**, 036601 (2008).

146. J. Lee, P. W. Bisso, R. L. Srinivas, J. J. Kim, A. J. Swiston, and P. S. Doyle, "Universal process-inert encoding architecture for polymer microparticles," Nat. Mater. **13**, 524–529 (2014).

147. S. C. Glotzer and M. J. Solomon, "Anisotropy of building blocks and their assembly into complex structures," Nat. Mater. **6**, 557–562 (2007).

148. J. Yan, M. Bloom, S. C. Bae, E. Luijten, and S. Granick, "Linking synchronization to self-assembly using magnetic Janus colloids," Nature **491**, 578–581 (2012).

149. A. Walther and A. H. E. Müller, "Janus Particles: Synthesis, Self-Assembly, Physical Properties, and Applications," Chem. Rev. **113**, 5194–5261 (2013).

150. G. Tao, J. J. Kaufman, S. Shabahang, R. R. Naraghi, S. V. Sukhov, J. D. Joannopoulos, Y. Fink, A. Dogariu, and A. F. Abouraddy, "Digital design of multimaterial photonic particles," Proc. Natl. Acad. Sci. **113**, 6839–6844 (2016).

151. C. Brosseau and D. Bicout, "Entropy production in multiple scattering of light by a spatially random medium," Phys. Rev. E **50**, 4997–5005 (1994).

152. "Wiley: Fundamentals of Polarized Light: A Statistical Optics Approach - Christian Brosseau," http://www.wiley.com/WileyCDA/WileyTitle/productCd-0471143022.html.

153. S. Zhang, B. Hu, P. Sebbah, and A. Z. Genack, "Speckle Evolution of Diffusive and Localized Waves," Phys. Rev. Lett. **99**, 063902 (2007).

154. J. Broky, J. Ellis, and A. Dogariu, "Identifying non-stationarities in random EM fields: are speckles really disturbing?," Opt. Express **16**, 14469–14475 (2008).

155. J. Broky, K. M. Douglass, J. Ellis, and A. Dogariu, "Fluctuations of scattered waves: going beyond the ensemble average," Opt. Express **17**, 10466–10471 (2009).

156. S. M. Cohen, D. Eliyahu, I. Freund, and M. Kaveh, "Vector statistics of multiply scattered waves in random systems," Phys. Rev. A **43**, 5748–5751 (1991).

157. D. Bicout, C. Brosseau, A. S. Martinez, and J. M. Schmitt, "Depolarization of multiply scattered waves by spherical diffusers: Influence of the size parameter," Phys. Rev. E **49**, 1767–1770 (1994).

158. A. Dogariu, C. Kutsche, P. Likamwa, G. Boreman, and B. Moudgil, "Time-domain depolarization of waves retroreflected from dense colloidal media," Opt. Lett. **22**, 585–587 (1997).

159. L. F. Rojas-Ochoa, D. Lacoste, R. Lenke, P. Schurtenberger, and F. Scheffold, "Depolarization of backscattered linearly polarized light," JOSA A **21**, 1799–1804 (2004).

160. M. Mujat and A. C. Dogariu, "Real-time Mueller matrix measurement for particulate systems," in (2000), Vol. 4035, pp. 390–400.

161. M. Mujat, A. Spier, and A. Dogariu, "Polarimetric signature of dense scattering media," in (2003), Vol. 5158, pp. 217–225.

162. R. R. Naraghi, S. Sukhov, and A. Dogariu, "Disorder fingerprint: Intensity distributions in the near field of random media," Phys. Rev. B **94**, 174205 (2016).

163. R. R. Naraghi, S. Sukhov, and A. Dogariu, "Disorder fingerprint - the distribution of local density of states in random media," in *Conference on Lasers and Electro-Optics (2016), Paper FM3D.1* (Optical Society of America, 2016), p. FM3D.1.

164. R. R. Naraghi, S. Sukhov, and A. Dogariu, "Near-Field Intensity Fluctuations: the Role of Disorder Correlations," in *Frontiers in Optics 2015 (2015), Paper LTh1H.6* (Optical Society of America, 2015), p. LTh1H.6.

165. E. Jakeman and R. J. A. Tough, "Non-Gaussian models for the statistics of scattered waves," Adv. Phys. **37**, 471–529 (1988).

166. M. Nieto-Vesperinas and J. A. Sánchez-Gil, "Second-order statistics of non-Gaussian fluctuations of coherent waves reflected from disordered media," Phys. Rev. B **48**, 4132–4135 (1993).

167. A. Apostol and A. Dogariu, "Non-Gaussian statistics of optical near-fields," Phys. Rev. E **72**, 025602 (2005).

168. A. Apostol, D. Haefner, and A. Dogariu, "Near-field characterization of effective optical interfaces," Phys. Rev. E **74**, 066603 (2006).

169. E. Kogan, M. Kaveh, R. Baumgartner, and R. Berkovits, "Statistics of waves propagating in a random medium," Phys. Rev. B **48**, 9404–9410 (1993).

170. N. Garcia and A. Z. Genack, "Crossover to strong intensity correlation for microwave radiation in random media," Phys. Rev. Lett. **63**, 1678–1681 (1989).

171. T. M. Nieuwenhuizen and M. C. W. van Rossum, "Intensity Distributions of Waves Transmitted through a Multiple Scattering Medium," Phys. Rev. Lett. **74**, 2674–2677 (1995).

172. M. T. Tavassoly, S. R. Hosseini, A. M. Fard, and R. R. Naraghi, "Applications of Fresnel diffraction from the edge of a transparent plate in transmission," Appl. Opt. **51**, 7170–7175 (2012).

173. Y. Bromberg and H. Cao, "Generating Non-Rayleigh Speckles with Tailored Intensity Statistics," Phys. Rev. Lett. **112**, 213904 (2014).

174. F. Riboli, N. Caselli, S. Vignolini, F. Intonti, K. Vynck, P. Barthelemy, A. Gerardino, L. Balet, L. H. Li, A. Fiore, M. Gurioli, and D. S. Wiersma, "Engineering of light confinement in strongly scattering disordered media," Nat. Mater. **13**, 720–725 (2014).

175. N. Shnerb and M. Kaveh, "Non-Rayleigh statistics of waves in random systems," Phys. Rev. B **43**, 1279–1282 (1991).

176. V. Coello and S. I. Bozhevolnyi, "Experimental statistics of near-field intensity distributions at nanostructured surfaces," J. Microsc. **202**, 136–141 (2001).

177. B. A. van Tiggelen and S. E. Skipetrov, "Fluctuations of local density of states and ${C}_{0}$ speckle correlations are equal," Phys. Rev. E **73**, 045601 (2006).

178. A. Cazé, R. Pierrat, and R. Carminati, "Near-field interactions and nonuniversality in speckle patterns produced by a point source in a disordered medium," Phys. Rev. A **82**, 043823 (2010).

179. M. A. Miller and D. Frenkel, "Phase diagram of the adhesive hard sphere fluid," J. Chem. Phys. **121**, 535–545 (2004).

180. A. Beghdadi, C. Andraud, J. Lafait, J. Peiro, and M. Perreau, "Entropic and multifractal analysis of disordered morphologies," Fractals **01**, 671–679 (1993).

181. C. Andraud, A. Beghdadi, E. Haslund, R. Hilfer, J. Lafait, and B. Virgin, "Local entropy characterization of correlated random microstructures," Phys. Stat. Mech. Its Appl. **235**, 307–318 (1997).

182. B. le Feber, N. Rotenberg, D. M. Beggs, and L. Kuipers, "Simultaneous measurement of nanoscale electric and magnetic optical fields," Nat. Photonics **8**, 43–46 (2014).

183. C. Chicanne, T. David, R. Quidant, J. C. Weeber, Y. Lacroute, E. Bourillot, A. Dereux, G. Colas des Francs, and C. Girard, "Imaging the Local Density of States of Optical Corrals," Phys. Rev. Lett. **88**, 097402 (2002).

184. D. C. Kohlgraf-Owens, S. Sukhov, and A. Dogariu, "Discrimination of field components in optical probe microscopy," Opt. Lett. **37**, 3606–3608 (2012).

185. I. V. Kabakova, A. de Hoogh, R. E. C. van der Wel, M. Wulf, B. le Feber, and L. Kuipers, "Imaging of electric and magnetic fields near plasmonic nanowires," Sci. Rep. **6**, 22665 (2016).

186. V. Parigi, E. Perros, G. Binard, C. Bourdillon, A. Maître, R. Carminati, V. Krachmalnicoff, and Y. D. Wilde, "Near-field to far-field characterization of speckle patterns generated by disordered nanomaterials," Opt. Express **24**, 7019–7027 (2016).

187. A. Apostol and A. Dogariu, "Spatial Correlations in the Near Field of Random Media," Phys. Rev. Lett. **91**, 093901 (2003).

188. A. Apostol and A. Dogariu, "First- and second-order statistics of optical near fields," Opt. Lett. **29**, 235–237 (2004).

189. M. Burresi, R. J. P. Engelen, A. Opheij, D. van Oosten, D. Mori, T. Baba, and L. Kuipers, "Observation of Polarization Singularities at the Nanoscale," Phys. Rev. Lett. **102**, 033902 (2009).

190. D. A. Keen and A. L. Goodwin, "The crystallography of correlated disorder," Nature **521**, 303–309 (2015).

191. W. H. Carter and E. Wolf, "Coherence properties of lambertian and non-lambertian sources*," JOSA **65**, 1067–1071 (1975).

192. A. Dogariu and R. Carminati, "Electromagnetic field correlations in three-dimensional speckles," Phys. Rep. **559**, 1–29 (2015).

193. C. Henkel, K. Joulain, R. Carminati, and J.-J. Greffet, "Spatial coherence of thermal near fields," Opt. Commun. **186**, 57–67 (2000).

194. H. Roychowdhury and E. Wolf, "Effects of spatial coherence on near-field spectra," Opt. Lett. **28**, 170–172 (2003).

195. R. Carminati, "Subwavelength spatial correlations in near-field speckle patterns," Phys. Rev. A **81**, 053804 (2010).

196. A. Apostol and A. Dogariu, "Coherence properties near interfaces of random media," Phys. Rev. E **67**, 055601 (2003).

197. L. Vicarelli, S. J. Heerema, C. Dekker, and H. W. Zandbergen, "Controlling Defects in Graphene for Optimizing the Electrical Properties of Graphene Nanodevices," ACS Nano **9**, 3428–3435 (2015).

198. W. Zhao, Y. Wang, Z. Wu, W. Wang, K. Bi, Z. Liang, J. Yang, Y. Chen, Z. Xu, and Z. Ni, "Defect-Engineered Heat Transport in Graphene: A Route to High Efficient Thermal Rectification," Sci. Rep. **5**, 11962 (2015).

199. J. C. W. Song, M. Y. Reizer, and L. S. Levitov, "Disorder-Assisted Electron-Phonon Scattering and Cooling Pathways in Graphene," Phys. Rev. Lett. **109**, 106602 (2012).

200. T. V. Alencar, M. G. Silva, L. M. Malard, and A. M. de Paula, "Defect-Induced Supercollision Cooling of Photoexcited Carriers in Graphene," Nano Lett. **14**, 5621–5624 (2014).

201. Q. Ma, N. M. Gabor, T. I. Andersen, N. L. Nair, K. Watanabe, T. Taniguchi, and P. Jarillo-Herrero, "Competing Channels for Hot-Electron Cooling in Graphene," Phys. Rev. Lett. **112**, 247401 (2014).

202. A. Stange, C. Sohrt, L. X. Yang, G. Rohde, K. Janssen, P. Hein, L.-P. Oloff, K. Hanff, K. Rossnagel, and M. Bauer, "Hot electron cooling in graphite: Supercollision versus hot phonon decay," Phys. Rev. B **92**, 184303 (2015).

203. F. Banhart, J. Kotakoski, and A. V. Krasheninnikov, "Structural Defects in Graphene," ACS Nano **5**, 26–41 (2011).

204. O. V. Yazyev and Y. P. Chen, "Polycrystalline graphene and other two-dimensional materials," Nat. Nanotechnol. **9**, 755–767 (2014).

205. Z.-J. Wang, G. Weinberg, Q. Zhang, T. Lunkenbein, A. Klein-Hoffmann, M. Kurnatowska, M. Plodinec, Q. Li, L. Chi, R. Schloegl, and M.-G. Willinger, "Direct Observation of Graphene Growth and Associated Copper Substrate Dynamics by in Situ Scanning Electron Microscopy," ACS Nano **9**, 1506–1519 (2015).

206. A. W. Robertson and J. H. Warner, "Atomic resolution imaging of graphene by transmission electron microscopy," Nanoscale **5**, 4079–4093 (2013).

207. G.-H. Lee, R. C. Cooper, S. J. An, S. Lee, A. van der Zande, N. Petrone, A. G. Hammerberg, C. Lee, B. Crawford, W. Oliver, J. W. Kysar, and J. Hone, "High-Strength Chemical-Vapor–Deposited Graphene and Grain Boundaries," Science **340**, 1073–1076 (2013).

208. G. López-Polín, C. Gómez-Navarro, V. Parente, F. Guinea, M. I. Katsnelson, F. Pérez-Murano, and J. Gómez-Herrero, "Increasing the elastic modulus of graphene by controlled defect creation," Nat. Phys. **11**, 26–31 (2015).

209. J. C. Koepke, J. D. Wood, D. Estrada, Z.-Y. Ong, K. T. He, E. Pop, and J. W. Lyding, "Atomic-Scale Evidence for Potential Barriers and Strong Carrier Scattering at Graphene Grain Boundaries: A Scanning Tunneling Microscopy Study," ACS Nano **7**, 75–86 (2013).

210. R. Beams, L. G. Cançado, and L. Novotny, "Raman characterization of defects and dopants in graphene," J. Phys. Condens. Matter **27**, 083002 (2015).

211. A. C. Ferrari and D. M. Basko, "Raman spectroscopy as a versatile tool for studying the properties of graphene," Nat. Nanotechnol. **8**, 235–246 (2013).

212. L. G. Cançado, A. Jorio, E. H. M. Ferreira, F. Stavale, C. A. Achete, R. B. Capaz, M. V. O. Moutinho, A. Lombardo, T. S. Kulmala, and A. C. Ferrari, "Quantifying Defects in Graphene via Raman Spectroscopy at Different Excitation Energies," Nano Lett. **11**, 3190–3196 (2011).

213. M. M. Lucchese, F. Stavale, E. H. M. Ferreira, C. Vilani, M. V. O. Moutinho, R. B. Capaz, C. A. Achete, and A. Jorio, "Quantifying ion-induced defects and Raman relaxation length in graphene," Carbon **48**, 1592–1597 (2010).

214. J. Ribeiro-Soares, M. E. Oliveros, C. Garin, M. V. David, L. G. P. Martins, C. A. Almeida, E. H. Martins-Ferreira, K. Takai, T. Enoki, R. Magalhães-Paniago, A. Malachias, A. Jorio, B. S. Archanjo, C. A. Achete, and L. G. Cançado, "Structural analysis of polycrystalline graphene systems by Raman spectroscopy," Carbon **95**, 646–652 (2015).

215. A. Eckmann, A. Felten, A. Mishchenko, L. Britnell, R. Krupke, K. S. Novoselov, and C. Casiraghi, "Probing the Nature of Defects in Graphene by Raman Spectroscopy," Nano Lett. **12**, 3925–3930 (2012).

216. Y. Huang, E. Sutter, N. N. Shi, J. Zheng, T. Yang, D. Englund, H.-J. Gao, and P. Sutter, "Reliable Exfoliation of Large-Area High-Quality Flakes of Graphene and Other Two-Dimensional Materials," ACS Nano **9**, 10612–10620 (2015).

217. M. C. Prado, D. Jariwala, T. J. Marks, and M. C. Hersam, "Optimization of graphene dry etching conditions via combined microscopic and spectroscopic analysis," Appl. Phys. Lett. **102**, 193111 (2013).

218. C. Casiraghi, A. Hartschuh, H. Qian, S. Piscanec, C. Georgi, A. Fasoli, K. S. Novoselov, D. M. Basko, and A. C. Ferrari, "Raman Spectroscopy of Graphene Edges," Nano Lett. **9**, 1433–1441 (2009).

219. R. Beams, L. G. Cançado, and L. Novotny, "Low Temperature Raman Study of the Electron Coherence Length near Graphene Edges," Nano Lett. **11**, 1177–1181 (2011).

220. D. W. Pohl and D. Courjon, *Near Field Optics* (Springer Science & Business Media, 2012).

221. M. Nieto-vesperinas and N. García, *Optics at the Nanometer Scale: Imaging and Storing with Photonic Near Fields* (Springer Science & Business Media, 2012).

222. L. Novotny and B. Hecht, *Principles of Nano-Optics* (Cambridge University Press, 2012).

223. J. A. Veerman, A. M. Otter, L. Kuipers, and N. F. van Hulst, "High definition aperture probes for near-field optical microscopy fabricated by focused ion beam milling," Appl. Phys. Lett. **72**, 3115–3117 (1998).

224. B. Hecht, B. Sick, U. P. Wild, V. Deckert, R. Zenobi, O. J. F. Martin, and D. W. Pohl, "Scanning near-field optical microscopy with aperture probes: Fundamentals and applications," J. Chem. Phys. **112**, 7761–7774 (2000).

225. M. A. Lauterbach, "Finding, defining and breaking the diffraction barrier in microscopy – a historical perspective," Opt. Nanoscopy **1**, 8 (2012).

226. L. G. Cançado, A. Hartschuh, and L. Novotny, "Tip-enhanced Raman spectroscopy of carbon nanotubes," J. Raman Spectrosc. **40**, 1420–1426 (2009).

227. R. Zhang, Y. Zhang, Z. C. Dong, S. Jiang, C. Zhang, L. G. Chen, L. Zhang, Y. Liao, J. Aizpurua, Y. Luo, J. L. Yang, and J. G. Hou, "Chemical mapping of a single molecule by plasmon-enhanced Raman scattering," Nature **498**, 82–86 (2013).

228. R. Carminati and J.-J. Greffet, "Near-Field Effects in Spatial Coherence of Thermal Sources," Phys. Rev. Lett. **82**, 1660–1663 (1999).

229. C. Henkel, K. Joulain, R. Carminati, and J.-J. Greffet, "Spatial coherence of thermal near fields," Opt. Commun. **186**, 57–67 (2000).

230. R. Beams, L. G. Cançado, S.-H. Oh, A. Jorio, and L. Novotny, "Spatial Coherence in Near-Field Raman Scattering," Phys. Rev. Lett. **113**, 186101 (2014).

231. B. Hecht, H. Bielefeldt, Y. Inouye, D. W. Pohl, and L. Novotny, "Facts and artifacts in near-field optical microscopy," J. Appl. Phys. **81**, 2492–2498 (1997).

232. R. Carminati, A. Madrazo, M. Nieto-Vesperinas, and J. J. Greffet, "Optical content and resolution of near-field optical images: Influence of the operating mode," J. Appl. Phys. **82**, 501–509 (1997).

233. O. Fenwick, G. Latini, and F. Cacialli, "Modelling topographical artifacts in scanning near-field optical microscopy," Synth. Met. **147**, 171–173 (2004).

234. N. García and M. Nieto-Vesperinas, "Near-field optics inverse-scattering reconstruction of reflective surfaces," Opt. Lett. **18**, 2090–2092 (1993).

235. N. García and M. Nieto-Vesperinas, "Direct solution to the inverse scattering problem for surfaces from near-field intensities without phase retrieval," Opt. Lett. **20**, 949–951 (1995).

236. R. Carminati, N. García, M. Nieto-Vesperinas, and J.-J. Greffet, "Direct reconstruction of surfaces from near-field intensity under spatially incoherent illumination," Opt. Lett. **21**, 501–503 (1996).

237. G. S. Agarwal, "Subwavelength resolution using evanescent waves," Pure Appl. Opt. J. Eur. Opt. Soc. Part A **7**, 1143 (1998).

238. B. Redding, G. Allen, E. R. Dufresne, and H. Cao, "Low-loss high-speed speckle reduction using a colloidal dispersion," Appl. Opt. **52**, 1168–1172 (2013).

239. F. Riechert, G. Bastian, and U. Lemmer, "Laser speckle reduction via colloidal-dispersion-filled projection screens," Appl. Opt. **48**, 3742–3749 (2009).

240. D. J. Pine, D. A. Weitz, P. M. Chaikin, and E. Herbolzheimer, "Diffusing wave spectroscopy," Phys. Rev. Lett. **60**, 1134–1137 (1988).

241. L. G. Cançado, R. R. Naraghi, and A. Dogariu, "Passive near-field imaging with pseudo-thermal sources," Opt. Lett. **42**, 1137–1140 (2017).

242. D. S. Wiersma, "The physics and applications of random lasers," Nat. Phys. **4**, 359–367 (2008).

243. B. H. Hokr, J. N. Bixler, M. T. Cone, J. D. Mason, H. T. Beier, G. D. Noojin, G. I. Petrov, L. A. Golovan, R. J. Thomas, B. A. Rockwell, and V. V. Yakovlev, "Bright emission from a random Raman laser," Nat. Commun. **5**, 4356 (2014).

244. T.-T.-K. Tran, Ø. Svensen, X. Chen, and M. N. Akram, "Speckle reduction in laser projection displays through angle and wavelength diversity," Appl. Opt. **55**, 1267–1274 (2016).

245. B. Redding, A. Cerjan, X. Huang, M. L. Lee, A. D. Stone, M. A. Choma, and H. Cao, "Low spatial coherence electrically pumped semiconductor laser for speckle-free full-field imaging," Proc. Natl. Acad. Sci. **112**, 1304–1309 (2015).